

# UC Irvine

## UC Irvine Electronic Theses and Dissertations

### Title

Effects of Aqueous Inorganic or Viscous Organic Matrices on the Chemical and Photochemical Aging Processes of Secondary Organic Aerosols in the Atmosphere

### Permalink

<https://escholarship.org/uc/item/34q890bj>

### Author

Klodt, Alexandra

### Publication Date

2022

### Copyright Information

This work is made available under the terms of a Creative Commons Attribution License, available at <https://creativecommons.org/licenses/by/4.0/>

Peer reviewed|Thesis/dissertation

UNIVERSITY OF CALIFORNIA,  
IRVINE

Effects of Aqueous Inorganic or Viscous Organic Matrices on the Chemical and  
Photochemical Aging Processes of Secondary Organic Aerosols in the Atmosphere

DISSERTATION

submitted in partial satisfaction of the requirements  
for the degree of

DOCTOR OF PHILOSOPHY

in Chemistry

by

Alexandra LeAma Klodt

Dissertation Committee:  
Professor Sergey A. Nizkorodov, Chair  
Professor Annmarie G. Carlton  
Professor James N. Smith

2022



# TABLE OF CONTENTS

	Page
<b>LIST OF FIGURES</b>	<b>v</b>
<b>LIST OF TABLES</b>	<b>xi</b>
<b>ACKNOWLEDGMENTS</b>	<b>xiii</b>
<b>VITA</b>	<b>xiv</b>
<b>ABSTRACT OF THE DISSERTATION</b>	<b>xix</b>
<b>1 Introduction</b>	<b>1</b>
1.1 Atmospheric Aerosols . . . . .	1
1.1.1 Volatile Organic Compounds and Secondary Organic Aerosol Formation	2
1.1.2 Aerosol Composition . . . . .	3
1.1.3 Aerosol Optical Properties . . . . .	3
1.2 Secondary Organic Aerosol Aging . . . . .	5
1.2.1 Aging Processes and Changes to Aerosol Composition . . . . .	5
1.2.2 Effect of Photochemical Aging on Optical Properties . . . . .	6
1.3 Types of Condensed Phases for Aerosol Aging . . . . .	6
1.3.1 Importance of Surrounding Matrix for Aerosol Aging . . . . .	6
1.3.2 Cloud Conditions . . . . .	7
1.3.3 Concentrated Inorganics . . . . .	8
1.3.4 Organic Matrices . . . . .	9
1.4 Goals of the Thesis . . . . .	10
<b>2 Effect of Ammonium Salts on the Decarboxylation of Oxaloacetic Acid in Atmospheric Particles</b>	<b>12</b>
2.1 Abstract . . . . .	12
2.2 Introduction . . . . .	13
2.3 Materials and Methods . . . . .	17
2.3.1 Sample Aging . . . . .	17
2.3.2 Rate Constant and Branching Ratio Calculations . . . . .	19
2.3.3 Computational Details . . . . .	22
2.4 Results and Discussion . . . . .	23
2.4.1 Sample Fits and Uncatalyzed Decarboxylation . . . . .	23

2.4.2	Effects of Ammonium in Weakly Acidic Solutions (pH 3-4)	26
2.4.3	Effects of Ammonium in Highly Acidic Solutions (pH near or less than 1)	29
2.4.4	Electronic Structure Calculations	30
2.4.5	Effect of Ionic Strength on the Initial Absorbance Spectra	34
2.5	Conclusions	38
<b>3</b>	<b>Aqueous Photochemistry of Secondary Organic Aerosol of <math>\alpha</math>-Pinene and <math>\alpha</math>-Humulene in the Presence of Hydrogen Peroxide or Inorganic Salts</b>	<b>41</b>
3.1	Abstract	42
3.2	Introduction	42
3.3	Methods	45
3.3.1	Secondary Organic Aerosol Generation	45
3.3.2	Secondary Organic Aerosol Aging Experiments	46
3.3.3	HUM SOA Extraction Efficiency	47
3.3.4	Light Flux Characterization	48
3.3.5	OH Steady-State Concentration Calculation	50
3.3.6	Mass Spectrometry Analysis	51
3.4	Results and Discussion	53
3.4.1	Effect of Aging on APIN SOA Mass Spectra	53
3.4.2	Effect of Aging on HUM SOA Mass Spectra	59
3.4.3	Effect of Aging on Elemental Ratios	63
3.5	Conclusions	66
<b>4</b>	<b>Effects of the sample matrix on the photobleaching and photodegradation of toluene-derived secondary organic aerosol compounds</b>	<b>67</b>
4.1	Abstract	68
4.2	Introduction	69
4.3	Methods	72
4.3.1	Secondary Organic Aerosol Generation	73
4.3.1.1	Chamber OH Steady-State Estimation	75
4.3.2	Photolysis Experiments	76
4.3.2.1	Scaling Photodegradation Rates to Atmospheric Conditions	77
4.3.2.2	Aqueous Photolysis Experiments	80
4.3.2.3	On-Filter Photolysis Experiments	82
4.3.3	Sample and Data Analyses	83
4.3.3.1	UV-Vis Analyses	83
4.3.3.2	Extraction Efficiency Determination	84
4.3.3.3	UPLC-HRMS Analysis	85
4.3.3.4	FTIR Analysis	87
4.3.3.5	Offline-AMS Analysis	87
4.4	Results and Discussion	88
4.4.1	Optical Properties	88
4.4.2	Chemical Composition Changes with Photolysis	95
4.4.2.1	PDA Data	95

4.4.2.2	SOA Composition - High Resolution Mass Spectrometry . .	100
4.4.2.3	Changes in Nitrogen-Containing Groups with On-Filter Photo- lysis . . . . .	107
4.4.2.4	Effect of Photolysis Matrix on the Photo-degradation Mech- anism . . . . .	111
4.5	Conclusions/Atmospheric Implications . . . . .	113
<b>5</b>	<b>Conclusions</b>	<b>116</b>
	<b>References</b>	<b>120</b>

# LIST OF FIGURES

	Page
1.1 Representation of organic and aqueous domains in a phase-separated aerosol	7
2.1 The decarboxylation reaction of OAA reported by Thalji et al. <sup>95</sup> adjusted to represent majority species at pH 3 to 4 by not deprotonating the carboxylic acid at carbon 4. The reaction is catalyzed by forming an imine as shown.	15
2.2 The proposed mechanism for OAA's decarboxylation including the six-membered ring transition state a) without catalyst and b) in the presence of ammonium.	16
2.3 The absorption spectrum of OAA in water over time.	24
2.4 Absorbance at 260 nm, normalized to time 0, for 1 mM OAA in pure water. The data is shown with individual dots and the fit with a solid line.	25
2.5 Absorbance at 260 nm, normalized to time 0, for 1 mM OAA in 1 M ammonium sulfate solution. The data is shown with individual dots and the fit with a solid line.	25
2.6 Absorbance at 260 nm, normalized to time 0, for 1 mM OAA in 1.54 M ammonium bisulfate solution. The data is shown with individual dots and the fit with a solid line.	26
2.7 Pseudo-first order rate constants for the decay of OAA's absorbance peak at 260 nm as a function of cation concentration (ammonium concentration for ammonium sulfate and ammonium chloride; sodium concentration for sodium sulfate). The data for ammonium sulfate is shown in red, ammonium chloride in black, and sodium sulfate in blue. Error bars represent standard deviations computed from the individual fits. As the temperature and pH were not intentionally fixed, some spread in the rate constants obtained may be expected due to variations in the room temperature or differences in the solution pH. This particularly applies when comparing the ammonium sulfate (pH = 3.7 ± 0.3) and ammonium chloride conditions (pH = 3.0 ± 0.3). See Table 2.1 for more detailed information on the pH of individual experimental trials.	27
2.8 The electronic energies of species likely involved in the ammonium-catalyzed decarboxylation of OAA. The reference energy of the product was set to 0 kcal mol <sup>-1</sup> , and the reference energy of the imine and enamine species were calculated accordingly. Values without and with parentheses are the relative free energies in the aqueous phase and the gas phase, respectively. All energies were calculated at PBE0/TZVPP level and reported in kcal mol <sup>-1</sup> .	31

2.9	(a) Select stationary points of the uncatalyzed (black) and ammonium-catalyzed (blue) decarboxylation reaction of OAA. Values without and with parentheses are the relative free energies with COSMO (representing the aqueous phase) and without COSMO (representing the gas phase), respectively. (b) Select stationary points of the uncatalyzed decarboxylation of OAA without COSMO (gas phase) shown in blue and with COSMO (aqueous phase) shown in black. (c) Select stationary points of the ammonium-catalyzed decarboxylation of OAA without COSMO (gas phase) shown in blue and with COSMO (aqueous phase) shown in black. All energies were calculated at PBE0/TZVPP level and reported in kcal mol <sup>-1</sup> . . . . .	32
2.10	Initial absorbance spectra for solutions containing ammonium sulfate. 1 mM OAA without added salts is shown in black. Traces are also shown for 1 mM OAA in 0.5 M (red), 1.0 M (orange), 1.5 M (green), 2.0 M (blue), and 2.5 (purple) M ammonium sulfate. . . . .	35
2.11	Absorbance spectra for OAA in ammonium bisulfate at their maximum value. 1 mM OAA without added salts is shown in black. Traces are also shown for 1 mM OAA in 0.5 M (red), 0.8 M (orange), 1.5 M (green), 2.0 M (purple) ammonium bisulfate, and acidified to pH 1.0 using sulfuric acid(gray). . . . .	35
2.12	Initial absorbance spectra for solutions containing ammonium chloride. 1 mM OAA without added salts is shown in black. Traces are also shown for 1 mM OAA in 0.25 M (red), 0.5 M (orange), 1.0 M (yellow), 1.5 M (green), 2.0 M (blue), and 2.5 (purple) M ammonium chloride. The traces in dashed lines have the pH adjusted to 4.0 so that the enol band is present as in the ammonium sulfate conditions. . . . .	36
2.13	Initial absorbance spectra for solutions containing sodium sulfate. 1 mM OAA without added salts is shown in black. Traces are also shown for 1 mM OAA in 0.25 M (red), 0.75 M (yellow), 1.0 M (green), and 1.3 M (blue) M sodium sulfate. . . . .	36
3.1	A test for the extraction efficiency of HUM SOA in water. . . . .	48
3.2	The spectral flux densities over the range of the electromagnetic spectrum of the photolysis set-up used in these experiments (in red), the 24-hour averaged solar spectrum in Los Angeles, California (Latitude/Longitude: 34°/118°) for the month of June (in blue), and the solar spectrum at a solar zenith angle (SZA) of zero (in green). . . . .	49
3.3	Mass spectra for the APIN SOA aged in nanopure water at 0, 1, 2, 3, and 4 h. Panel (a) shows aging with photolysis, and panel (b) shows dark aging. . . . .	54



3.4	Dimer/monomer ratios and $C_{15}/C_{10}$ ratios for APIN SOA (a) and HUM SOA (b), respectively, are shown for 0 h, the dark control at 4 h, and photolysis at 4 h. Data are grouped by aqueous aging conditions. Ratios are calculated by dividing the total dimer by the total monomer peak intensity or the total $C_{15}$ by the total $C_{10}$ peak intensity. These ratios are analogous in the sense that monomer and $C_{10}$ peaks both represent lower molecular weight aging products in the performed experiments. Further explanation of $C_{10}$ and $C_{15}$ peaks is provided in the section discussing the effect of aging on HUM SOA mass spectra. . . . .	56
3.5	Mass spectra for the APIN SOA aged with 0.01 mM $H_2O_2$ . Panel (a) shows aging with photolysis and panel (b) shows dark aging. . . . .	57
3.6	Mass spectra for the APIN SOA aged with 0.15 mM $NaNO_3$ . Panel (a) shows aging with photolysis and panel (b) shows dark aging. . . . .	58
3.7	Mass spectra for the APIN SOA aged with 0.15 mM $NH_4NO_3$ . Panel (a) shows aging with photolysis and panel (b) shows dark aging. . . . .	59
3.8	Mass spectra for the HUM SOA aged in nanopure water. Panel (a) shows aging with photolysis and panel (b) shows dark aging. . . . .	60
3.9	Mass spectra for the HUM SOA aged with 0.01 mM $H_2O_2$ . Panel (a) shows aging with photolysis and panel (b) shows dark aging. . . . .	62
3.10	Mass spectra for the HUM SOA aged with 0.15 mM $NaNO_3$ . Panel (a) shows aging with photolysis and panel (b) shows dark aging. . . . .	62
3.11	Mass spectra for the HUM SOA aged with 0.15 mM $NH_4NO_3$ . Panel (a) shows aging with photolysis and panel (b) shows dark aging. . . . .	63
3.12	Average values for the number of carbon atoms, O/C ratios, H/C ratios, and N/C ratios are shown at each hour of the four-hour aging time of APIN SOA in nanopure water, 0.01 mM $H_2O_2$ , 0.15 mM $NaNO_3$ , and 0.15 mM $NH_4NO_3$ . Open circles denote the dark control condition, and closed circles denote the photolysis condition. . . . .	64
3.13	Average values for the number of carbon atoms, O/C ratios, H/C ratios, and N/C ratios are shown at each hour of the four-hour aging time of HUM SOA in nanopure water, 0.01 mM $H_2O_2$ , 0.15 mM $NaNO_3$ , and 0.15 mM $NH_4NO_3$ . Open circles denote the dark control condition, and closed circles denote the photolysis condition. . . . .	64
4.1	PTR-ToF-MS data using the $[^{13}CC_6H_8 + H]^+$ trace to estimate the OH steady-state concentrations in the chamber during SOA formation. The unsteady signal at early times arises from incomplete mixing in the chamber during the toluene injection. Panel (a) shows the data series normalized to the count value at 3000 s where we began the linear fit in panel (b). Panel (b) shows $-\ln(\frac{[VOC]}{[VOC]_0}) \times k_{OH}^{-1}$ , with $\frac{[VOC]}{[VOC]_0}$ being the normalized PTR counts shown in panel (a) as a function of time since 3000 s as a rearrangement of Equation 4.1. The slope of this trace represents the OH steady-state concentration in the chamber. . . . .	76

4.2	Spectral photon flux density ( $F(\lambda)$ ) and its product with the mass absorption coefficient ( $F(\lambda) \times MAC(\lambda)$ ) for UCI photolysis lamp (black solid), WM photolysis lamp (black dashed), solar zenith angle zero (red), and the Los Angeles 24-h average (blue). . . . .	79
4.3	A test of the extraction efficiency of the toluene SOA (a) from the Teflon filters, (b) from the pure water solutions, and (c) from the 1 M ammonium sulfate solutions. . . . .	85
4.4	The wavelength-dependent mass absorption coefficient plots for each experimental condition and control. Photolysis in water is in panel (a), dark aging in water is in panel (b), photolysis in 1 M ammonium sulfate is in panel (c), dark aging in 1 M ammonium sulfate is in panel (d), and photolysis on the filter is in panel (e). Note that there are only four traces for the filter photolysis in panel e) because measuring the absorbance requires extraction of the filter and therefore is destructive. . . . .	89
4.5	Normalized absorbance decay of the wavelengths integrated from 300 to 700 nm with photolysis. Photolysis experiments in 1 M ammonium sulfate are shown in black circles, in pure water are shown in blue squares, and on the filter are shown in red triangles. Values on the y-axis were corrected for changes in the dark and then normalized to the mass absorption coefficient at zero minutes. Shaded areas represent one standard deviation of the fit of the three combined trials. . . . .	91
4.6	Changes in the normalized absorbance of wavelengths integrated from 300 to 700 nm in the dark for aqueous samples. Individual trials aged in water are shown with blue crosses and individual trials aged in 1 M ammonium sulfate are shown with black squares. Fits are shown in blue for water and black for 1 M ammonium sulfate. The slight increase in absorbance in the ammonium sulfate solutions is due to reactions of ammonia with SOA carbonyl compounds producing light-absorbing products. . . . .	92
4.7	Normalized absorbance decay of wavelengths integrated from 300 to 700 nm with photolysis on the filter fit to a single exponential decay without constraining absorbance at time infinity to zero, i.e. allowing a photorecalcitrant fraction. . . . .	94

4.8	UPLC-PDA chromatograms for (a) unaged toluene SOA sample (black trace), photolyzed 5 h in water (blue trace), and photolyzed 5 h on the filter (green trace) from Filter 3 and (b) unaged toluene SOA (black trace), photolyzed 5 h in water (blue trace), and photolyzed 5 h in 1 M ammonium sulfate (red trace) from Filter 4. The black (unaged) and blue (photolyzed in water) traces are shown twice to illustrate the extent of reproducibility of this analysis. PDA counts were integrated over 300 to 680 nm wavelength range to match with the UV-Vis data analysis. A blank PDA spectrum (see Figure 4.9), also integrated from 300 to 680 nm, was subtracted from each PDA spectrum shown here. The peaks for which molecular formulas could be assigned are marked on the graph and their assigned formulas are indicated, while asterisks denote unnamed formulas. In the case of 1 M ammonium sulfate, PDA counts were adjusted for the estimated 50% extraction efficiency. Additionally, the baselines are each offset by $10^3$ PDA counts on the y-axis of panel (a) and $2 \times 10^3$ PDA counts on the y-axis of panel (b) for ease of comparison. . . . .	95
4.9	HPLC-PDA chromatograms for all dark conditions studied. PDA counts were integrated over 300 to 680 nm wavelength range. The blank PDA chromatogram shown as the last trace was subtracted from the rest of the traces. For display purposes, the traces are offset by adding $10^3$ unit spacing between them. . . . .	97
4.10	Mass spectra for all photolysis and dark aged samples comparing aging in water and on the filter. CHON compounds are shown in red and CHO compounds are shown in black. . . . .	101
4.11	Mass spectra for all photolysis and dark aged samples comparing aging in water and 1 M ammonium sulfate. CHON compounds are shown in red and CHO compounds are shown in black. . . . .	103
4.12	Van Krevelen diagrams for the (a) unaged sample, (b) sample aged in water in the dark, (c) sample photolyzed in water, and (d) sample photolyzed on the filter from Filter 3. CHO formulas are shown in black and CHON formulas are shown in red. The size of the marker represents the summed mass spectrometry abundance of all CHO or CHON compounds with the corresponding H:C and O:C ratios. . . . .	105
4.13	Van Krevelen diagrams for the (a) unaged sample, (b) sample aged in 1 M ammonium sulfate in the dark, (c) sample photolyzed in water, and (d) sample photolyzed in 1 M ammonium sulfate from Filter 4. CHO formulas are shown in black and CHON formulas are shown in red. The size of the marker represents the summed mass spectrometry abundance of all CHO or CHON compounds with the corresponding H:C and O:C ratios. . . . .	106

4.14	(a) Totals for the main fragment ions for nitrogen-containing groups measured by aerosol mass spectrometry before (in black) and after 5 h of photolysis (in red) in the aqueous phase and organic particle phase. $\text{NO}^+$ and $\text{NO}_2^+$ fragment concentrations are normalized to an internal standard. (b) $\text{NO}^+/\text{NO}_2^+$ fragment ratios before (in black) and after 5 h of photolysis (in red) for samples age in water and on the filter. (c) $\text{NO}^+/\text{NO}_2^+$ fragment ratios for the isotopically labeled inorganic internal standard. Error bars represent one standard deviation over five injections. . . . .	108
4.15	ATR-FTIR spectra taken after different times of on-filter photolysis normalized to the highest peak in each spectrum – the C=O peak at $1717\text{ cm}^{-1}$ from Filter 2. The trace for before photolysis is shown in dark red, after 6 h of photolysis in yellow, after 18 h in teal, and after 24 h in light blue. The photolysis for this experiment was performed with the irradiation set up at WM. . . . .	110

# LIST OF TABLES

	Page
2.1 A summary of individual decarboxylation experiments performed: type of salt added to the experimental solution, the concentration of salt added, measured solution pH, calculated rate constant from pseudo-first-order fit (as well as the fit's standard deviation), the lifetime of OAA in this solution, and branching ratio to compare the lifetime of OAA with respect to OH-oxidation and decarboxylation. The rate constant and branching ratio calculations are discussed in the next section. Branching ratios are calculated at pH 3.7 for all conditions except solutions containing ammonium bisulfate, which are calculated at pH 1.	18
2.2 The equilibrium ratios of OAA's forms in solution and the abundances as determined by Kozlowski et al. <sup>94</sup> at pH 3.7 and pH 1.	20
2.3 Equilibrium ratios used to calculate OH rate constants, OH rate constants for individual OAA forms calculated from the SAR, and final estimated aqueous OH rate constants at pH 3.7 and pH 1.	22
2.4 Data from individual decarboxylation reactions in the presence of ammonium bisulfate.	30
3.1 Conditions used for SOA preparation. SOA concentration represents the average during the collection of two sequentially collected filters, and so the concentrations are different.	46
3.2 Summary of aqueous samples prepared from SOA filters. Aqueous SOA concentration assumes full dissolution of SOA.	47
3.3 The integrated fluxes and the number of hours equivalent to one hour under the photolysis set-up for the 24-hour average solar flux in June in Los Angeles. The calculation was performed by integrating the flux in Figure 3.2 for the three UV wavelength ranges that may potentially drive photochemistry. The values in the last column represent the ratios of the UV lamp's integrated flux to the solar integrated flux.	49
3.4 Values of interest for OH steady-state concentration calculation. Values for the concentration of SOA take into account extraction efficiency as described in Section 3.3.3.	51
3.5 Some of the major compounds detected in the APIN SOA by mass spectrometry. Photolyzable groups are shown in red, and hydrolyzable groups are shown in blue. Suggested structures were retrieved from previous work. <sup>162-167</sup>	55

3.6	The major compounds detected in the HUM SOA before aging. The only previously identified HUM SOA compound structure is included. <sup>134</sup> . . . . .	61
4.1	Summary of the experiments carried out as part of this study at the College of William and Mary (WM) and the University of California Irvine (UCI). . . . .	73
4.2	Summary of samples prepared and the experiments they were used for at William and Mary (WM) and University of California Irvine (UCI). . . . .	74
4.3	The integrated photon flux densities and the number of hours equivalent to one hour under the UCI and WM photolysis set-ups for the 24-h average solar flux in Los Angeles, California in summer and the maximal achievable flux at the SZA = 0. The calculation was performed by integrating $F(\lambda) \times MAC(\lambda)$ from Figure 4.2 from 280 to 400 nm, the UV wavelength range that likely drives photochemistry for our samples. The values on the last two columns represent the ratios of the UV lamp's integrated flux to the solar integrated flux. . . . .	79
4.4	Summary of aqueous SOA samples and their mass concentrations for aqueous-phase photolysis experiments. Mass concentrations from the same filter vary slightly between experiments aged in water versus aged in ammonium sulfate because the exact mass of the filter half was divided by the total mass of the filter and then multiplied by the mass of SOA collected in an attempt to account for differences in sizes of the filter sections. The mass concentrations are still somewhat approximate because the SOA may not have been completely evenly distributed on the filter after collection. . . . .	81
4.5	Kinetic parameters for exponential and biexponential fits to absorbance data. Error represents the standard deviation of fitting parameters over the three combined trials. . . . .	94
4.6	Absorbance lifetimes for photobleaching processes described by Equation 4.5 scaled to the 24-h average solar actinic flux in Los Angeles. Errors represent the standard deviations over the three combined trials. . . . .	94
4.7	Formulas associated with the well-defined peaks in the integrated (300 to 680 nm) unaged PDA data and the percent change from unaged after aging for individual peaks, the total resolved peak area, and the area of the unresolved baseline. The area of the unresolved baseline feature was calculated by integrating the sample PDA from 300 to 680 nm and summing from 5 to 12 min and then subtracting the area of the blank integrated from 300 to 680 nm summed from 5 to 12 min and the area of the resolved peaks. . . . .	98
4.8	Formulas associated with the well-defined peaks in the integrated (300 to 680 nm) unaged PDA data and the percent change from unaged after aging for individual peaks, the total resolved peak area, and the area of the unresolved baseline. The area of the unresolved baseline feature was calculated by integrating the sample PDA from 300 to 680 nm and summing from 5 to 12 min and then subtracting the area of the blank integrated from 300 to 680 nm summed from 5 to 12 min and the area of the resolved peaks. . . . .	99

# ACKNOWLEDGMENTS

I would like to thank the many people who made it possible for me to finish my degree. First, my advisor Sergey Nizkorodov has given me guidance and support throughout the past five years. I would like to thank him for dedicating so much of his time and energy (and coffee) to my success during my time here.

Thanks to my collaborators, including Julia Laskin, Alexander Laskin, Peng Lin, Dian Romonosky, Phillip Furche, and Rachel O'Brien. Their input on each of my projects was invaluable to the final result, and I am grateful. Also, thank you to Veronique Perraud and Lisa Wingen for always helping out with many miscellaneous things around the lab.

On a similar note, my project on oxaloacetic acid would never have gotten off the ground without the help of several undergraduate students: Jiajing (Judith) Wang, Michael Olsen, Jorge Fernandez, and especially Kimberly Zhang. Thank you for your hard work on the project. It was a pleasure to mentor each of you. Also, thanks to Marley Adamek and Monica Dibley for their work on the toluene aging project.

Thank you to the other members of the Aerosol Photochemistry Group; you guys are the reason we have the best group! I want to thank Lauren Fleming for helping me get established in graduate school, giving me advice, and for all of the time we spent working out and hanging out after work. I also want to thank Cynthia Wong for giving me endless encouragement, teaching me to climb, and just generally being a great friend. Finally, I need to thank Natalie Smith and Vahe Baboosian. I cannot imagine graduate school without you guys. I am very grateful to have been a triplet with you!

I have made some amazing friends while in graduate school, and I am grateful to all of them. The community we built together got us through graduate school and a worldwide pandemic. Thank you all for keeping me sane. I particularly want to thank Natalie Smith (again – she's my twin so I have to mention her twice) and Taylor Frey for hanging out with me pretty much every weekend and sharing all of the ups and downs of life.

Speaking of ups and downs, I want to give a huge thank you to Igor Palubski. You were probably the most constant thing in my life during graduate school: constantly supportive, encouraging, and understanding. I'm glad we could go through this together.

I would also like to thank my parents. You instilled a lot of important life skills in me that have really helped me to be successful. Thank you for supporting my decision to go to graduate school, even if it meant moving all the way to California.

Finally, I acknowledge my research funding sources. Chapters 2, 3, and 4 were funded by NSF grant AGS-1853639. Chapter 2 was additionally funded by NSF grant CHE-1800431, and Chapter 4 was additionally funded by NSF grant AGS-2042619, NSF grant AGS-1936123, and William & Mary Honors research funding.

# VITA

## Alexandra LeAma Klodt

### EDUCATION

**University of California, Irvine**  
PhD in Atmospheric Chemistry  
Cumulative GPA: 3.974  
Thesis Advisor: Professor Sergey Nizkorodov

*Irvine, CA*  
*August 2017 - August 2022*

**University of California, Irvine**  
Masters in Atmospheric Chemistry  
Cumulative GPA: 3.965  
Thesis Advisor: Professor Sergey Nizkorodov

*Irvine, CA*  
*August 2017 - June 2020*

**Iowa State University-Magna Cum Laude**  
Bachelor of Science, Chemistry  
Minor in Psychology  
Cumulative GPA: 3.897  
Research Advisor: Professor William Jenks

*Ames, IA*  
*August 2013 - May 2017*

### Awards/Fellowships/Memberships:

Award for contributions to the chemistry department teaching program by a TA (2022), Micheal E. Gebel Award (2021), American Association for Aerosol Research Member (2018-Present), American Chemical Society Member (2017-Present), Phi Beta Kappa Honor Society (2016, senior inductee), President's Academic Certificate of Excellence Award (2013-2017), Fahrney Foundation Award (2013-2016), Plagens Research Scholarship (2015), Reding/Monsanto Engineering Award (2014), Cardinal Scholar Award (2013)

### PUBLICATIONS

1. Klodt, A.; Romonosky, D.; Lin, P.; Laskin, J.; Laskin, A.; Nizkorodov, S. Aqueous Photochemistry of Secondary Organic Aerosol of  $\alpha$ -Pinene and  $\alpha$ -Humulene in the Presence of Hydrogen Peroxide or Inorganic Salts. *ACS Earth and Space Chem.*, **3** (2019) 2736-2746. DOI: 10.1021/acsearthspacechem.9b00222
2. Klodt, A.; Zhang, K.; Fernandez, J.; Olsen, M.; Furche, F.; Nizkorodov, S. Effect of Ammonium Salts on the Atmospheric Aging of 3-Oxocarboxylic Acids. *ACS Earth and Space Chem.*, **5** (2021) 931-940. DOI: 10.1021/acsearthspacechem.1c00025
3. Klodt, A.; Adamek, M.; Dibley, M.; Nizkodorov, S.; O'Brien, R. Effects of the Sample Matrix on the Photobleaching and Photodegradation of Toluene-Derived Secondary



Organic Aerosol Compounds. *Atmospheric Chemistry and Physics*, **22** (2022) 10155-10171 DOI: 10.5194/acp-22-10155-2022

4. Klodt, A.; Aiona, P.; MacMillan, A.; Lee, J.; Zhang, X.; Helgestad, T.; Novak, G.; Lin, P.; Wingen, L.; Laskin, J.; Laskin, A.; Bertram, T.; Cappa, C.; Nizkorodov, S. Effects of Humidity, NO<sub>x</sub>, and Ammonia on the Optical Properties and Molecular Composition of Photo-oxidized Naphthalene Secondary Organic Aerosols. (*in preparation*)
5. Edwards, K.; Klodt, A.; Galaezzo, T.; Schervish, M.; Wei, J.; Fang, T.; Aumont, B.; Nizkorodov, S.; Shiraiwa, M. Nitrogen Oxide Influences on the Production of Reactive Oxygen Species from  $\alpha$ -Pinene and Naphthalene Secondary Organic Aerosols. (*Journal of Physical Chemistry A, submitted*)
6. Zhang, K.; Klodt, A.; Furche, F.; Nizkorodov, S. Exploring the Gas-Phase Photochemistry of Oxaloacetic Acid and Diethyl Oxaloacetate Using Experimental Methods and Non-adiabatic Molecular Dynamics. (*in preparation*)
7. Wilkinson, C.; Klodt, A.; Nizkorodov, S.; O'Brien, R. Effects of Environmental Conditions and Light Flux on the Photo-Aging of Naphthalene Secondary Organic Aerosol. (*in preparation*)

**Conference Presentations** \* indicates the presenting author

#### Invited Talks:

R. O'Brien\*, A. Klodt, L. Nicks, H. Yu, N. Warren, C. Wilkinson, M. Adamek, C. Cappa, J. Kroll, C. Jordan, B. Anderson, S. Nizkorodov, C. Lim: The role of water vapor on photo-bleaching of organic particles, AAAR, October 3-7, 2022, Raleigh, NC.

#### Platform Presentations:

S. Frey\*, A. Klodt, A. Burns, A. Carlton, S. Nizkorodov: Uptake of atmospheric trace gases into water-containing aerosol particles, Student Research Program Symposium; Grad Division, August 11, 2022, Irvine, CA.

R. O'Brien\*, A. Klodt, L. Nicks, H. Yu, N. Warren, C. Wilkinson, M. Adamek, C. Cappa, J. Kroll, C. Jordan, B. Anderson, S. Nizkorodov, C. Lim: The role of water vapor on photo-bleaching of organic particles, IGAC, September 10-15, 2022, Manchester, UK.

A. Klodt\*, M. Adamek, M. Dibley, S. Nizkorodov, R. O'Brien: Comparing the photodegradation of toluene-derived brown carbon SOA in aerosol mimics and cloud water mimics, Pacifichem, December 22, 2021, held virtually.

A. Klodt\*, M. Adamek, M. Dibley, S. Nizkorodov, R. O'Brien: Effects of ammonium sulfate on the photodegradation of toluene-derived brown carbon SOA, AAAR, October 19, 2021, held virtually. Received a registration waiver for my abstract.

A. Klodt\*, K. Zhang, J. Fernandez, M. Olsen, F. Furche, S. Nizkorodov: The effects of ammonium on the aging of oxaloacetic acid in the atmospheric aqueous phase, ISKPPA, February 19, 2021, held virtually.

A. Klodt\*, D. Romonosky, P. Lin, J. Laskin, A. Laskin, S. Nizkorodov: Aqueous photochemistry of secondary organic aerosol in the presence of common inorganic salts, ACS Fall 2019 National Meeting and Expo, August 28th, 2019, San Diego, CA.

A. Klodt\*, D. Romonosky, P. Lin, J. Laskin, A. Laskin, S. Nizkorodov: Aqueous photochemical reactions in clouds, AirUCI Retreat, September 24-26, 2018, Lake Arrowhead, CA.

### **Poster Presentations:**

S. Frey\*, A. Klodt, A. Burns, A. Carlton, S. Nizkorodov: Uptake of atmospheric trace gases into water-containing aerosol particles, SoCal Undergraduate Chemistry Research Symposium, August 12, 2022, Irvine, CA. Won outstanding poster award.

A. Klodt\*, M. Adamek, M. Dibley, S. Nizkorodov, R. O'Brien: Effects of the sample matrix on the photobleaching and photodegradation of toluene-derived secondary organic aerosol compounds, IGASP, June 15, 2022, Irvine, CA.

K. Edwards\*, A. Klodt, T. Galeazzo, M. Schervish, J. Wei, T. Fang, B. Aumont, S. Nizkorodov, M. Shiraiwa: Nitrogen oxide influence on the production of reactive oxygen species and environmentally persistent free radicals from  $\alpha$ -pinene and naphthalene volatile organic compound precursors, IGASP, June 15, 2022, Irvine, CA.

K. Zhang\*, A. Klodt, F. Furche, S. Nizkorodov: Combined experimental and theoretical study on the uncatalyzed and ammonium-catalyzed decarboxylation of oxaloacetic acid in atmospheric particles, ACS, Spring Meeting 2021, held virtually.

A. Klodt\*, K. Zhang, J. Fernandez, M. Olsen, F. Furche, S. Nizkorodov: The effects of ammonium on atmospheric aging of 3-oxocarboxylic acids, AAAR, October 5, 2020, held virtually. Received a registration waiver for my abstract

A. Klodt\*, D. Romonosky, P. Lin, J. Laskin, A. Laskin, S. Nizkorodov: Effects of common inorganic salts on aqueous photochemistry of secondary organic aerosol, AAAR, October 17, 2019, Portland, OR.

### **RESEARCH PROJECTS**

**Optical Properties of Naphthalene High-NO<sub>x</sub> SOA**  
*Graduate Project*

2021-2022

Studied the effect of a range of humidities,  $\text{NO}_x$ , and ammonia on the optical properties of secondary organic aerosol made from the photo-oxidation of naphthalene

**Photochemical Aging of Toluene High- $\text{NO}_x$  SOA in the Atmospheric Condensed Phase** 2019-2022

*Graduate Project*

Studied the direct photolysis of toluene high- $\text{NO}_x$  secondary organic aerosol in concentrated  $(\text{NH}_4)_2\text{SO}_4$ , viscous organic phase, and dilute water to simulate aging in particle-phase water, viscous organic aerosol, or dilute cloud water, respectively.

**Effect of Salts on the Decarboxylation Lifetime of Oxaloacetic Acid** 2019-2020

*Graduate Project*

Studied the effect of  $(\text{NH}_4)_2\text{SO}_4$  on the decarboxylation lifetime of oxaloacetic acid as a representative 3-oxocarboxylic acid under representative atmospheric aqueous conditions.

**Aqueous Photochemical and Dark Reactions in Cloud-Like Conditions** 2018-2019

*Graduate Project*

Studied the effects of some atmospheric salts common in clouds on the aqueous photochemistry of  $\alpha$ -Pinene and  $\alpha$ -Humulene.

**Singlet Versus Triplet State Reactivity of Nitrenes** 2017

*Undergraduate Project*

Studied singlet versus triplet reactivity of nitrenes with an alkene after being produced from a photolytic cleavage of the sulfur-nitrogen bond of dibenzothiophene sulfimine

**DNP NMR Sensitizer Synthesis** 2016

*Undergraduate Project*

Worked on a collaborative project to synthesize a sensitizer to improve Dynamic Nuclear Polarization Nuclear Magnetic Resonance spectroscopy.

## **SKILLS**

### **Instrumentation**

Aerosol Mass Spectrometry, Proton Transfer High-Resolution Spectrometry, Electrospray Ionization High-Resolution Mass Spectrometry, Nuclear Magnetic Resonance Spectroscopy

### **Software**

Excel, Igor Pro, Xcalibur/Freestyle, PTRViewer, MZMine,  $\text{\LaTeX}$ , LabVIEW

## WORK EXPERIENCE

### University of California, Irvine

August 2017 - March 2021

*Teaching Assistant*

Taught general chemistry laboratory and lecture, two different organic chemistry laboratories, and analytical chemistry laboratory/lecture. Gained experience organizing students and explaining concepts in more accessible ways.

### Iowa State University

June 2015 - May 2017

*Undergraduate Researcher*

Conducted independent research projects. Learned and gained significant experience with organic synthesis, gas chromatography, and Nuclear Magnetic Resonance spectroscopy, as well as basic laboratory techniques and safety procedures.

## PROFESSIONAL EXPERIENCE AND TRAINING

### Index of Chamber Atmospheric Research in the United States

2019-2021

- ICARUS is a database designed to make all atmospheric chamber data public in response to the Environmental Protection Agency's "Strengthening Transparency in Regulatory Science" proposal.
- Served as a member of the developing committee, providing ideas and feedback for the functionality of the website.
- Was in charge of organizing the implementation of the website in my research group's standard protocol.

### Activate to Captivate

Winter 2019

- An 8-week certificate course designed to increase the effectiveness of presentations.
- Focused on clearly communicating scientific ideas to audiences with varying levels of subject expertise.

### Pacific Northwest National Lab Inaugural Summer School

July 2019

- Selected from 125 applicants to be one of 25 participants
- Learned about a broad range of topics including aerosol characterization, measurements, cloud condensation nuclei properties, and modeling

# ABSTRACT OF THE DISSERTATION

Effects of Aqueous Inorganic or Viscous Organic Matrices on the Chemical and Photochemical Aging Processes of Secondary Organic Aerosols in the Atmosphere

By

Alexandra LeAma Klodt

Doctor of Philosophy in Chemistry

University of California, Irvine, 2022

Professor Sergey A. Nizkorodov, Chair

After secondary organic aerosol (SOA) forms, its composition changes through various aging processes. In the laboratory setting, aging is sometimes studied in dilute aqueous systems as models for chemistry occurring in cloud and fog droplets. While pure water is often a good model for cloud and fog droplets, these droplets always contain small concentrations of inorganic salts such as ammonium sulfate or ammonium nitrate. Additionally, the aging of SOA may also occur in aerosol particles, which can include areas of concentrated aqueous solutions of these salts or semi-solid organic and inorganic phases containing less water. These differences in aging matrices can have important effects on the reaction mechanisms and kinetics of SOA aging, and it is important to understand the effects relative to dilute aqueous solutions for a comprehensive understanding of SOA evolution in the atmosphere.

Atmospheric cloud water contains low concentrations of inorganic salts (0.01 to 10 mM). The first study discussed in this thesis looks at the effect of ammonium and nitrate ions on the photochemical and dark aging of  $\alpha$ -pinene or  $\alpha$ -humulene ozonolysis SOA in cloud water mimics. SOA particles were produced from dark ozonolysis of  $\alpha$ -pinene or  $\alpha$ -humulene and collected on filters, then extracted and aged for 4 h in the dark or with photolysis in pure water or aqueous solutions containing 0.15 mM  $\text{NaNO}_3$  or  $\text{NH}_4\text{NO}_3$ . Changes in the chemical

composition of the SOA during aging were monitored by direct infusion high-resolution electrospray ionization mass spectrometry. The presence of nitrate ions decreased the average carbon atom number of compounds, even in the dark, in  $\alpha$ -pinene SOA but not  $\alpha$ -humulene SOA. This work demonstrated that inorganic salts in cloud water-type matrices may affect aging for certain SOA types.

Water in deliquesced aerosols has much higher concentrations of inorganic salts than cloud water, with ionic strengths from 1 M up to greater than 10 M. The second study in this thesis examines the effects that ammonium-containing salts at these high ionic strengths have on the decarboxylation of 3-oxocarboxylic acids. Solutions of oxaloacetic acid (OAA) – a representative 3-oxocarboxylic acid – and ammonium salts were prepared, and decarboxylation was monitored using UV-visible spectroscopy. Increasing concentrations of ammonium linearly decreased the decarboxylation lifetime of OAA. Comparing decarboxylation lifetimes and OH lifetimes suggests decarboxylation will be the dominant loss pathway for OAA and likely other 3-oxocarboxylic acids in the atmospheric aqueous phase. Additionally, the inorganic ions in the aging matrix of deliquescent aerosols can have strong effects on the aging of organics under these conditions.

Both the high ionic strength conditions of deliquesced aerosols and the low water content of dry organic particles are considered in the third project discussed in this thesis. Toluene SOA was prepared in a smog chamber by photooxidation in the presence of  $\text{NO}_x$  to investigate the effects of various matrices on the photodegradation of SOA that absorbs UV and visible radiation. The SOA was collected and photolyzed under different conditions: directly on the filter, dissolved in pure water, and dissolved in 1 M ammonium sulfate. UV-Visible spectroscopy and electrospray ionization high-resolution mass spectrometry coupled to liquid chromatography separation were used to observe changes in mass absorption coefficient (MAC) and composition during irradiation. The MAC changes over the irradiation time

were used to determine photobleaching rates, which were fastest in water, slightly slower in 1 M ammonium sulfate, and much slower directly on the filter. Conversely, the mass spectrometry analysis revealed an efficient photodegradation of nitrophenol compounds, which are expected to be major chromophores in this type of SOA, on the filter but not in the aqueous phases. This study demonstrated that the SOA absorption coefficient lifetime with respect to photobleaching and lifetimes of individual chromophores in SOA with respect to photodegradation will depend strongly and possibly independent of each other on the matrix during aging.

In the atmosphere SOA particles exist under a range of different aqueous or dry conditions, providing a range of matrices for aging. This thesis demonstrates that both dark and photolytic aging can be affected by the differences in these aging matrices compared to dilute aqueous solutions, with changes in both the aging mechanisms and rates. Understanding these effects is crucial in determining the fate of individual compounds and complex SOA particles in the atmosphere.

# Chapter 1

## Introduction

### 1.1 Atmospheric Aerosols

Aerosols are solid or liquid particles suspended in a gas,<sup>1</sup> and they have been shown to affect climate, air quality, and health.<sup>2</sup> In the atmosphere, aerosols are typically classified as organic or inorganic, meaning composed primarily of organic compounds or inorganic compounds, respectively. Field observations, however, show that aerosols in the atmosphere most often contain varying contributions of both organic and inorganic components, either in separate phases or mixed together in one phase.<sup>3</sup> The organic constituents of aerosols are relatively complex as compared to the inorganic constituents, and so the study of organic aerosols is an important and evolving frontier in the field of atmospheric chemistry.<sup>1</sup> Atmospheric aerosols may additionally be classified as primary or secondary in nature, meaning they are either directly emitted or they form from the condensation of oxidized gases into particles, respectively.<sup>1-4</sup> Contributions by secondary aerosols, at a few hundreds of Tg y<sup>-1</sup>, tend to outweigh contributions by primary aerosols, estimated to be around 30 Tg y<sup>-1</sup>.<sup>1,4,5</sup> Also, the distinction between primary and secondary aerosols quickly becomes blurred as aerosols



spend time in the atmosphere, as different aerosols mix and aging processes change the composition of both primary and secondary aerosols.<sup>6</sup>

### **1.1.1 Volatile Organic Compounds and Secondary Organic Aerosol Formation**

Secondary organic aerosol (SOA) is formed from the reactions of oxidants and volatile organic compounds (VOCs) in the atmosphere.<sup>7</sup> Common oxidants include the OH radical, ozone, and the chlorine radical during the day and the nitrate radical during nighttime.<sup>1,8</sup> VOCs may be emitted from biogenic or anthropogenic sources, and different regions of the globe experience varying contributions from either classification of VOC. Some important biogenic VOC precursors include monoterpenes ( $C_{10}H_{16}$ ), and sesquiterpenes ( $C_{15}H_{24}$ ), and these are important in both the urban and remote/rural environments.<sup>9</sup> The lifetimes of monoterpenes and sesquiterpenes with respect to atmospheric oxidants are on the order of minutes to hours,<sup>10</sup> so they have the potential to form SOA efficiently. Atmospheric concentrations of monoterpenes are hundreds to thousands of ppt,<sup>11</sup> which has encouraged many studies on SOA formation from these precursors.<sup>10,12-14</sup> Sesquiterpenes are less abundant in the atmosphere, with concentrations of tens of ppt,<sup>11</sup> but their higher molecular weights give them greater SOA formation potential, and they also have been studied as SOA precursors.<sup>1</sup> Globally, biogenic VOCs are emitted at about an order of magnitude higher rates than anthropogenic VOCs,<sup>15,16</sup> but anthropogenic VOCs also become important in areas with high levels of human activity. Aromatic compounds have garnered particular interest as anthropogenic VOCs, as they are important emissions that contribute significantly to SOA formation in urban environments.<sup>7,17</sup> Urban environments also experience high levels of nitrogen oxides ( $NO_x$ ), which will participate in the SOA formation reactions to influence the composition of the SOA.<sup>18</sup>

### 1.1.2 Aerosol Composition

The oxidation pathways during SOA formation result in oxygen-containing functional groups, such as a carbonyl, carboxyl, or hydroxyl groups, and often more than one of these groups is required for sufficiently low vapor pressures to partition into existing particles or nucleate new particles.<sup>10</sup> As a result, multifunctional compounds such as oxocarboxylic acids and dicarboxylic acids are common types of compounds in aerosol particles.<sup>19</sup> However, while SOA constituent molecules generally have a limited number of functional group types, the chemical composition of SOA is extremely complex in terms of the number of different molecules it contains. Even laboratory SOA generated from a single VOC precursor may contain thousands of individual compounds in each particle, and many studies have been conducted to elucidate formation mechanisms and SOA composition from individual precursors and mixtures of precursors alike.<sup>1</sup> SOA composition, in turn, has a large influence on the properties of the SOA. SOA formed from different precursors and under different conditions will have different composition, leading to differences in properties such as viscosity,<sup>20,21</sup> hygroscopicity,<sup>22</sup> relative humidity at which particles become phase-separated,<sup>21-23</sup> ability to act as cloud condensation nuclei,<sup>22-24</sup> and the wavelengths at which light is absorbed and scattered.<sup>25</sup>

### 1.1.3 Aerosol Optical Properties

Aerosol optical properties, which describe how aerosol particles absorb and scatter solar radiation, have been an important research topic on the basis of their climate relevance.<sup>2,25</sup> Aerosol optical properties are quantified using scattering and absorption coefficients. The scattering coefficient is the product of the number concentration and the scattering cross-section, while the absorption coefficient is the product of the number concentration and the absorption cross-section. The addition of the scattering and absorbing coefficients describes the total attenuation of incoming radiation by the aerosol and is termed the extinction coef-

ficient. The most common method for quantifying aerosol scattering is the Single Scattering Albedo, which is defined as the ratio of scattering to total extinction by the aerosol.<sup>26</sup> There are various methods for measuring and expressing absorption by aerosol particles. Most relevant to this thesis will be mass absorption coefficient, defined in equation (1.1).

$$MAC(\lambda)_{bulk} = \frac{A_{10}(\lambda) \times \ln(10)}{b \times c_{mass}} \quad (1.1)$$

$MAC(\lambda)_{bulk}$  is the wavelength-dependent mass-normalized absorption coefficient of the bulk SOA extract,  $A_{10}(\lambda)$  is the base-10 absorbance measured by the UV-Vis spectrometer,  $b$  is the pathlength, and  $c_{mass}$  is the mass concentration of the solution. Determining  $MAC(\lambda)_{bulk}$  requires the aerosol particles to be extracted into a solvent, and so it is convenient to measure using UV-Visible spectroscopy. However, it only reflects the absorption properties of the material from which the aerosols are made. In order to take into account absorption properties depending on the chemical composition of the aerosol, particle size, and particle shape, equation (1.2) is used.

$$MAC(\lambda)_{aerosol} = K\lambda^{-AAE} \quad (1.2)$$

$MAC(\lambda)_{aerosol}$  is the wavelength-dependent mass-normalized absorption coefficient,  $K$  is a preexponential factor which includes the aerosol mass concentration, and  $AAE$  is the Absorption Angstrom Exponent which describes how the absorption coefficient is related to wavelength.<sup>27</sup> The relationship between  $MAC(\lambda)_{aerosol}$  and  $MAC(\lambda)_{bulk}$  depends on the distribution of particle sizes and shapes in the suspended aerosol. This relationship is dependent on individual aerosol particles and so is complex and beyond the scope of this dissertation. Although measurements of aerosol optical properties are available, SOA represents the greatest uncertainty in net climate effects,<sup>28</sup> and this in large part is due to uncertainties in aerosol chemistry.

## 1.2 Secondary Organic Aerosol Aging

### 1.2.1 Aging Processes and Changes to Aerosol Composition

After formation, the lifetime of SOA with respect to deposition, which is the most important loss mechanism of SOA from the atmosphere, is 1 to 2 weeks.<sup>29</sup> During this time, SOA undergoes a variety of physical and chemical aging processes. Some physical processes include coagulation,<sup>30</sup> water uptake or loss,<sup>31</sup> phase transitions,<sup>32</sup> and gas-to-particle partitioning.<sup>33</sup> Of greater interest to this thesis, chemical processes also change the composition of the SOA particle. Chemical processes can be divided into photochemical and dark processes. Photochemical processes include heterogeneous reactions of photochemically-produced gas-phase free radicals with particle surfaces as well condensed-phase reactions initiated by solar photons directly inside the particles. Some dark processes specific to the condensed phase include hydrolysis,<sup>34,35</sup> oxidation reactions with oxidizing solutes, such as iron complexes,<sup>36</sup> and the formation of salts between carboxylic acids and inorganic cations.<sup>37,38</sup> As they are of particular interest to this thesis, interactions with inorganic ions will be discussed in more depth in Section 3.

Condensed-phase photochemical processes can be further categorized as indirect or direct. Indirect photolysis reactions occur when excitation energy from an organic chromophore is transferred to another molecule to produce reactive species, such as OH radicals, singlet oxygen, or triplet states, which then react with SOA compounds. These processes often result in more functionalized products with lower volatility for at least the first few minutes of aging, although eventually, fragmentation reactions begin to outweigh functionalization.<sup>39,40</sup> Direct photolysis involves the direct absorption of UV radiation by a compound that breaks down following the excitation. Common compounds that efficiently undergo direct photolysis in

particles include carbonyls, peroxides, and organic nitrates, with varying relative importance depending on the SOA type and formation conditions.<sup>40–46</sup>

## **1.2.2 Effect of Photochemical Aging on Optical Properties**

In addition to changing the SOA composition, photochemical aging leads to changes in optical properties. Since indirect photolysis leads to more functionalized compounds in the SOA particles,<sup>39,40</sup> this often translates to a greater abundance of chromophores and can therefore lead to more absorbing SOA particles. Direct photolysis, on the other hand, often leads to chromophore destruction and subsequent photobleaching of absorbing SOA particles.<sup>3</sup> These two processes sometimes occur in parallel, as well. For instance, when a hydroperoxide (ROOH) is photolyzed, the original chromophore is chemically altered, but an OH radical is also produced to participate in further indirect photolysis pathways.<sup>45</sup> The optical properties of SOA can therefore have a complex response to UV irradiation depending on the starting SOA composition.

## **1.3 Types of Condensed Phases for Aerosol Aging**

### **1.3.1 Importance of Surrounding Matrix for Aerosol Aging**

Aerosol particles are estimated to spend 15% of their lifecycle under cloud conditions, and the other 85% as a deliquesced aerosol or a phase-separated aerosol with both concentrated organics and concentrated inorganics present in individual pockets.<sup>47</sup> All three of these environments have unique implications for the aging of SOA. Two significant differences between the three environments are the concentration of organic molecules and the concentration of inorganic ions, providing unique matrices for the aging of the SOA compounds. Cloud and

fog water is relatively dilute, with organic concentrations on the order of 10 to 100 mgC L<sup>-1</sup> and ionic strengths of 10<sup>-5</sup> to 10<sup>-2</sup> M.<sup>48,49</sup> Aerosol particles are distinguished from cloud droplets by their smaller size and higher solute levels. Aerosol particles, as shown in Figure 1.1, can have particle domains that are nearly 100% organic in composition, as well as aqueous phase domains that have ionic strengths greater than 1 M, sometimes measured to be greater than 10 M.<sup>49</sup> The domains with concentrated organics are much more viscous than the aqueous phases, with viscosities ranging from 10<sup>2</sup> to 10<sup>8</sup> compared to 10<sup>-2</sup> Pa.s.<sup>20</sup> The dominant inorganic species in the aqueous domains contributing to ionic strength in the atmosphere are ammonium, sulfate, and nitrate, particularly in urban areas with high emissions of anthropogenic ammonia, sulfur dioxide, and NO<sub>x</sub>.<sup>50</sup> Other ions which contribute to ionic strength in the atmosphere include sodium and chloride, and these become more important in areas impacted by sea spray.<sup>49</sup> Aging processes can be impacted by the conditions in these different matrices, depending on the viscosity, proximity of other organic molecules, ionic strength, and identity of nearby ions as described below.

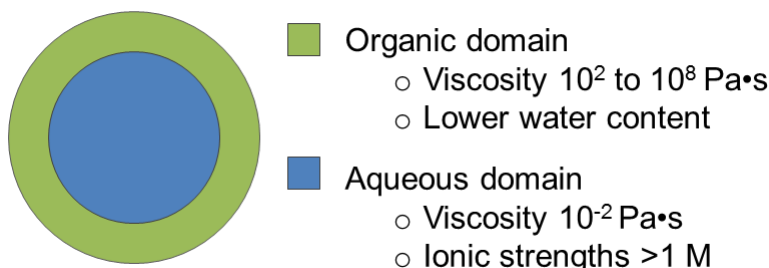


Figure 1.1: Representation of organic and aqueous domains in a phase-separated aerosol

### 1.3.2 Cloud Conditions

Cloud- and fog-droplet chemistry is important both to SOA formation and aging.<sup>49</sup> Five to 60% of global SOA is estimated to result from in-cloud processing,<sup>51</sup> and aqueous-phase reactions have been suggested to explain the differences in oxidation level measured in field studies compared to laboratory studies.<sup>52,53</sup> Importantly, in-cloud processing of isoprene ox-

idation products is thought to be a major contributor to SOA production.<sup>54,55</sup>

Important SOA aging processes also occur in cloud and fog water. Studies on the direct photolysis of aqueous-phase SOA extracts in pure water or mixtures of water and methanol have provided insight into cloud and fog water chemistry.<sup>56-60</sup> Composition changes were observed with photolysis for the SOA, with irradiation generally reducing the average molecule size and degrading chromophores.<sup>56-60</sup>

While the concentrations of inorganic ions in cloud water are low, they still have effects on SOA chemistry in this phase. An important example is the production of OH radicals with the photolysis of  $\text{NO}_3^-$  ions in cloud water.<sup>61</sup> It was demonstrated that SOA formed more efficiently from syringaldehyde and acetosyringone in solutions with micromolar concentrations of ammonium nitrate than in solutions with micromolar concentrations of ammonium sulfate with photolysis, likely because of the formation of OH radicals with nitrate photolysis.<sup>62</sup> Other types of aqueous reactions are possible at low concentrations of inorganic ions, as well. For instance, ammonium ions are known to be catalysts for various reactions.<sup>63,64</sup> Also, many inorganic ions are weak acids or bases and may therefore change the pH or other equilibria of solutions or act as buffers.

### 1.3.3 Concentrated Inorganics

With the much higher ionic strength of deliquesced aerosols, photochemical processes occurring in this phase have more potential to be altered by inorganic species. There have been a few studies looking into the effect of high ionic strength on the photochemistry of SOA compounds, although they have largely focused on the photolysis of single molecules in the presence of sodium salts.<sup>65-69</sup> Generally, all of the work done has shown a red shift in the absorption spectrum with ionic strength.<sup>65-67,69</sup> However, the changes in the photodegrada-

tion rates have varied between experiments, with some finding accelerated photodegradation at high ionic strength,<sup>65,66</sup> and others finding decelerated photodegradation at high ionic strength.<sup>67,69</sup> Photo-bleaching has also been shown to be decelerated for rice-straw smoldering primary organic aerosol when ionic strength was adjusted with NaCl, NaNO<sub>3</sub>, and Na<sub>2</sub>SO<sub>4</sub>.<sup>68</sup> High concentrations of inorganic ions clearly have an effect on the photochemistry of SOA in the aqueous phase, but there is no consensus on what the effects are. Also, the most common salts in the atmosphere – ammonium sulfate and ammonium nitrate – are not represented in the studies that were conducted prior to the work in this thesis.

### 1.3.4 Organic Matrices

Some areas of aerosol particles can differ dramatically from the two conditions already discussed (cloud conditions and concentrated inorganics), consisting almost entirely of solid or semisolid organic material and limited water. Direct photolysis has for some years been considered a potentially important sink for SOA compounds, particularly those found in SOA from aromatic precursors, in this environment based on the absorption coefficients of several SOA types.<sup>70</sup> The measurement of volatile product formation with direct photolysis demonstrated that SOA in this phase is in fact labile to direct photolysis.<sup>71–73</sup> Further studies found that peroxide and carbonyl groups were responsible for driving photochemistry for low-NO<sub>x</sub> terpene ozonolysis SOA.<sup>41–46,74</sup> Meanwhile, it was observed that photodegradation was actually slower with direct photolysis of aromatic-derived SOA in spite of its greater absorption coefficients.<sup>75–77</sup> Additionally, some individual chromophores were observed to photolyze at different rates between organic and aqueous matrices as well as between different organic matrices.<sup>78–81</sup> When considering the effects of the range of matrices described above, it becomes clear that these matrices have important effects on aerosol aging in the atmosphere. Therefore it is important to better understand the influence of the aerosol aging matrix on the aging processes occurring in the atmosphere.



## 1.4 Goals of the Thesis

The overarching goal of this thesis is to explore the influence of the surrounding matrix on dark and photochemical aging processes occurring in atmospheric organic aerosols, with a focus on the indirect effects of inorganic salts on the photochemistry of organic compounds. Conditions representing cloud water, deliquesced aerosols with high ionic strength, and organic aerosols with low liquid water content are examined, and changes in aerosol composition and optical properties are explored as part of this work. The relevant background for each project will be described in depth at the beginning of each corresponding chapter. A brief overview of the goals of each chapter is provided below.

Chapter 2 describes the effect of varying concentrations of ammonium salts on the rate of decarboxylation of a representative 3-oxocarboxylic acid. The decarboxylation rate of oxaloacetic acid was measured in aqueous solutions of ammonium sulfate, ammonium bisulfate, ammonium chloride, and sodium sulfate, with cation concentrations ranging from 0 to 5 M and pH values ranging from 4.0 to 0.2. Lifetimes with respect to decarboxylation are compared to estimated OH lifetimes for oxaloacetic acid. The main result is that dark decarboxylation competes efficiently with other sink mechanisms for these types of molecules.

Chapter 3 explores the effect of common atmospheric solutes on the aqueous-phase aging of SOA. SOA from  $\alpha$ -pinene or  $\alpha$ -humulene ozonolysis was produced as representative monoterpene or sesquiterpene SOA, respectively, and aged in solutions of 0.010 mM  $\text{H}_2\text{O}_2$ , 0.15 mM  $\text{NaNO}_3$ , or 0.15 mM  $\text{NH}_4\text{NO}_3$  with or without photolysis. The SOA composition was monitored over time using direct infusion electrospray ionization high-resolution mass spectrometry. The results from this study have implications for the role of salts in the aging of SOA dissolved in cloud and fog water.

Chapter 4 investigates the differences in the photodegradation of toluene high-NO<sub>x</sub> SOA in various atmospheric matrices. Toluene SOA was prepared in a smog chamber by photooxidation in the presence of NO<sub>x</sub>. The SOA was collected and photolyzed under different conditions: directly on the filter, dissolved in pure water, and dissolved in 1 M ammonium sulfate. UV-Visible spectroscopy and electrospray ionization high-resolution mass spectrometry coupled to liquid chromatography separation were used to observe changes in MAC and composition during irradiation. The results show that the SOA absorption coefficient lifetime and lifetimes of individual chromophores in SOA will depend strongly on the matrix during aging.

This thesis explores the aging of SOA compounds in a range of atmospherically-relevant matrices. It is demonstrated that both dark and photochemical aging processes can be affected by the surrounding matrix. Changes in both the aging mechanisms and rates are observed as compared to in aqueous solution. It is concluded that understanding the influence of the matrix during aging is crucial in determining the fates of both individual compounds and complex SOA particles in the atmosphere.

## Chapter 2

# Effect of Ammonium Salts on the Decarboxylation of Oxaloacetic Acid in Atmospheric Particles

Reprinted with permission from Klodt, A.L.; Zhang, K.; Olsen, M.W.; Fernandez, J.L.; Furch, F.; Nizkorodov, S.A., Effect of ammonium salts on the decarboxylation of oxaloacetic acid in atmospheric particles, *American Chemical Society Earth and Space Chemistry*, **2021**, 5(4), 931-940, <https://doi.org/10.1021/acsearthspacechem.1c00025>. Copyright 2021 American Chemical Society.

### 2.1 Abstract

Oxaloacetic acid (OAA) is a 3-oxocarboxylic acid formed from the oxidation of succinic acid. OAA and other 3-oxocarboxylic acids experience a decarboxylation reaction in aqueous solutions which can be catalyzed by ammonium and amines. This catalysis has not been

studied under atmospherically relevant conditions despite interest in OAA in the atmosphere. To address this, 1 mM solutions of OAA were prepared with varying concentrations of ammonium sulfate, ammonium bisulfate, ammonium chloride, and sodium sulfate to simulate various atmospheric conditions. The extent of the decarboxylation was monitored using UV-Visible absorption spectroscopy. OAA's uncatalyzed decarboxylation lifetime was around 5 h. Under moderately acidic conditions representative of aerosol particles (pH = 3-4), the decarboxylation rate increased linearly with ammonium concentration up to about 2.7 M, after which additional ammonium had no effect. The effective lifetime of OAA reduced to approximately 1 h under these conditions. Density functional theory calculations support the proposed catalytic mechanism, predicting the free energy barrier height for decarboxylation to be approximately 21 kcal mol<sup>-1</sup> lower after OAA has reacted with ammonium. In more acidic solutions (pH<1), OAA's decarboxylation was suppressed, with lifetimes of tens of hours, even in the presence of ammonium. Comparison of the decarboxylation rate with the expected rate of oxidation by OH suggests that decarboxylation will be the dominant loss mechanism for OAA, and presumably other 3-oxocarboxylic acids, in aerosol particles and cloud/fog droplets. This result explains why OAA is difficult to detect in field measurements even though it is a known oxidation product of succinic acid.

## 2.2 Introduction

The importance of secondary organic aerosol (SOA) formation and aging has been recognized based on SOA's ability to affect climate, air quality, and health.<sup>2</sup> SOA is generally comprised of molecules containing carbonyl, carboxyl, and hydroxyl functional groups.<sup>10</sup> Oxocarboxylic acids and dicarboxylic acids comprise a major fraction of SOA mass as a result of their low vapor pressures.<sup>19</sup> Their abundance in atmospheric water is also high as a result of their high polarity.<sup>82</sup> Their prevalence in SOA and water solubility makes dicarboxylic acids, ox-

oxocarboxylic acids, and oxodicarboxylic acids (molecules that have two carboxyl groups and at least one keto group) good representative molecules for SOA found in the aqueous phase, such as aerosol liquid water or cloud droplets, and studying their possible aqueous reactions is important for understanding the fate of SOA constituent molecules dissolved in atmospheric water.<sup>19,49,50,83–87</sup>

The ionic strengths for atmospheric water generally fall between  $10^{-5}$  and  $10^{-2}$  M for cloud/fog water and in excess of 1 M in deliquescent aerosol particles.<sup>49</sup> The major contributors to the ionic strength are sulfate and ammonium ions, especially in areas dominated by anthropogenic emissions of ammonia and sulfur dioxide,<sup>50</sup> although other inorganic ions including nitrate, chloride, and sodium also contribute. These hygroscopic species have the potential to affect the chemistry of SOA in the aqueous phase through various mechanisms. Ammonium ions are especially interesting in this regard because they directly affect the pH, and they can act as a catalyst for various processes by reacting with carbonyl and other oxygen-containing groups.<sup>63,64</sup> One such ammonium-catalyzed process is the main focus of this work.

Oxaloacetic acid (OAA) is a 3-oxodicarboxylic acid – a class of compounds which are known to undergo the decarboxylation reaction shown in simplified Figure 2.1. OAA can be formed by the oxidation of succinic acid,<sup>88</sup> which is prevalent in the atmosphere,<sup>83,84</sup> and OAA has recently been observed in atmospheric aerosols.<sup>86,87,89</sup> Previously, the decarboxylation reaction of 3-oxocarboxylic acids has been suggested by Römpf et al.<sup>85</sup> to explain the absence of 3-oxodicarboxylic acids detected in field data, despite their assumed formation and detection in laboratory-generated SOA. In fact, it has been known for some time that OAA’s decarboxylation reaction can be catalyzed by ammonium and other amines.<sup>90</sup> Since OAA is an important molecule in the citric acid cycle,<sup>91</sup> this decarboxylation reaction and response to ammonium and amines has been reported in previous studies, usually under more neutral or basic conditions and ionic strengths and temperatures more representative of the human

body.<sup>92–95</sup> The behavior of OAA under the higher ionic strength conditions of deliquescent aerosol particles has not been studied.

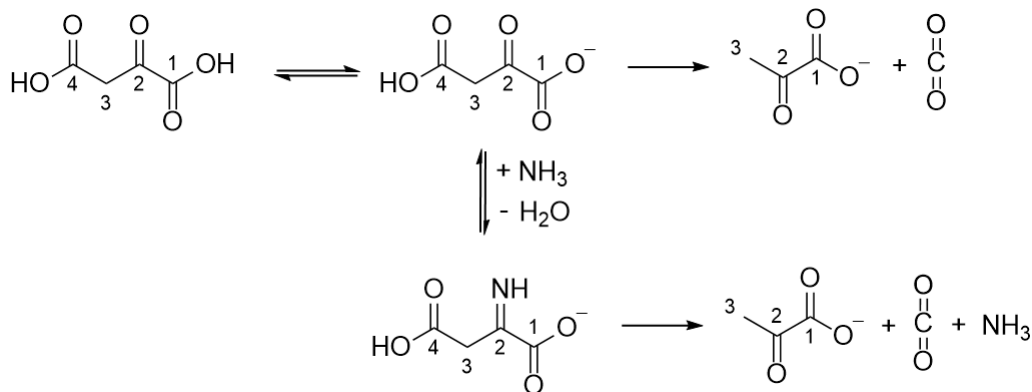


Figure 2.1: The decarboxylation reaction of OAA reported by Thalji et al.<sup>95</sup> adjusted to represent majority species at pH 3 to 4 by not deprotonating the carboxylic acid at carbon 4. The reaction is catalyzed by forming an imine as shown.

The ammonium-catalyzed decarboxylation of OAA has not been studied with theoretical methods. Previous theoretical calculations have provided many mechanistic insights into the catalysis of reactions by diamines, although with the important limitation that they do not exhaustively explore possible decarboxylation pathways. Song et al.<sup>96</sup> reported a detailed mechanism and proton-transfer pathway for the uncatalyzed and ethylenediamine-catalyzed decarboxylation of undissociated OAA in the gas phase and aqueous phase proposed using semilocal density functional theory (DFT). They found an uncatalyzed free energy barrier of about 24 kcal mol<sup>-1</sup> and an ethylenediamine-catalyzed free energy barrier of approximately 14 kcal mol<sup>-1</sup>, and the dehydration of the carbinolamine to form an imine was the rate-limiting step for the catalyzed reaction. A detailed mechanism for fully deprotonated OAA at pH 8.0 with and without catalysis by protonated ethylenediamine was calculated by Cheng et al.<sup>97</sup> When fully deprotonated, the dehydration of the carbinolamine was still the rate-limiting step, but the free energy barrier was greater: 49 kcal mol<sup>-1</sup> with ethylenediamine catalysis (the free energy barrier and rate-limiting step without a catalyst were not discussed). Finally, Fan et al.<sup>98</sup> used DFT to compare several protonated diamine catalysts in the decar-

boxylation of OAA's anions ( $\text{OAA}^-$  and  $\text{OAA}^{2-}$ ). They calculated the decarboxylation step to have the highest free energy for  $\text{OAA}^{2-}$  in the presence of all diamine catalysts, while the dehydration of the carbinolamine was rate-determining for  $\text{OAA}^-$  with most of the catalysts.

Here the chemistry of OAA in the presence of varying, atmospherically relevant concentrations of  $\text{NH}_4^+$  and  $\text{SO}_4^{2-}$ , as well as  $\text{Na}^+$  and  $\text{Cl}^-$  for comparison, simulating a number of aqueous conditions found in the atmosphere, is studied. Electronic structure calculations are also reported in order to generate the energy diagrams of both the uncatalyzed and ammonium-catalyzed decarboxylation of OAA. It is proposed that the ammonium-catalyzed reaction goes through a six-membered ring transition state which is analogous to the known transition state of the uncatalyzed reaction, as presented in Figure 2.2. The activation energies of both mechanisms are compared to validate the experimental results. It is shown that decarboxylation in the presence of ammonium occurs on time scales of hours, and therefore controls the lifetime of OAA, and likely all other 3-oxocarboxylic acids, in the presence of ammonium sulfate aerosols.

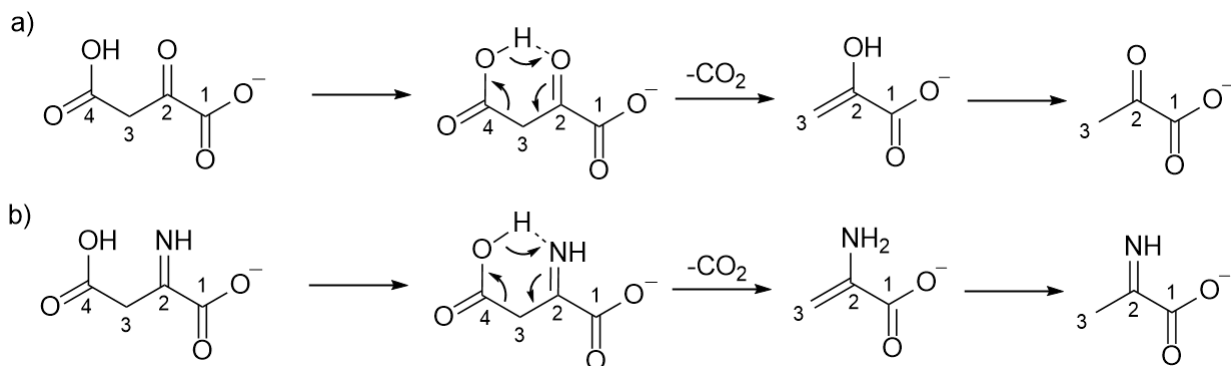


Figure 2.2: The proposed mechanism for OAA's decarboxylation including the six-membered ring transition state a) without catalyst and b) in the presence of ammonium.

## 2.3 Materials and Methods

### 2.3.1 Sample Aging

OAA (97% purity) was purchased from Millipore Sigma. Ammonium sulfate (99% purity), ammonium bisulfate (98% purity), ammonium chloride (99% purity), and sodium sulfate (99% purity) were purchased from Fisher Scientific. All compounds were used without further purification. OAA was dissolved in pure Milli-Q water or solutions of varying concentrations of ammonium sulfate, ammonium bisulfate, sodium sulfate, or ammonium chloride to make 1 mM solutions of OAA. The OAA dissolved promptly upon contact with the solution, so minimal mixing was required. The time between solution preparation and the beginning of measurements was minimized (<5 min) to control the amount of time spent in the aqueous phase, allowing for the observation of as much of the decarboxylation reaction as possible. The rate of the decarboxylation reaction shown in Figure 2.1 was monitored using the peak in absorbance at 260 nm using a UV-Vis spectrometer (Shimadzu UV-2450) which was programmed to collect a spectrum at set time intervals, ranging from 10 to 30 min depending on the rate at which the absorbance decayed. The 1 mM OAA concentration was specifically chosen to provide a starting 260 nm absorbance around one to ensure a good signal-to-noise ratio. The starting concentration was not varied in these experiments since OAA exhibited first-order decay. The pH value for each starting sample was measured using a Mettler Toledo SevenEasy pH meter. The pH of the solutions did not change significantly throughout the experiments, which agrees with previous work.<sup>99,100</sup> A summary of experimental conditions and measured pH values is provided in Table 2.1.



Table 2.1: A summary of individual decarboxylation experiments performed: type of salt added to the experimental solution, the concentration of salt added, measured solution pH, calculated rate constant from pseudo-first-order fit (as well as the fit's standard deviation), the lifetime of OAA in this solution, and branching ratio to compare the lifetime of OAA with respect to OH-oxidation and decarboxylation. The rate constant and branching ratio calculations are discussed in the next section. Branching ratios are calculated at pH 3.7 for all conditions except solutions containing ammonium bisulfate, which are calculated at pH 1.

Salt Added	Salt Concentration (M)	pH	Rate Constant $\pm 1$ std dev ( $s^{-1}$ )	Lifetime (h)	Branching Ratio (Q)
none	0		$(4.57 \pm 0.01) \times 10^{-5}$	6.1	$6.53 \times 10^{-3}$
none	0	3.1	$(5.91 \pm 0.15) \times 10^{-5}$	4.7	$5.05 \times 10^{-3}$
$(NH_4)_2SO_4$	0.10		$(8.75 \pm 0.03) \times 10^{-5}$	3.2	$3.41 \times 10^{-3}$
$(NH_4)_2SO_4$	0.25	3.9	$(8.19 \pm 0.10) \times 10^{-5}$	3.4	$3.65 \times 10^{-3}$
$(NH_4)_2SO_4$	0.50	3.9	$(1.24 \pm 0.02) \times 10^{-4}$	2.2	$2.40 \times 10^{-3}$
$(NH_4)_2SO_4$	0.50		$(1.54 \pm 0.01) \times 10^{-4}$	1.8	$1.94 \times 10^{-3}$
$(NH_4)_2SO_4$	0.75	3.5	$(1.45 \pm 0.02) \times 10^{-4}$	1.9	$2.06 \times 10^{-3}$
$(NH_4)_2SO_4$	1.0	4.0	$(1.86 \pm 0.01) \times 10^{-4}$	1.5	$1.60 \times 10^{-3}$
$(NH_4)_2SO_4$	1.0	4.0	$(1.89 \pm 0.02) \times 10^{-4}$	1.5	$1.58 \times 10^{-3}$
$(NH_4)_2SO_4$	1.35	3.5	$(2.54 \pm 0.01) \times 10^{-4}$	1.1	$1.17 \times 10^{-3}$
$(NH_4)_2SO_4$	1.48	3.7	$(2.52 \pm 0.02) \times 10^{-4}$	1.1	$1.19 \times 10^{-3}$
$(NH_4)_2SO_4$	1.5	4.0	$(2.39 \pm 0.04) \times 10^{-4}$	1.2	$1.25 \times 10^{-3}$
$(NH_4)_2SO_4$	1.85	3.8	$(2.53 \pm 0.02) \times 10^{-4}$	1.1	$1.18 \times 10^{-3}$
$(NH_4)_2SO_4$	2.0	4.0	$(2.70 \pm 0.03) \times 10^{-4}$	1.0	$1.10 \times 10^{-3}$
$(NH_4)_2SO_4$	2.25	3.9	$(2.63 \pm 0.02) \times 10^{-4}$	1.1	$1.13 \times 10^{-3}$
$(NH_4)_2SO_4$	2.5	4.0	$(2.32 \pm 0.01) \times 10^{-4}$	1.2	$1.29 \times 10^{-3}$
$NH_4Cl$	0.25	3.1	$(6.92 \pm 0.12) \times 10^{-5}$	4.0	$4.31 \times 10^{-3}$
$NH_4Cl$	0.5	3.0	$(7.38 \pm 0.10) \times 10^{-5}$	3.8	$4.04 \times 10^{-3}$
$NH_4Cl$	1.0	3.0	$(9.11 \pm 0.16) \times 10^{-5}$	3.1	$3.28 \times 10^{-3}$
$NH_4Cl$	1.5	2.9	$(1.57 \pm 0.01) \times 10^{-4}$	1.8	$1.90 \times 10^{-3}$
$NH_4Cl$	2.0	2.9	$(1.97 \pm 0.09) \times 10^{-4}$	1.4	$1.51 \times 10^{-3}$
$NH_4Cl$	2.5	2.7	$(2.35 \pm 0.01) \times 10^{-4}$	1.2	$1.27 \times 10^{-3}$
$NH_4HSO_4$	0.5	1.3	$(8.05 \pm 0.12) \times 10^{-6}$	35.5	$4.23 \times 10^{-2}$
$NH_4HSO_4$	0.8	1.0	$(6.15 \pm 0.10) \times 10^{-6}$	45.2	$5.54 \times 10^{-2}$
$NH_4HSO_4$	1.5	0.4	$(4.49 \pm 0.03) \times 10^{-6}$	62.0	$7.60 \times 10^{-2}$
$NH_4HSO_4$	2.0	0.2	$(2.37 \pm 0.04) \times 10^{-6}$	117	$1.44 \times 10^{-1}$
$H_2SO_4$	0	1.0	$(4.36 \pm 0.04) \times 10^{-6}$	63.7	$7.82 \times 10^{-2}$
$Na_2SO_4$	0.25	3.5	$(5.83 \pm 0.05) \times 10^{-5}$	4.8	$5.11 \times 10^{-3}$
$Na_2SO_4$	0.75	3.5	$(3.55 \pm 0.10) \times 10^{-5}$	7.8	$8.39 \times 10^{-3}$
$Na_2SO_4$	1.0	3.5	$(5.44 \pm 0.04) \times 10^{-5}$	5.1	$5.48 \times 10^{-3}$
$Na_2SO_4$	1.34	3.5	$(4.94 \pm 0.03) \times 10^{-5}$	5.6	$6.03 \times 10^{-3}$

### 2.3.2 Rate Constant and Branching Ratio Calculations

Rate constants and standard deviations were determined by fitting the absorbance at 260 nm over time to a first-order rate law. Sample fits to the data are shown in Figures 2.4-2.6. The decarboxylation reaction has also been shown to be first order in previous studies.<sup>92,101</sup>

To determine the importance of the decarboxylation reaction relative to other loss processes, the measured rate constants were converted into lifetimes with respect to decarboxylation, and compared to calculated lifetimes with respect to oxidation by OH using the method described in Ref.<sup>102</sup> Below,  $Q$  is defined as the ratio of the rate of oxidation of OAA by OH to the rate of decarboxylation:

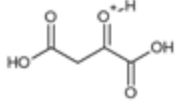
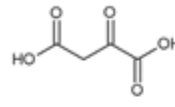
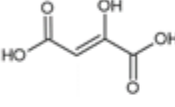
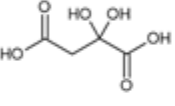
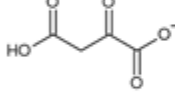
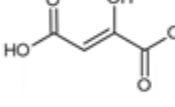
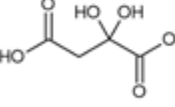
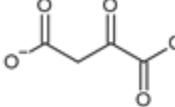
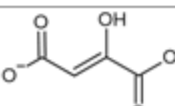
$$Q = \frac{\tau_d}{\tau_{OH}} = \frac{k_{OH} [OH]}{k_d} \quad (2.1)$$

where  $\tau_d$  is the lifetime of OAA with respect to decarboxylation,  $\tau_{OH}$  is the lifetime of OAA with respect to OH oxidation,  $k_{OH}$  is the bimolecular rate constant for OAA's reaction with OH, and  $k_d$  the measured unimolecular rate constant for OAA's decarboxylation. OH concentrations for deliquescent particles and cloud/fog water have been estimated to be  $10^{-16}$  to  $10^{-15}$  M.<sup>103-105</sup> Therefore, for the purposes of this comparison, OH concentration was assumed to be  $10^{-15}$  M for most of the discussion, although the implications of higher OH concentrations are addressed briefly.

The reaction rate of OAA with the OH radical has not been previously determined, so the structure-activity relationships (SARs) for aqueous OH-oxidation developed by Monod and Doussin<sup>106,107</sup> were used to estimate  $k_{OH}$  for OAA. OAA has multiple acid-base sites and can form a gem-diol or enol in the aqueous phase, so the mixture of compounds contributing to its OH reactivity is complex. Equilibrium ratios of all possible forms of OAA present in aqueous solutions at various pH values, shown in Table 2.2, were previously determined

by Kozłowski et al.<sup>94</sup> and were used here to determine a weighted rate constant for the OH-oxidation of OAA.

Table 2.2: The equilibrium ratios of OAA's forms in solution and the abundances as determined by Kozłowski et al.<sup>94</sup> at pH 3.7 and pH 1.

Structure	pH 3.7 (%)	pH 1 (%)
 Protonated keto form	0	3.4
 H <sub>2</sub> A keto form	0.2	10.6
 H <sub>2</sub> A enol form	0.4	3.4
 H <sub>2</sub> A gem-diol form	1.3	75.5
 HA <sup>-</sup> keto form	45.5	4.6
 HA <sup>-</sup> enol form	5.9	0.6
 HA <sup>-</sup> gem-diol form	19	1.9
 A <sup>2-</sup> keto form	24	0
 A <sup>2-</sup> enol form	3.2	0

The rate constants for the OH-oxidation of unsaturated compounds were not included in the SARs' training data set,<sup>106,107</sup> so the enol forms of OAA could not be calculated. Instead, the OH-oxidation rate of the closely related but-2-enedioic acid was used to estimate the OH reactivity of the enol forms of OAA. But-2-enedioic acid, which has the same structure as enol OAA with the exception of enol-OAA's vinylic alcohol group, reacts quickly with the OH radical ( $6 \times 10^9 \text{ M}^{-1} \text{ s}^{-1}$ ; see fumaric acid and maleic acid in Buxton et al.).<sup>108</sup> Additionally, but-2-enedioic acid only has two equivalent hydrogens which may be abstracted by OH, so the reactivity of each hydrogen should be about half of but-2-enedioic acid's total OH reactivity, or  $3 \times 10^9 \text{ M}^{-1} \text{ s}^{-1}$ . The OH reactivity of enol-OAA's vinylic hydrogen was therefore assumed to be equivalent to the reactivity of one of but-2-enedioic acid's vinylic hydrogens and the OH reactivity of enol-OAA's vinylic alcohol group to be  $6.9 \times 10^7 \text{ M}^{-1} \text{ s}^{-1}$ , which is the base value for alcohol groups in the SAR.<sup>106</sup> Charged species were also not included in the SARs' training data set, so the protonated keto form also could not be included in the calculation of the OH-oxidation rate constants. The values in Table 2.3, which shows the values used to estimate the rate constant for OAA's reaction with the OH radical, were renormalized to exclude it from the calculation. This is not expected to have a significant effect on the calculated OH-oxidation rate as the keto forms generally react an order of magnitude more slowly than the gem-diol forms,<sup>109</sup> and the protonated keto form only accounts for 3.4% of the abundance at pH 1 and is not present at pH 3.7.<sup>94</sup>

Table 2.3: Equilibrium ratios used to calculate OH rate constants, OH rate constants for individual OAA forms calculated from the SAR, and final estimated aqueous OH rate constants at pH 3.7 and pH 1.

Form	OH-oxidation rate constant ( $M^{-1}s^{-1}$ )	Ratio used for pH 3.7 (%)	Ratio used for pH 1 (%)
H <sub>2</sub> A keto form	$7.01 \times 10^6$	0.2	11.0
H <sub>2</sub> A enol form	$3.07 \times 10^9$	0.4	3.5
H <sub>2</sub> A gem-diol form	$2.61 \times 10^8$	1.3	78.2
HA <sup>-</sup> keto form	$1.23 \times 10^7$	45.5	4.8
HA <sup>-</sup> enol form	$3.07 \times 10^9$	5.9	0.6
HA <sup>-</sup> gen-diol form	$4.51 \times 10^8$	19.0	2.0
A <sup>2-</sup> keto form	$4.22 \times 10^7$	24	0
A <sup>2-</sup> enol form	$3.07 \times 10^9$	3.2	0
Final rate constant for OH oxidation		$2.98 \times 10^8 M^{-1}s^{-1}$	$3.41 \times 10^8 M^{-1}s^{-1}$

### 2.3.3 Computational Details

To further analyze the experimental results, electronic structure calculations were performed to obtain the energy diagrams for both the uncatalyzed and ammonium-catalyzed decarboxylation of OAA. The main goal of these simulations was to establish the mechanism for decarboxylation, rather than quantitatively predict the rate constants, using resource-efficient computational methodology. Geometries of the reactants, transition state intermediates, and products were fully optimized within DFT using the hybrid exchange correlation functional of Perdew, Burke, and Ernzerhof (PBE0)<sup>110</sup> in combination with the resolution-of-identity (RI) approximation.<sup>111</sup> PBE0 has been shown to give acceptably accurate barrier heights based on previous work,<sup>102</sup> so in the interest of computational cost, other hybrid exchange correlation functionals were not tested. Polarized triple-zeta valence basis sets (def2-TZVPP)<sup>112</sup> were used for all atoms. Very fine size four (grids) was used for numerical integration, and ground state energies converged to  $10^{-8}$  Ha.<sup>113</sup> Analytical second derivative (Aoforce)<sup>114</sup> calculations were performed to confirm that all optimized structures were minima of the potential energy surface. In addition to calculations for isolated molecules, calculations for molecules in

a dielectric medium were also performed. To this end, the conductor-like screening model (COSMO)<sup>115</sup> was employed with the dielectric constant for water, 80.1.<sup>116</sup> For each proposed mechanism, a search for transition states was performed by scanning the ground state potential energy surface along the carbon C<sub>3</sub>-C<sub>4</sub> bond distance, followed by an unconstrained transition state optimization. The validity of the transition state structures was checked using numerical finite differences of analytical gradients<sup>117</sup> to ensure there was one imaginary frequency. The Gibbs free energies of each species within the rigid-rotor harmonic oscillator approximation at 25 °C and 1 atm were subsequently calculated. Energy diagrams for OAA's decarboxylation were generated by setting the reference energy of all the reactants to zero. All electronic structure calculations were carried out with the TURBOMOLE electronic structure program suite, version V7.3.<sup>118</sup>

## 2.4 Results and Discussion

### 2.4.1 Sample Fits and Uncatalyzed Decarboxylation

A sample UV-Vis plot of OAA in water with the peak at 260 nm decreasing over the course of an experiment is shown in Figure 2.3. When monitoring the decarboxylation of OAA by UV-Vis, it can be seen in Figures 2.4-2.6 that the decrease at 260 nm is not strictly a first-order decay until after some time has passed, corresponding to the keto/enol and keto/gem-diol conversions both reaching equilibrium. Since the conversion between OAA's keto and gem-diol forms is faster in water than between the keto and enol forms,<sup>119</sup> it is likely the keto/enol interconversion that controls the change in the pre-equilibrium absorbance. However, the rate of keto/enol interconversion has not been determined at pH values lower than 5. At pH values above 5, the rate has been shown to be highly pH dependent,<sup>119</sup> so it would not be reasonable to apply rate constants obtained at higher pH values to the data. In any

case, the expected first-order kinetics are observed after the solution has had time to reach keto/enol equilibrium. To avoid interference from the solution equilibration, fitting began once the data had adopted a first-order decay pattern. The first point for the fit was chosen by performing sample fits beginning at each data point, then using the one with the earliest starting point with which the later fits agree within the standard deviation of the chosen fit. This difference is small under conditions of high ammonium concentration (0 to 5% – Figure 2.5), but much larger with low ammonium concentrations (5 to 10% – Figure 2.4) and/or high acidity (10 to 25% – Figure 2.6).

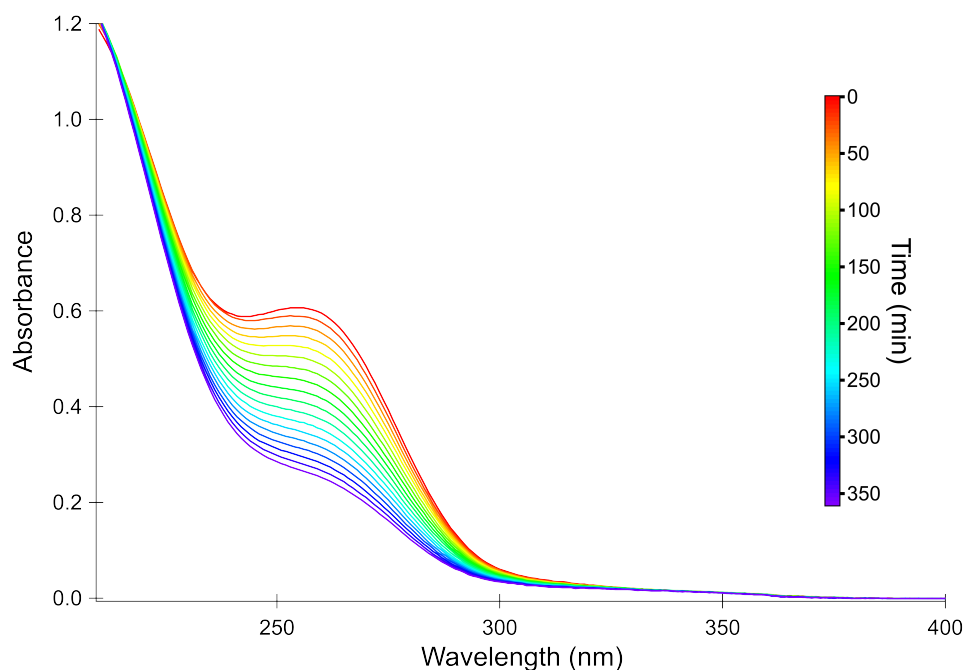


Figure 2.3: The absorption spectrum of OAA in water over time.

The uncatalyzed rate constant (Figure 2.4) for the decarboxylation was determined to be  $(5.24 \pm 0.95) \times 10^{-5} \text{ s}^{-1}$  as an average and standard deviation of two measurements, which shows good agreement with previous work ( $5.5 \times 10^{-5} \text{ s}^{-1}$ ).<sup>94</sup> This gives OAA a lifetime of about 5 h in a dilute aqueous solution, such as a cloud droplet. This is more than two orders of magnitude shorter than the lifetime with respect to the oxidation by OH in cloud/fog water (predicted  $Q = 0.005$ ), so decarboxylation will be the major removal pathway for aqueous OAA under these conditions.

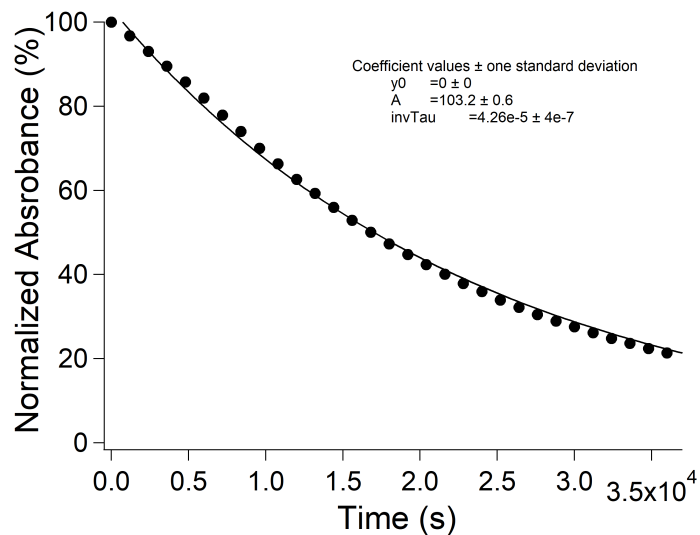


Figure 2.4: Absorbance at 260 nm, normalized to time 0, for 1 mM OAA in pure water. The data is shown with individual dots and the fit with a solid line.

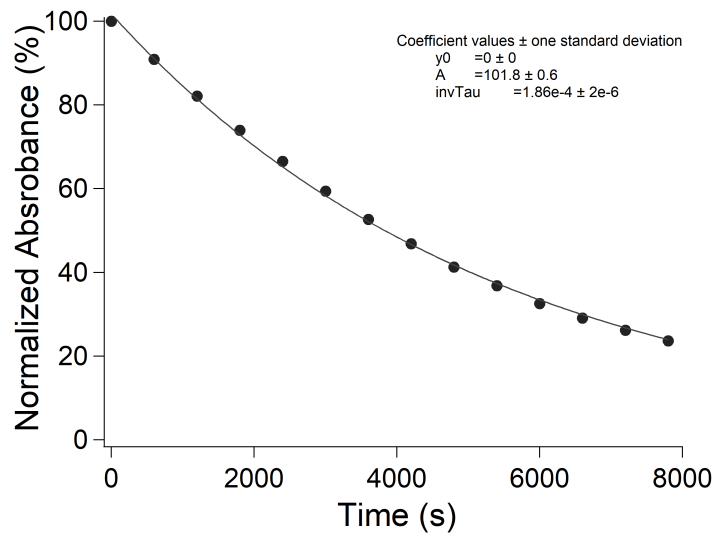


Figure 2.5: Absorbance at 260 nm, normalized to time 0, for 1 mM OAA in 1 M ammonium sulfate solution. The data is shown with individual dots and the fit with a solid line.



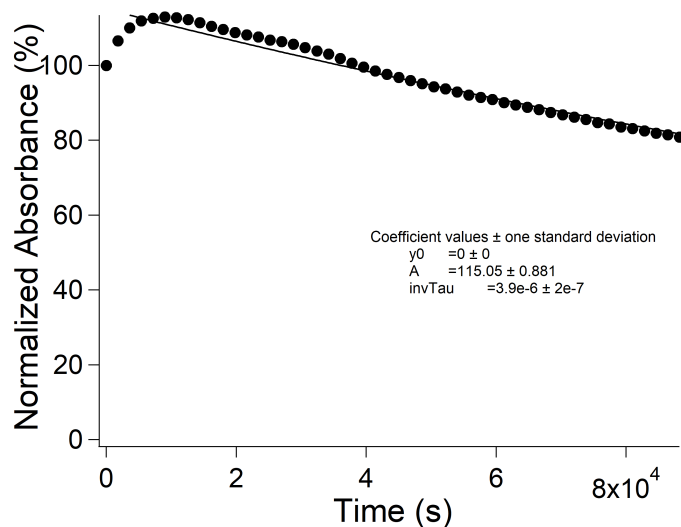


Figure 2.6: Absorbance at 260 nm, normalized to time 0, for 1 mM OAA in 1.54 M ammonium bisulfate solution. The data is shown with individual dots and the fit with a solid line.

## 2.4.2 Effects of Ammonium in Weakly Acidic Solutions (pH 3-4)

The measured pseudo-first-order rate constants ( $k$ ) and their dependence on salt concentrations are shown in Figure 2.7. The rate constants are plotted as functions of cation (ammonium or sodium) concentration rather than the overall ionic strength because it is observed that ammonium ion concentration better correlates with changes in the observed rate constants. An increase in ammonium sulfate linearly increases the rate constant for the decarboxylation reaction, with a slope of about  $7 \times 10^{-5} \text{ s}^{-1}$  per molar ammonium. The dependence of the rate on ammonium concentration appears to reach an asymptote above about 2.7 M ammonium. The lifetime of OAA at the point the rate levels off is about 1 h. It was confirmed using the E-AIM model II (<http://www.aim.env.uea.ac.uk/aim/aim.php>) that the activity of ammonium ion increases smoothly with ammonium sulfate concentration over this concentration range, so the saturation above 2.7 M is not due to the changes in activity of ammonium ion.

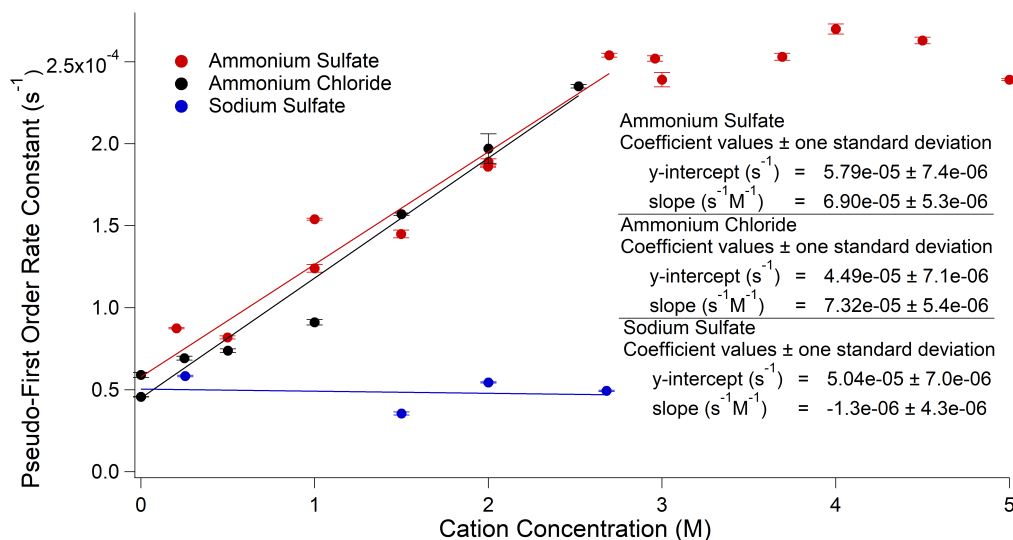


Figure 2.7: Pseudo-first order rate constants for the decay of OAA's absorbance peak at 260 nm as a function of cation concentration (ammonium concentration for ammonium sulfate and ammonium chloride; sodium concentration for sodium sulfate). The data for ammonium sulfate is shown in red, ammonium chloride in black, and sodium sulfate in blue. Error bars represent standard deviations computed from the individual fits. As the temperature and pH were not intentionally fixed, some spread in the rate constants obtained may be expected due to variations in the room temperature or differences in the solution pH. This particularly applies when comparing the ammonium sulfate (pH =  $3.7 \pm 0.3$ ) and ammonium chloride conditions (pH =  $3.0 \pm 0.3$ ). See Table 2.1 for more detailed information on the pH of individual experimental trials.

Figure 2.7 compares the measured rate constant for both ammonium sulfate and ammonium chloride. The dependence of the measured rate constant on ammonium ion concentration is the same regardless of whether the sulfate or chloride salt of ammonium is used, so there are no strong anion effects on decarboxylation. Control experiments were performed based on previous work which has shown some atmospheric aqueous processes to be influenced by ionic strength.<sup>49,65,66,120</sup> However, the rate constant for decarboxylation does not show a dependence on salt concentration with the addition of sodium sulfate. While the data is not plotted as a function of ionic strength in Figure 2.7, the ionic strength increases with increasing sodium sulfate concentration, so it can be concluded that the reaction is not appreciably affected by ionic strength in this case.

The observed behavior of the effective rate constant on  $[\text{NH}_4^+]$  can be explained if it is assumed that ammonia present in solution converts a small fraction of the carbonyl species into imine (Figure 2.1), which then decarboxylates at a much higher rate (Figure 2.2). The measured relative rate of decarboxylation in the presence and absence of dissolved ammonia in the limit of a rapid imine-carbonyl equilibrium can be expressed as follows:

$$\frac{\text{Rate}_{\text{withNH}_3}}{\text{Rate}_{\text{withoutNH}_3}} = \frac{k_{\text{imine}} [\text{imine}] + k_{\text{carbonyl}} [\text{carbonyl}]}{k_{\text{carbonyl}} [\text{carbonyl}]} \approx 1 + \frac{k_{\text{imine}} K_{\text{eq}} [\text{NH}_3]}{k_{\text{carbonyl}}} \quad (2.2)$$

Here,  $[\text{carbonyl}]$  is the starting concentration of OAA,  $[\text{imine}]$  is the concentration of imine assumed to be a minority species in solution ( $[\text{imine}] \ll [\text{carbonyl}]$ ),  $k_{\text{carbonyl}}$  is the rate constant for decarboxylation from the carbonyl species (measured to be  $5.24 \times 10^{-5} \text{ s}^{-1}$ ),  $k_{\text{imine}}$  is the unknown rate constant for decarboxylation from the imine species, and  $K_{\text{eq}}$  is the equilibrium constant between the imine and carbonyl species.

$$K_{\text{eq}} = \frac{[\text{imine}]}{[\text{carbonyl}] [\text{NH}_3]} \quad (2.3)$$

Ammonia is a minor species in solution under acidic conditions, but its concentration can be calculated from the acid ionization constant  $K_a$  of the ammonium ion:

$$K_a = \frac{[\text{H}_3\text{O}^+] [\text{NH}_3]}{[\text{NH}_4^+]} = 5.6 \times 10^{-10} \quad (2.4)$$

Combining these equations results in a predicted proportionality of the relative decarboxylation rate on the ammonium ion concentration,

$$\frac{\text{Rate}_{\text{withNH}_3}}{\text{Rate}_{\text{withoutNH}_3}} = 1 + \frac{k_{\text{imine}} K_{\text{eq}}}{k_{\text{carbonyl}}} \times \frac{K_a [\text{NH}_4^+]}{[\text{H}_3\text{O}^+]} \quad (2.5)$$

This can be related to the pseudo-first-order rate constant shown in Figure 2.7

$$k_{effective} = k_{carbonyl} + k_{imine}K_{eq} \times \frac{K_a [NH_4^+]}{[H_3O^+]} \quad (2.6)$$

which is consistent with the observed linear dependence on  $[NH_4^+]$  below  $[NH_4^+] \approx 2.7$  M. The linearity breaks down at higher concentrations, likely because equilibrium equations (2.3) and/or (2.4) no longer work at high ionic strengths.

### 2.4.3 Effects of Ammonium in Highly Acidic Solutions (pH near or less than 1)

Pseudo-first-order rate constants were also measured for solutions of OAA with varying concentrations of ammonium bisulfate, shown in Table 2.4. These experiments showed much slower rates of decarboxylation. At these low pH values, there is a strong contribution by the gem-diol form of OAA,<sup>94</sup> which should decrease the decarboxylation rate because the most likely reaction intermediate requires the keto form.<sup>96</sup> In addition, the rate is suppressed by the low concentration of ammonia needed to produce the imine, resulting in anticorrelation between the effective rate constant and hydronium ion concentration (equation 2.6). As a control experiment, the decarboxylation rate of OAA was measured in an aqueous solution acidified to pH 1.0 with sulfuric acid in the absence of ammonium and a lifetime of 63.7 hours was found. This is longer than for the solution containing ammonia at the same pH 1.0 (45.2 hours), showing that ammonia does still catalyze the decarboxylation even at these highly acidic pH values. However, the catalytic effect of ammonia is not strong enough to counteract the suppression of the decarboxylation rate by the increased acidity.

Table 2.4: Data from individual decarboxylation reactions in the presence of ammonium bisulfate.

Ammonium Bisulfate Concentration (M)	Solution pH	Rate Constant $\pm 1$ std dev ( $s^{-1}$ )	Lifetime (h)
0 ( $H_2SO_4$ added)	1.0	$(4.36 \pm 0.04) \times 10^{-6}$	63.7
0.5	1.3	$(8.05 \pm 0.12) \times 10^{-6}$	35.5
0.8	1.0	$(6.15 \pm 0.10) \times 10^{-6}$	45.2
1.5	0.4	$(4.49 \pm 0.03) \times 10^{-6}$	62.0
2.0	0.2	$(2.37 \pm 0.04) \times 10^{-6}$	117

Although the gem-diol reacts more readily with the OH radical than the keto form of OAA, decarboxylation is still the faster process at an OH concentration of  $10^{-15}$  M, with branching ratio Q ranging from 0.042 for 0.5 M ammonium bisulfate to 0.14 for 2.0 M ammonium bisulfate. If particle OH concentrations are higher, for instance  $10^{-12}$  M as suggested by Ervens et al. in their 2011 review,<sup>121</sup> OH oxidation lifetimes would be much shorter, and the branching ratios would shift to 42 for 0.5 M ammonium bisulfate and 140 for 2.0 M ammonium bisulfate. The importance of OAA’s decarboxylation reaction will therefore be highly OH-concentration dependent under acidic conditions, as acidity greatly decreases the decarboxylation rate.

#### 2.4.4 Electronic Structure Calculations

Electronic structure calculations were performed by Kimberly Zhang. Two possible reaction pathways for the ammonium-catalyzed decarboxylation of OAA are presented in Figure 2.8, one starting from the imine form and one starting from the enamine form of the reaction intermediate. Because most of the experiments were conducted at pH 3 to 4, which is higher than the pKa at carbon 1 (pH = 2.15) and lower than the pKa at carbon 4 (pH = 4.06),<sup>122</sup> the simulations were begun with the mono-deprotonated form of OAA as this should be the majority species in solution. To determine which of these pathways is more thermodynamically favorable, the stability of both compounds was compared to that of the

decarboxylation enamine product. In the gas phase, the starting enamine species has a lower free energy ( $5 \text{ kcal mol}^{-1}$ ) than the imine ( $7 \text{ kcal mol}^{-1}$ ) relative to the product. However, the energy order switches in the aqueous phase ( $14 \text{ kcal mol}^{-1}$  for the imine versus  $9 \text{ kcal mol}^{-1}$  for the enamine). In both the gas and aqueous phases, the reaction is predicted to be exergonic.

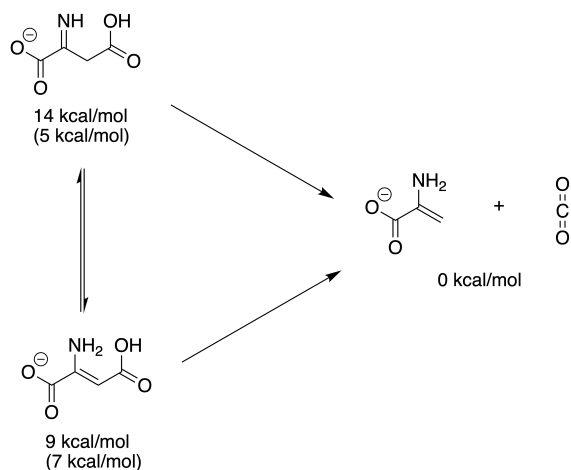


Figure 2.8: The electronic energies of species likely involved in the ammonium-catalyzed decarboxylation of OAA. The reference energy of the product was set to  $0 \text{ kcal mol}^{-1}$ , and the reference energy of the imine and enamine species were calculated accordingly. Values without and with parentheses are the relative free energies in the aqueous phase and the gas phase, respectively. All energies were calculated at PBE0/TZVPP level and reported in  $\text{kcal mol}^{-1}$ .

Figure 2.9 shows the energy diagrams for the ammonium-catalyzed and uncatalyzed decarboxylation processes in the gas and aqueous phases. The calculations found the transition state for the uncatalyzed decarboxylation is stabilized by the formation of a six-membered ring as shown in Figure 2.2 and Figure 2.9, in agreement with previous theoretical studies on the uncatalyzed decarboxylation of OAA and related molecules.<sup>96,123,124</sup>) The calculated activation energy of  $32 \text{ kcal mol}^{-1}$  for the aqueous-phase uncatalyzed reaction is higher than the experimentally determined activation energy of  $23.6 \text{ kcal mol}^{-1}$  reported by Ito et al.,<sup>100</sup> but still within a range expected of the lower target accuracy. The calculated energy barriers may be high because tunneling was not allowed for in the calculations. In the catalyzed re-

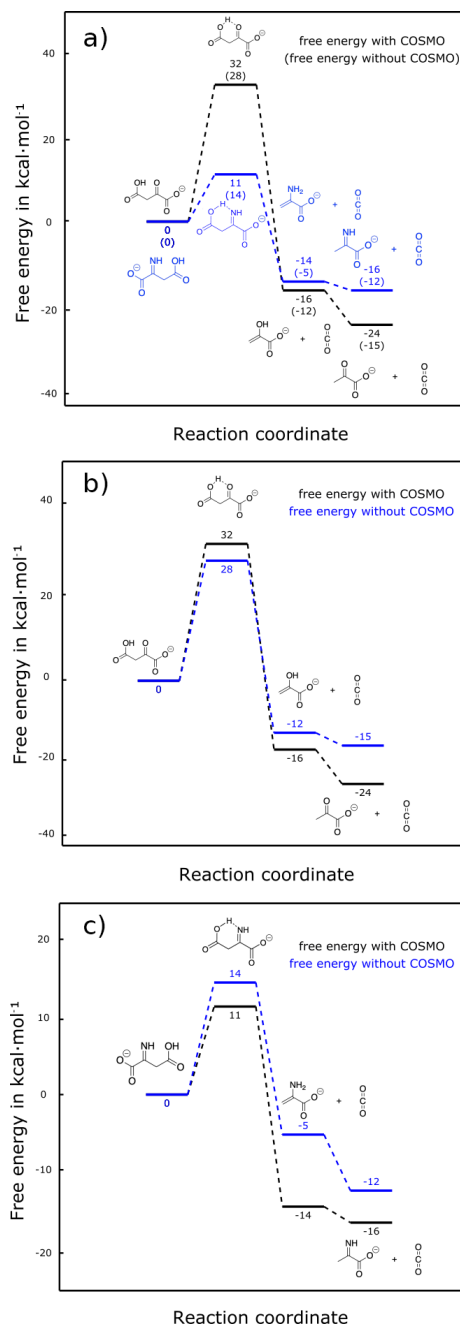


Figure 2.9: (a) Select stationary points of the uncatalyzed (black) and ammonium-catalyzed (blue) decarboxylation reaction of OAA. Values without and with parentheses are the relative free energies with COSMO (representing the aqueous phase) and without COSMO (representing the gas phase), respectively. (b) Select stationary points of the uncatalyzed decarboxylation of OAA without COSMO (gas phase) shown in blue and with COSMO (aqueous phase) shown in black. (c) Select stationary points of the ammonium-catalyzed decarboxylation of OAA without COSMO (gas phase) shown in blue and with COSMO (aqueous phase) shown in black. All energies were calculated at PBE0/TZVPP level and reported in kcal mol<sup>-1</sup>.

action, the decarboxylation proceeds from the imine form, and an analogous six-membered ring is formed for the ammonium-catalyzed transition state. The activation energy of the ammonium-catalyzed decarboxylation is significantly lower than that of the uncatalyzed decarboxylation in both the gas and aqueous phase, which is consistent with the relative experimental decarboxylation rates. Replacing OAA's carbonyl with an imine lowers the activation energy for decarboxylation, leading to shorter lifetimes in solutions containing ammonium. Comparing the gas and aqueous phase energy levels, it can also be seen from Figure 2.9 that the solvation effect of water stabilizes all the species except for the uncatalyzed transition state.

The Curtin-Hammett principle was used to calculate the relative free energies of the transition states ( $\Delta\Delta G^\ddagger$ ).<sup>125</sup>

$$\Delta\Delta G^\ddagger = \Delta G_{\text{carbonyl}}^\ddagger - \Delta G_{\text{imine}}^\ddagger + \Delta G_{\text{eq}}^\circ \quad (2.7)$$

$\Delta G_{\text{carbonyl}}^\ddagger$  and  $\Delta G_{\text{imine}}^\ddagger$  are the activation energies for decarboxylation from the carbonyl and imine, and  $\Delta G_{\text{eq}}^\circ$  is the free energy of the carbonyl and imine equilibrium (assumed to be achieved faster than the time scale of the decarboxylation process). The gas phase theoretical value of  $\Delta\Delta G^\ddagger$  is 14 kcal mol<sup>-1</sup>. Calculating  $\Delta\Delta G^\ddagger$  while including the dielectric constant of water to represent the aqueous phase gives 24 kcal mol<sup>-1</sup>.

The Curtin-Hammett principle also makes it possible to estimate  $\Delta\Delta G^\ddagger$  from the experimental results using the following equation:

$$\frac{k_{\text{imine}}K_{\text{eq}}}{k_{\text{carbonyl}}} = e^{\frac{\Delta\Delta G^\ddagger}{RT}} \quad (2.8)$$



Using equation (2.6), it was determined that  $k_{imine}K_{eq} = 12.5$  at pH of 4 (see Table 2.1 for experimental pH values) from the experimentally determined slope in Figure 2.7. Plugging this value into equation (2.8), along with the measured  $k_{carbonyl}$  rate constant, gave an experimental  $\Delta\Delta G^\ddagger$  value of about 7.3 kcal mol<sup>-1</sup>. The experimentally derived value is considerably lower than the theoretical value suggesting that the calculation overestimates the barrier height for the carbonyl species (by about 8 kcal mol<sup>-1</sup> as discussed above) but underestimates the barrier height for the imine species. It is also possible that other forms of OAA than the ones shown in Figure 2.2 can decarboxylate making the direct comparison between the theory and experiment more challenging. Despite these quantitative discrepancies, which may in part be due to the neglect of proton tunneling on the computed barriers, the computations support the experimental observations by suggesting that the decarboxylation reaction proceeds more efficiently along the catalyzed pathway due to a lower transition state energy along this pathway.

### 2.4.5 Effect of Ionic Strength on the Initial Absorbance Spectra

It has been demonstrated that increasing salt concentrations can affect the absorption spectra of aqueous molecules and impact their direct photolysis rates.<sup>65-68</sup> This prompted an examination of the effect of the added salts on the initial absorption spectrum of OAA before decarboxylation (Figures 2.10-2.13). For these Figures, although all solutions were prepared at close to 1 mM concentrations of OAA as possible, the actual concentration of each solution was used to scale each spectrum by 1 mM divided by the exact concentration to make the peak heights more directly comparable.

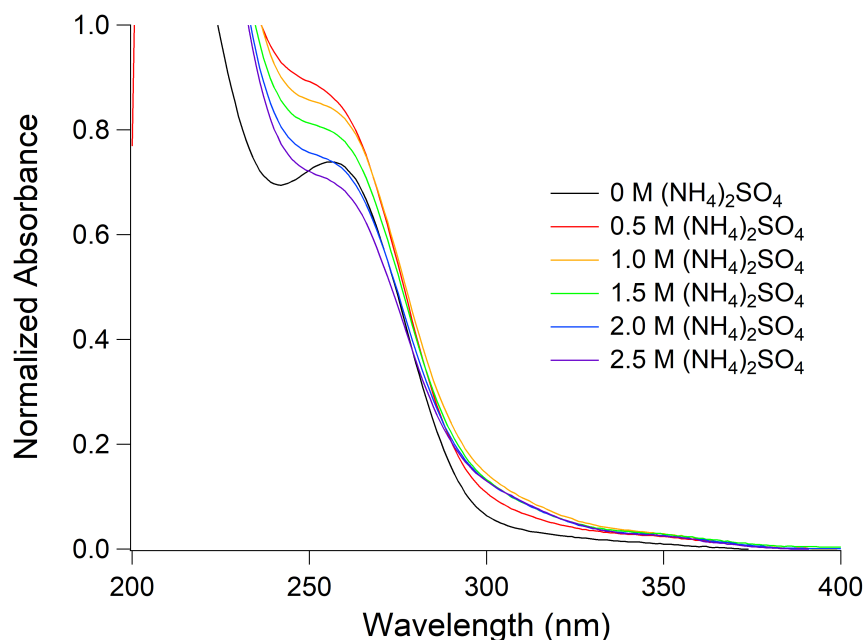


Figure 2.10: Initial absorbance spectra for solutions containing ammonium sulfate. 1 mM OAA without added salts is shown in black. Traces are also shown for 1 mM OAA in 0.5 M (red), 1.0 M (orange), 1.5 M (green), 2.0 M (blue), and 2.5 (purple) M ammonium sulfate.

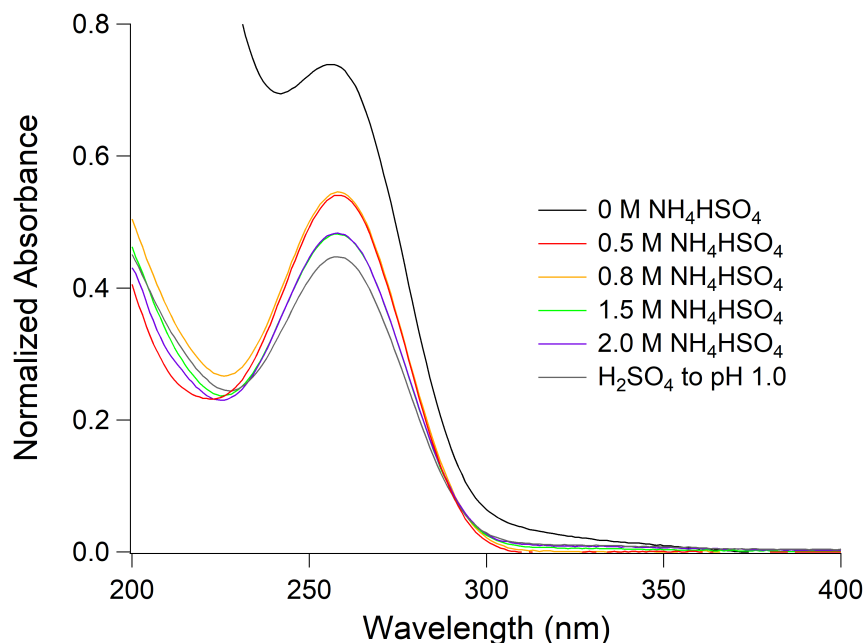


Figure 2.11: Absorbance spectra for OAA in ammonium bisulfate at their maximum value. 1 mM OAA without added salts is shown in black. Traces are also shown for 1 mM OAA in 0.5 M (red), 0.8 M (orange), 1.5 M (green), 2.0 M (purple) ammonium bisulfate, and acidified to pH 1.0 using sulfuric acid (gray).

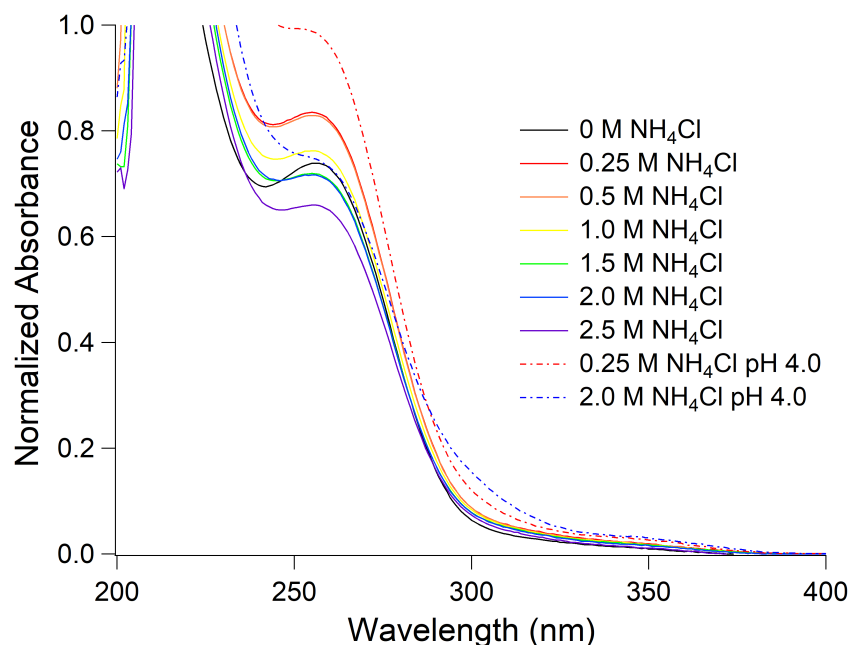


Figure 2.12: Initial absorbance spectra for solutions containing ammonium chloride. 1 mM OAA without added salts is shown in black. Traces are also shown for 1 mM OAA in 0.25 M (red), 0.5 M (orange), 1.0 M (yellow), 1.5 M (green), 2.0 M (blue), and 2.5 (purple) M ammonium chloride. The traces in dashed lines have the pH adjusted to 4.0 so that the enol band is present as in the ammonium sulfate conditions.

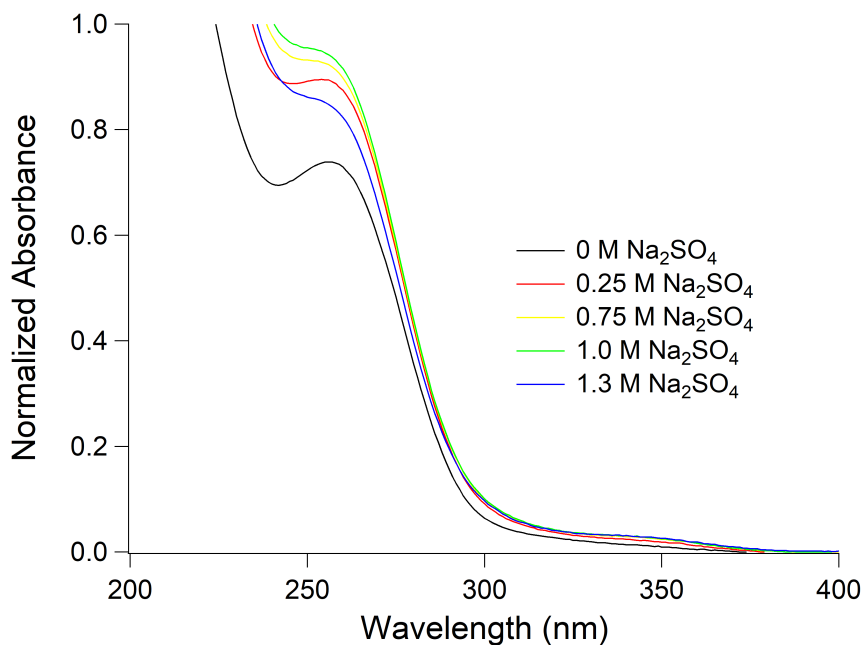


Figure 2.13: Initial absorbance spectra for solutions containing sodium sulfate. 1 mM OAA without added salts is shown in black. Traces are also shown for 1 mM OAA in 0.25 M (red), 0.75 M (yellow), 1.0 M (green), and 1.3 M (blue) M sodium sulfate.

In all conditions, the addition of small concentrations (less than 1 M) of salts resulted in an increase in the height of the main absorption peak at 260 nm. However, further addition of salt decreased the 260 nm absorption. The decrease holds true for the solutions containing sodium sulfate as well as for the solutions containing ammonium, so it is not attributable to faster decarboxylation with ammonium. This effect was not observed in previous studies on pyruvic acid<sup>65,67</sup> (another atmospherically important keto-acid and the product of the OAA decarboxylation) and is likely a result of changing OAA's complex equilibrium of species in solution. Since the enol form is the major absorbing species for OAA<sup>94</sup> any change in the enol concentration will change the absorption intensity. Other single-molecule experiments have shown that salts can affect absorption spectra by changing the ratios of species present in solution,<sup>66,67</sup> although these other studies have been on molecules with a less complex set of forms at equilibrium. A decrease in relative enol concentration explains why lowering the pH of the solutions (in the ammonium bisulfate and sulfuric acid conditions) significantly decreased the main absorption peak, as there is a greater fraction of gem-diol and a lower fraction of enol present at acidic conditions.<sup>94</sup> An additional consequence of increased acidity is reduced absorption above 300 nm. OAA will absorb less of the sun's energy under very acidic conditions (pH near or less than 1) than at more moderately acidic pH's, which may affect its photochemistry.

Another interesting effect is the growth of a shoulder on the main absorption peak with the addition of ammonium sulfate (Figure 2.10), providing more absorption of tropospherically-relevant wavelengths. This shoulder, characterized by an increase in absorbance between 270 and 315 nm, is attributable to the formation of an enamine,<sup>126</sup> which would be particularly interesting if the enamine form is not active in the decarboxylation process as could be the case based on these and previous calculations.<sup>96-98</sup> Therefore, enamine formation may be a potential pathway for direct photolysis to compete with OAA's decarboxylation. The enamine peak is only visible at pH values above about 3.5, as demonstrated by the ammonium

chloride-containing absorbance spectra (Figure 2.12). Since ammonium chloride is more acidic than ammonium sulfate or sodium sulfate, the ammonium chloride solutions were generally near pH 3 and the enamine peak was not present. However, when a drop of 1 N potassium hydroxide was added to the sample solution the pH changed from  $\sim 3$  to  $\sim 4$  and the enamine band became visible. It is clear from the comparison of the initial absorbance spectra that pH, ionic strength, and ionic species can alter the absorption spectrum of OAA significantly, and potentially affect its direct photolysis rate.

## 2.5 Conclusions

The decarboxylation rate of OAA was observed in solutions of ammonium and sulfate salts under varying concentrations and compared to the reaction rate in pure water, and electronic structure calculations were performed to validate the experimental results. At weakly acidic pH values, the rate at which OAA was converted to pyruvic acid linearly increased with the addition of ammonium up to about 2.7 M ammonium but had no further observable change in rate at higher ammonium concentrations. At pH values near and less than 1, the decarboxylation reaction rate was reduced by about an order of magnitude, although ammonium still catalyzed the reaction. Salts that did not contain ammonium did not accelerate the observed reaction. The DFT calculations performed suggest that the energy barrier for decarboxylation is significantly lower from the imine (after reaction with ammonium) than from the uncatalyzed carbonyl form:  $11 \text{ kcal mol}^{-1}$  compared to  $32 \text{ kcal mol}^{-1}$ .

When decarboxylation lifetimes were compared to the lifetimes of OAA with respect to OH oxidation under corresponding atmospheric conditions, decarboxylation was found to be dominant in nearly all cases. These results suggest that the lifetime of OAA will be highly dependent on the aqueous system in which it is dissolved. In dilute solutions (such as cloud

water) and aerosols with low ammonium concentrations, decarboxylation reactions of the type studied here will be ammonium (or amine) concentration dependent, but the exact ammonium concentration will not be as important in deliquescent particles in cases where the ammonium concentration is sufficiently high. At highly acidic pH values, the importance of decarboxylation will depend on the OH concentration, but decarboxylation is still likely to be the dominant removal pathway. The decarboxylation lifetimes calculated here can be summarized as follows: 5 hours in dilute water/weakly acidic water without ammonium ions, less than 5 hours and as short as 1 hour in water neutralized by ammonium, and tens of hours in more acidic waters.

Decarboxylation and OH oxidation do not exhaustively describe all possible fates for OAA in atmospheric water. For instance, reactions between carboxylic acids and ammonium or protonated amines have been shown to contribute to nanoparticle growth.<sup>127</sup> Formation of a carboxylate salt of this type with the carboxylic acid at OAA's carbon 4 would inhibit the decarboxylation pathway shown in Figure 2.2, suppressing decarboxylation in freshly nucleated particles. Sulfate-esterification may also occur in sulfate-containing atmospheric solutions, particularly at low pH values.<sup>128</sup> The methods presented here do not allow sulfate-esterification to be differentiated from decarboxylation in highly acidic conditions where sulfate-esterification is expected to gain in importance. However, formation of sulfate esters has been shown to result from the reactions of epoxides, while their formation from the reactions of alcohols (i.e., enol form of OAA) is kinetically unfavorable under atmospheric conditions.<sup>129,130</sup> Finally, small ketone-containing molecules can undergo aldol condensation catalyzed by the presence of ammonium,<sup>131</sup> which could also compete with decarboxylation. The rate of aldol condensation has not been measured for OAA, so the lifetimes of OAA with respect to decarboxylation and aldol condensation cannot be directly compared. However, rates of aldol condensation for other small carbonyl compounds are on the order of  $10^{-5}$  to  $10^{-7} \text{ s}^{-1}$  – one to three orders of magnitude slower than the decarboxylation of OAA is

predicted to be under similar conditions.<sup>63</sup> Therefore, decarboxylation is expected to be the most important process for OAA in atmospheric particles containing ammonium.

Decarboxylation is also expected to be an important removal pathway for other 3-oxocarboxylic acids, although the reactivity of OAA may not translate directly. Other 3-oxocarboxylic acids, such as acetoacetic acid and  $\alpha,\alpha$ -dimethylacetoacetic acid, have decarboxylation rates of the same order of magnitude as OAA in pure water,<sup>132,133</sup> and ammonium salts are expected to catalyze the decarboxylation reactions of other molecules similarly. However, the OH reactivity of these other molecules may differ from OAA. OAA has an especially unreactive keto form as a result of its structure (it only has one carbon where hydrogen atoms can be abstracted by OH radicals). However, it also has a strong tendency to form a gem-diol (which reacts more quickly with OH) and exists as an enol in small abundances (which reacts very readily with OH). Other molecules will likely have a more OH-reactive keto form, be less likely to form a gem-diol, and may not have an enol form. It will be useful for future work to determine if/how the structure of 3-oxocarboxylic acids affects the ammonium-catalyzed decarboxylation, and if OH oxidation becomes more important than decarboxylation for other 3-oxocarboxylic acids.

## Chapter 3

# Aqueous Photochemistry of Secondary Organic Aerosol of $\alpha$ -Pinene and $\alpha$ -Humulene in the Presence of Hydrogen Peroxide or Inorganic Salts

Reprinted with permission from Klodt, A.L.; Romonosky, D.E.; Lin, P.; Laskin, J.; Laskin, A.; Nizkorodov, S.A., Aqueous photochemistry of secondary organic aerosol of  $\alpha$ -pinene and  $\alpha$ -humulene in the presence of hydrogen peroxide or inorganic salts, *American Chemical Society Earth and Space Chemistry*, **2019**, 3(12), 2736-2746, <https://doi.org/10.1021/acsearthspacechem.9b00222>. Copyright 2019 American Chemical Society.



## 3.1 Abstract

The effect of common atmospheric solutes on the aqueous-phase aging of secondary organic aerosol (SOA) was explored under irradiated and dark conditions. SOA particles were produced from dark ozonolysis of  $\alpha$ -pinene or  $\alpha$ -humulene in a photochemical smog chamber, collected on filters, and extracted in either pure water or in aqueous solutions containing 0.010 mM  $\text{H}_2\text{O}_2$ , 0.15 mM  $\text{NaNO}_3$ , or 0.15 mM  $\text{NH}_4\text{NO}_3$ . These aqueous samples were then irradiated for up to four hours to simulate photochemical aqueous aging by sunlight or kept in the dark for the same amount of time to simulate nighttime aqueous chemistry of SOA. The chemical composition of the SOA was monitored over time using direct infusion electrospray ionization high-resolution mass spectrometry. The presence of salts accelerated the loss of high-molecular-weight compounds, both under irradiated and dark conditions, making the dissolved SOA compounds smaller and more volatile. These effects of atmospheric salts have important implications for understanding SOA evolution in cloud and fog water.

## 3.2 Introduction

Secondary organic aerosol (SOA) has a significant impact on human health and climate, and it is, therefore, important to understand how SOA particles are produced from volatile organic compounds (VOCs) and age during particle transport through the atmosphere.<sup>7</sup> Monoterpenes ( $\text{C}_{10}\text{H}_{16}$ ) are the major atmospheric SOA precursors with atmospheric concentrations of hundreds to thousands of ppt,<sup>11</sup> and SOA formation from various monoterpenes, particularly  $\alpha$ -pinene,<sup>4</sup> has been studied extensively.<sup>10,12-14</sup> There have also been studies on SOA formation from sesquiterpenes ( $\text{C}_{15}\text{H}_{24}$ ) such as  $\alpha$ -humulene,<sup>134</sup> which are less abundant in the atmosphere (measured to be tens of ppt)<sup>11</sup> but have greater SOA yield due to their higher molecular weights.<sup>1</sup> The lifetimes of monoterpenes and sesquiterpenes for reaction

with atmospheric oxidants are generally minutes to hours<sup>10</sup> and so they are quickly oxidized to compounds that can be soluble in cloud and fog water.

Chemistry occurring in fog and cloud droplets is known to be a significant factor in both the formation and aging of SOA.<sup>49</sup> For example, 5 to 60% of SOA globally is estimated to result from in-cloud processing,<sup>51</sup> and reactions occurring in the atmospheric aqueous phase have been proposed to explain the discrepancies in SOA oxidation level observed between laboratory and field studies.<sup>52,53</sup> Atmospheric fog and cloud waters often contain approximately 100  $\mu\text{g mL}^{-1}$  of dissolved carbon,<sup>48</sup> as well as aqueous oxidants, such as  $\text{H}_2\text{O}_2$  with normal concentrations of around  $10^{-6}$  M, and inorganic salts.<sup>49</sup> These inorganic salts, usually ammonium nitrate or ammonium sulfate, result in ionic strengths ranging from  $10^{-4}$  to  $10^{-2}$  M in fog water and  $10^{-5}$  to  $10^{-2}$  M in cloud water,<sup>49</sup> and can potentially affect the aging mechanisms of aqueous SOA. For instance,  $\text{NO}_3^-$  can serve as a photochemical source of OH radicals,<sup>61</sup>  $\text{NH}_4^+$  can react with carbonyls and act as a catalyst for various reactions,<sup>63,64</sup> and changing ionic strength can affect acid-base or other aqueous equilibria as salts can act as buffers in aqueous solutions. There have been only a few studies probing the effects of common inorganic salts on the aqueous-phase photochemical aging of SOA.<sup>65,66</sup>

Mechanisms of aqueous SOA aging can be photolytic or non-photolytic, and the photolytic processes can be further categorized as direct or indirect. The direct aqueous-phase photolysis of SOA extracts in pure water and in water/methanol mixtures has been examined in several studies.<sup>56-58,60</sup> The irradiation of SOA solutions resulted in a reduction in the average molecular size of SOA compounds driven by Norrish splitting of carbonyls and photolysis of peroxides.<sup>135,136</sup> Indirect photolysis occurs in parallel when reactions with sunlight produce reactive species, such as OH radicals, singlet oxygen, or triplet-excited states, and then these species react with SOA components. In contrast to the direct photochemical processes, the indirect processes normally result in more functionalized and less volatile products.<sup>39</sup> Non-

photolytic aging pathways include hydrolysis,<sup>34,35</sup> functional group exchange with inorganic ions, and reactions with other oxidizing solutes –  $\text{H}_2\text{O}_2$  in this work. In the hydrolysis of esters, the starting compounds are fragmented to smaller molecules with carboxyl and alcohol groups, resulting in smaller products with higher vapor pressures. Certain reactions with inorganic salts can decrease vapor pressure as salts are formed between carboxylic acids and inorganic cations.<sup>37,38</sup> Finally, the presence of  $\text{H}_2\text{O}_2$  can have a myriad of consequences. Neglecting its host of influences on photochemical reactions,  $\text{H}_2\text{O}_2$  is an important aqueous-phase oxidant,<sup>49</sup> its reactions with carbonyls and alcohols can produce peroxides,<sup>137</sup> it is well known to be an important part of sulfate formation from  $\text{SO}_2$ ,<sup>138</sup> and can be a source of radicals in the dark through Fenton-type reactions.<sup>139</sup>

Previous studies have explored the aging of SOA from various terpenes, including those studied here, in pure water.<sup>59,60</sup> The present work is intended to implement a more atmospherically relevant approach by adding solutes as would be present in atmospheric cloud and fog waters. Thus, the goals of this study are (1) to ascertain whether the photolysis and dark aging of aqueous SOA in the presence of common atmospheric solutes proceeds via a different mechanism compared to in the absence of these solutes and (2) to compare photolytic and dark aging of SOA in the presence of ionizable versus non-ionizable solutes. To accomplish these goals, aging of SOA produced from ozonolysis of a common monoterpene,  $\alpha$ -pinene (APIN), and a common sesquiterpene,  $\alpha$ -humulene (HUM), was studied using high-resolution mass-spectrometry after the SOA was aged in various conditions. These conditions included the presence or absence of both sunlight and solutes such as hydrogen peroxide (as a non-ionizable solute), sodium nitrate (an ionizable solute), and ammonium nitrate (an ionizable solute that also provides ammonium as a reactant).

## 3.3 Methods

### 3.3.1 Secondary Organic Aerosol Generation

APIN and HUM SOA were prepared through dark reaction with O<sub>3</sub> as described in previous papers.<sup>59,60,140</sup> APIN and HUM were purchased from Sigma-Aldrich at the highest available purity, and no further purification was performed. Approximately 600 ppb O<sub>3</sub> and 500 ppb of precursor were injected into a 5 m<sup>3</sup> teflon chamber, and ozonolysis was allowed to proceed under dry conditions at 21 to 25 °C without seed particles. These relatively high concentrations were necessary to obtain enough material for subsequent photochemical and mass spectrometric experiments. Particle sizes were monitored using a TSI model 3936 scanning mobility particle sizer (SMPS) and ozone concentrations were monitored using a Thermo Scientific model 49i ozone analyzer. An Aerosol Mass Spectrometer (AMS) was not used during the generation of the SOA used for aging, but AMS data was collected during the generation of HUM SOA produced under the same conditions for later solubility experiments. Aerosol particles were subsequently collected onto poly(tetrafluoroethylene) (PTFE) filters (Millipore 0.2 μm pore size) after passing through an activated carbon denuder with a flow rate of about 10 SLM (standard liters per minute). Two filter samples were collected over 2 to 3 h during each chamber experiment. A breakdown of SOA production details is provided in Table 3.1. After collection, the samples were vacuum sealed and frozen at -20 °C pending aqueous photolysis experiments.

Table 3.1: Conditions used for SOA preparation. SOA concentration represents the average during the collection of two sequentially collected filters, and so the concentrations are different.

Filter #	VOC	Initial VOC (ppb)	Initial O <sub>3</sub> (ppb)	Reaction Time (h)	Peak SOA concentration (mg m <sup>-3</sup> )	Collection time (h)	SOA collected (mg)
1	APIN	500	600	0.8	1.5	1.5	1.8
2	APIN	500	600	0.8	0.96	1.5	1.8
3	HUM	500	600	2	1.7	1	2.1
4	HUM	500	600	2	1.4	1	2.0

### 3.3.2 Secondary Organic Aerosol Aging Experiments

Samples were thawed, and each filter was extracted with 10 mL of HPLC-grade water. After sonicating for about 10 min, the water and SOA solutions were split into 4 aliquots of 2.5 mL and 100  $\mu$ L of concentrated aqueous oxidant or salt solution was added with final concentrations as shown in Table 3.2. No precipitation of SOA was observed after the addition of these small concentrations of salts, so it is not believed that the added salts had a significant impact on the SOA solubility. The concentrations in Table 3.2 assume complete dissolution of SOA. Under these conditions, all APIN SOA is expected to dissolve.<sup>141</sup> The solubility of HUM SOA in water was unknown, and the extraction efficiency was determined, as shown in Figure 3.1, to be about 40%. Because some HUM SOA remains undissolved after extraction with water, the results of these experiments only apply to the water-soluble fraction. Photolysis occurred similarly to previous work;<sup>60</sup> control samples were simultaneously aged under dark conditions. Briefly, a Xenon UV lamp (Newport model 66905) was used with a U-330 bandpass filter (Edmund optics #46-438) to decrease levels of hard UV, visible, and IR radiation. The majority of the radiation fell between 280 and 400 nm. Using the “Quick TUV”<sup>142</sup> calculator the lamp’s flux was determined to be comparable to that under ambient conditions. A full analysis is provided in Figure 3.2 and Table 3.3 in section 3.3.4. Therefore, the photolysis time under the UV lamp can be viewed as equivalent to photolysis in sunlight during summertime in Los Angeles. OH steady-state concentrations were determined to be

too low to have a significant effect on the aging of SOA, as they were estimated to be about  $10^{-18}$  M in all conditions where OH was produced (see section 3.3.5 below for further analysis). The photolysis and control (i.e., without photolysis) experiments were done for four hours. Samples of the solutions were taken once every hour for offline analysis using direct infusion electrospray ionization high-resolution mass spectrometry (ESI-HRMS).

Table 3.2: Summary of aqueous samples prepared from SOA filters. Aqueous SOA concentration assumes full dissolution of SOA.

VOC	Filter #	Aqueous oxidant/salt	Aqueous SOA concentration ( $\mu\text{g mL}^{-1}$ )	Aqueous oxidant/salt concentration (mM)
APIN	1	N/A	184	N/A
APIN	1	H <sub>2</sub> O <sub>2</sub>	177	0.010
APIN	2	NaNO <sub>3</sub>	180	0.15
APIN	2	NH <sub>4</sub> NO <sub>3</sub>	180	0.15
HUM	3	N/A	210	N/A
HUM	3	H <sub>2</sub> O <sub>2</sub>	202	0.010
HUM	4	NaNO <sub>3</sub>	196	0.15
HUM	4	NH <sub>4</sub> NO <sub>3</sub>	196	0.15

### 3.3.3 HUM SOA Extraction Efficiency

Figure 3.1 shows the results of a test of the extraction efficiency of HUM SOA from the filter. A filter with HUM SOA was first sonicated in 10 mL water for 10 min and an absorbance spectrum of the extract taken. Then the filter was removed from water and sonicated in 10 mL of methanol for 10 min. Based on the comparison of integrated absorbance over the 230-350 nm range, we estimate that approximately 40% of the SOA was dissolved in water, and the rest dissolved in methanol. This is to be contrasted with the dissolution of APIN SOA, for which the initial water extraction dissolved more than 90% of the material based on the study of Updyke et al.<sup>141</sup>(see supporting information Figure S3).

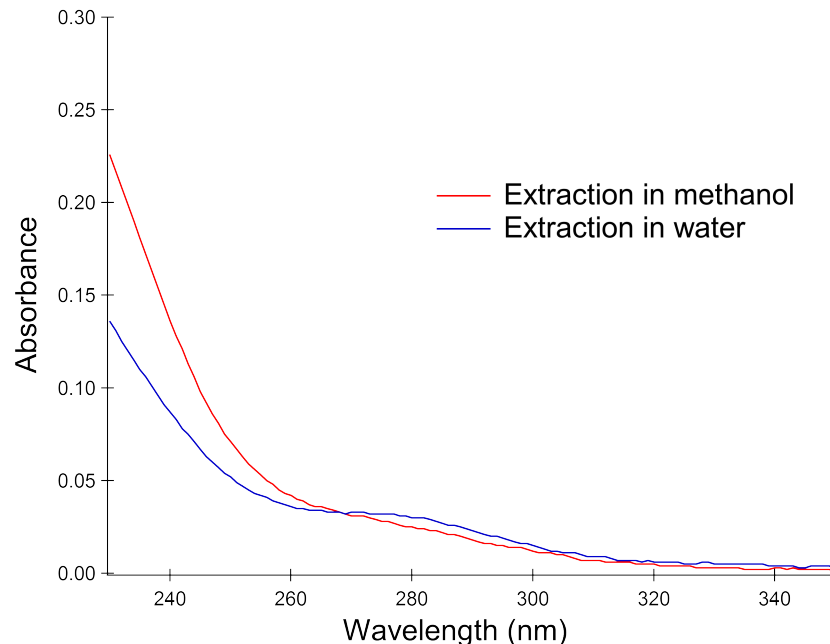


Figure 3.1: A test for the extraction efficiency of HUM SOA in water.

### 3.3.4 Light Flux Characterization

Figure 3.2 provides a comparison of the spectral flux densities of the photolysis lamp used in this project with the 24-hour averaged solar spectrum in June in Los Angeles, California and the solar spectrum at a solar zenith and of zero generated by the "Quick TUV calculator."<sup>142</sup> Table 3.3 provides an analysis of the relative integrated fluxes of the lamp used in the work as compared to the 24-hour average solar flux in June in Los Angeles.

The parameters used for the Quick TUV calculator were:

- Latitude/Longitude: 34 °N 118 °W or SZA = 0
- Date and Time: June 20, 2017
- Overhead Ozone: 300 du
- Surface Albedo: 0.1
- Ground Altitude: 0 km
- Measured Altitude: 0 km
- Clouds Optical Depth/Base/Top: 0.00/4.00/5.00

- Aerosols Optical Depth/S-S Albedo/Alpha: 0.235/0.990/1.000
- Sunlight Direct Beam/Diffuse Down/Diffuse Up: 1.0/1.0/0.0
- 4 streams transfer model

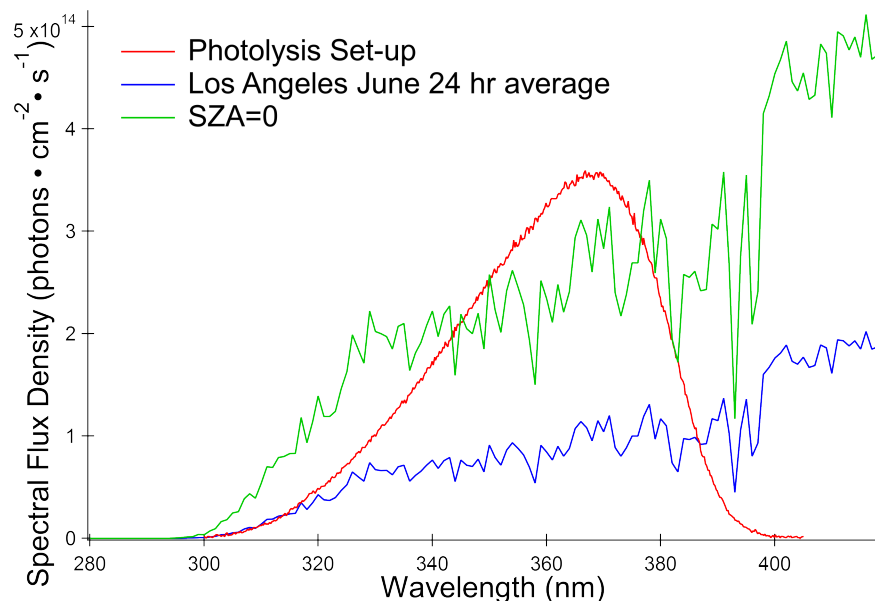


Figure 3.2: The spectral flux densities over the range of the electromagnetic spectrum of the photolysis set-up used in these experiments (in red), the 24-hour averaged solar spectrum in Los Angeles, California (Latitude/Longitude: 34°/118°) for the month of June (in blue), and the solar spectrum at a solar zenith angle (SZA) of zero (in green).

Table 3.3: The integrated fluxes and the number of hours equivalent to one hour under the photolysis set-up for the 24-hour average solar flux in June in Los Angeles. The calculation was performed by integrating the flux in Figure 3.2 for the three UV wavelength ranges that may potentially drive photochemistry. The values in the last column represent the ratios of the UV lamp’s integrated flux to the solar integrated flux.

Wavelength range of comparison	Integrated flux from our UV lamp (photons cm <sup>-2</sup> s <sup>-1</sup> )	Integrated flux from the 24h-average (photons cm <sup>-2</sup> s <sup>-1</sup> )	Equivalent hours at 24-h average sunlight in Los Angeles
UVB (280 to 315 nm)	$1.46 \times 10^{14}$	$1.72 \times 10^{14}$	0.85
UVB+UVA2 (280 to 340 nm)	$2.40 \times 10^{15}$	$1.54 \times 10^{15}$	1.56
Full UV (280 to 400 nm)	$1.54 \times 10^{16}$	$7.24 \times 10^{15}$	2.13



### 3.3.5 OH Steady-State Concentration Calculation

Approximate OH steady-state concentrations ( $[\text{OH}]_{\text{SS}}$ ) were calculated to understand the relative amounts of OH present with photolysis of  $\text{H}_2\text{O}_2$  and  $\text{NO}_3^-$  in the aqueous solutions. First, the rate constants for OH production were found using the following equation:<sup>143</sup>

$$j_x = \int 2.303 \times 10^3 \times F_\lambda \times \varepsilon_{x,\lambda} \times \phi_{\text{OH},\lambda} d\lambda \quad (x = \text{NO}_3^- \text{ or } \text{H}_2\text{O}_2) \quad (3.1)$$

where  $F_\lambda$  represents the surface area normalized photon flux ( $\text{mol-photon cm}^{-2}\text{s}^{-1}\text{nm}^{-1}$ ) with values shown in Figure 3.2,  $\varepsilon_{x,\lambda}$  is the base-10 molar absorptivity coefficient for  $x$  ( $\text{M}^{-1}\text{s}^{-1}$ ), and  $\phi_{\text{OH},\lambda}$  is the OH quantum yield. Values for  $\varepsilon_{x,\lambda}$  and  $\phi_{\text{OH},\lambda}$  were retrieved from the literature.<sup>144-147</sup> Calculated  $j$  values can be found in Table 3.4. Next, OH formation rates ( $R_{\text{OH}}$ ) were calculated by multiplying the production rate constant by the concentration of  $x$ . Finally,  $[\text{OH}]_{\text{SS}}$  was found by multiplying the OH production rate by the OH lifetime ( $\tau$ ), where  $\tau$  can be found via the following equation:

$$\tau = (k_{\text{SOA}} [\text{SOA}] + k_{\text{H}_2\text{O}_2} [\text{H}_2\text{O}_2])^{-1} \quad (3.2)$$

In the case of nitrate photolysis, the  $\text{H}_2\text{O}_2$  term will go to zero. The reaction of OH with SOA was assumed to be diffusion limited, and so  $1 \times 10^{10} \text{ M}^{-1}\text{s}^{-1}$  was used for  $k_{\text{SOA}}$ . The rate constant for OH reaction with  $\text{H}_2\text{O}_2$  was  $2.7 \times 10^7 \text{ M}^{-1}\text{s}^{-1}$ .<sup>148</sup> SOA concentrations were estimated using the average molar mass for each condition. The final  $[\text{OH}]_{\text{SS}}$  are shown in Table 3.4 below. They are too small to compete with direct photolysis under our experimental conditions.

Table 3.4: Values of interest for OH steady-state concentration calculation. Values for the concentration of SOA take into account extraction efficiency as described in Section 3.3.3.

SOA system	$J_x$ ( $s^{-1}$ )	$R_{OH}$ formation ( $M s^{-1}$ )	[SOA] (mM)	$\tau$ (s)	Theoretical [OH] <sub>ss</sub> (M)
APIN + H <sub>2</sub> O <sub>2</sub>	$1.8 \times 10^{-6}$	$1.8 \times 10^{-11}$	0.66	$1.5 \times 10^{-7}$	$2.7 \times 10^{-18}$
APIN + NaNO <sub>3</sub>	$1.3 \times 10^{-7}$	$2.0 \times 10^{-11}$	0.76	$1.3 \times 10^{-7}$	$2.7 \times 10^{-18}$
APIN + NH <sub>4</sub> NO <sub>3</sub>	$1.3 \times 10^{-7}$	$2.0 \times 10^{-11}$	0.77	$1.3 \times 10^{-7}$	$2.6 \times 10^{-18}$
HUM + H <sub>2</sub> O <sub>2</sub>	$1.8 \times 10^{-6}$	$1.8 \times 10^{-11}$	0.30	$3.7 \times 10^{-7}$	$6.0 \times 10^{-18}$
HUM + NaNO <sub>3</sub>	$1.3 \times 10^{-7}$	$2.0 \times 10^{-11}$	0.28	$3.5 \times 10^{-7}$	$7.0 \times 10^{-18}$
HUM + NH <sub>4</sub> NO <sub>3</sub>	$1.3 \times 10^{-7}$	$2.0 \times 10^{-11}$	0.28	$3.5 \times 10^{-7}$	$7.0 \times 10^{-18}$

### 3.3.6 Mass Spectrometry Analysis

Approximately 200  $\mu$ L of sample was mixed in a 1:1 ratio with acetonitrile to achieve stable electrospray ionization and then injected into the mass spectrometer using a direct infusion mode. An LTQ-Orbitrap mass spectrometer (Thermo Scientific<sup>TM</sup>) equipped with a modified ESI source was used to analyze the samples.<sup>56,57,59,140,149–152</sup> Mass spectra of the solvent (water and acetonitrile) were also collected so that background spectra could be subtracted from the sample spectra. All spectra were collected in the positive ion mode, and the resolving power of the instrument was  $\sim 10^5$  at  $m/z$  400.

The analysis of the mass spectra was carried out similarly to previous work.<sup>59,153</sup> Peak positions and intensities were first determined using Decon2LS program (<https://omics.pnl.gov/software/decontools-decon2ls>), and the resultant peak lists were clustered together according to experimental batch, such that 0, 1, 2, 3, and 4 h with photolysis was a group for each experimental condition and 0, 1, 2, 3, and 4 h without photolysis was another group. The clustered peaks were then assigned assuming a 0.001  $m/z$  accuracy with formulas of  $C_cH_hO_xN_nNa_s$ . The number of nitrogen atoms per molecule was allowed to be between 0 and 3. The number of sodium atoms was also allowed to be between 0 and 3. The monosodium adduct was the most common ion peak in nearly all cases, but some adducts corresponding to two sodium minus one hydrogen and even a few adducts corresponding to

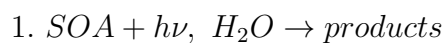
three sodium minus two hydrogens were observed. Sodium adducts are commonly observed in direct infusion electrospray ionization, and they can be formed during ionization within the instrument.<sup>154,155</sup> But since it is unusual to have adducts with more than one sodium ion, additional checks were performed to make sure that these peaks could not be explained by isotopes or possible impurities. It is assumed that the intentional addition of NaNO<sub>3</sub> in some of the experiments enhanced the sodium adduct formation.

Nitrogen was allowed in the assignments in all conditions. In the case of the pure water and H<sub>2</sub>O<sub>2</sub>-containing samples, nitrogen-containing assignments with formulas that may reasonably be expected from terpene oxidation (C<sub>7-10</sub>H<sub>14-16</sub>NO<sub>3+</sub> for APIN and C<sub>13-15</sub>H<sub>22-24</sub>NO<sub>3+</sub> for HUM) were not observed. In the case of the sodium and ammonium nitrate salt-containing samples, some reasonable nitrogen-containing formulas were assigned, although the abundances were very low and may reasonably be considered negligible. Elemental ratios for assigning were constrained to  $0 < O/C < 1.3$  and  $0.7 < H/C < 2.0$  to ensure the assignment of physically reasonable formulas.<sup>156</sup> <sup>13</sup>C isotopes and obvious impurities with anomalous mass defects were not considered for the remainder of the analysis. Assigned peaks were then used to check the internal calibration of the m/z axis. Peaks that were unassigned and peaks with questionable suggested formulas were re-assigned manually using a molecular formula calculator (<http://magnet.fsu.edu/~midas/>). In the case of the samples containing ammonium nitrate, it was possible for peaks to have been ionized by ammonium. Therefore, in these trials, peaks containing nitrogen were examined individually to determine whether this was the case. Since the majority of the peaks were ionized by sodium, only peaks with a large analogous sodium ion adduct peak and an unusually high H/C ratio (from the 4 extra H-atoms in NH<sub>4</sub><sup>+</sup>) were assumed to be ammonium ion adducts. Lastly, the formulas of the assigned ions were converted to the neutral formulas by removing Na<sup>+</sup>, H<sup>+</sup>, or NH<sub>4</sub><sup>+</sup>, depending on the ionization mechanism. Hereafter, all the identified compounds are presented and discussed as neutral species with their corresponding masses.

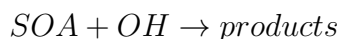
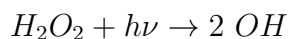
## 3.4 Results and Discussion

### 3.4.1 Effect of Aging on APIN SOA Mass Spectra

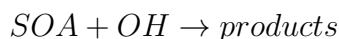
The presence of aqueous oxidants and salts in SOA extracts under irradiated and dark conditions can be expected to foster different chemical pathways for SOA aging. In experiments where only SOA is dissolved in pure water, photolysis and hydrolysis of SOA compounds can occur in parallel:



In the presence of hydrogen peroxide, there can be additional reactions between SOA and  $\text{H}_2\text{O}_2$  or reactions driven by oxidation of SOA compounds with OH:



Nitrate photolysis produces OH radicals and nitrating agents such as  $\text{NO}_2$  which may react with SOA to form nitrogen-containing organic compounds (NOC),<sup>61</sup> so nitrate ions can influence the products of photolytic SOA aging.



For solutions where ammonium salts are present, competing reactions between carbonyls and ammonia can occur, generating reduced NOC,<sup>25,157</sup> as well as various reactions catalyzed by ammonia.<sup>63,64</sup>

#### 4. $SOA \xrightarrow{NH_4^+} products$

Finally, the presence of inorganic ions changes the ionic strength of solutions, which can indirectly affect reactions such as hydrolysis. The OH concentrations present in the solutions in this work were very low, so OH and other radical reactions will be neglected during the analysis. Evidence of the other processes described above will be the focus of analysis of the mass spectra, as described below.

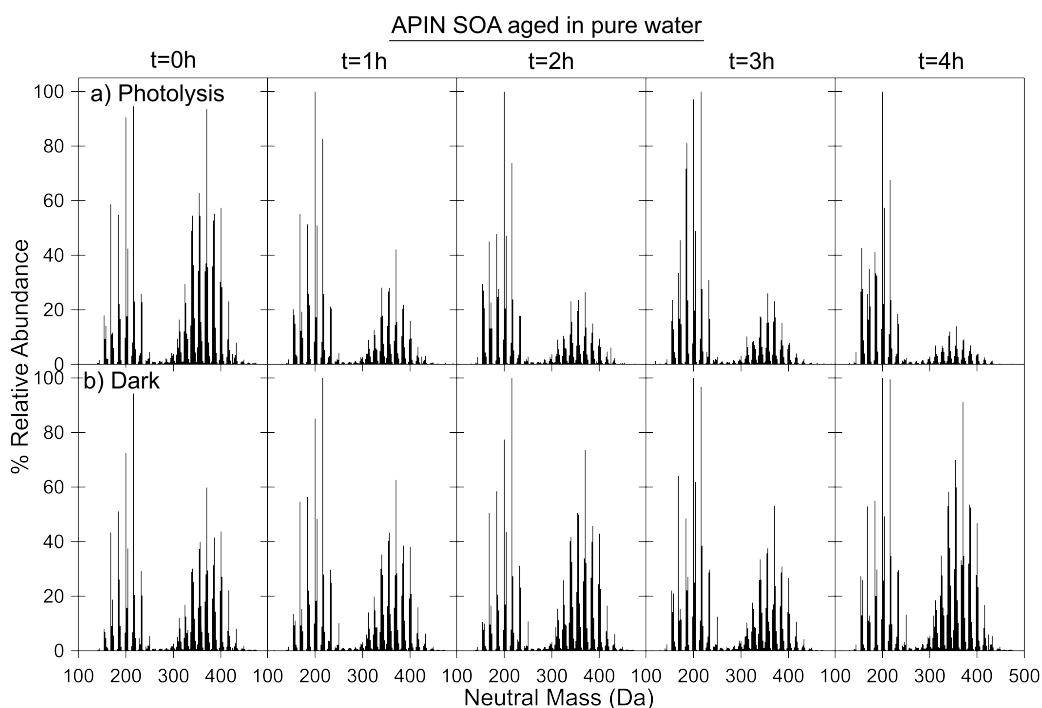
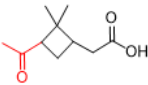
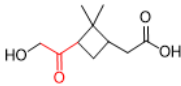
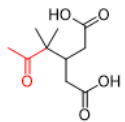
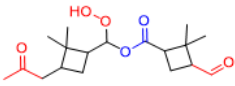
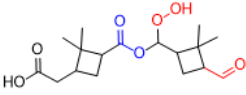
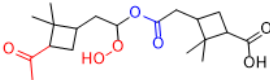


Figure 3.3: Mass spectra for the APIN SOA aged in nanopure water at 0, 1, 2, 3, and 4 h. Panel (a) shows aging with photolysis, and panel (b) shows dark aging.

Figure 3.3 shows the mass spectra of the APIN SOA solution in nanopure water over the 4 h aging period in both the photolysis and dark experiments. Peaks are normalized to the highest peak in each spectrum. The unaged mass spectra are similar to previously reported APIN SOA ozonolysis spectra,<sup>59,60,158–161</sup> for example, the monomer (<300 Da, a single oxygenated APIN unit) and dimer regions (300 – 500 Da, two covalently-bound oxygenated APIN units) can be clearly discerned.  $C_{10}H_{16}O_5$  (MW 216),  $C_{10}H_{16}O_4$  (10-hydroxypinonic

acid), and  $C_{10}H_{16}O_3$  (pinonic acid) appear as the most abundant monomers.  $C_{19}H_{30}O_7$  (MW 370) and  $C_{19}H_{30}O_8$  (MW 386), which were identified as ester compounds when observed in boreal forest field studies in Hyytiälä, Finland,<sup>162</sup> are the major detected dimers.<sup>163</sup> Some peaks of interest can be found in Table 3.5. Another feature of Figure 3.3 is a reduction in the relative abundance of dimers as compared to monomers with photolysis, but not in the dark condition, as observed previously in experiments in pure water.<sup>60</sup> This relationship may more easily be seen in Figure 3.4, which shows all dimer/monomer ratios for the systems discussed.

Table 3.5: Some of the major compounds detected in the APIN SOA by mass spectrometry. Photolyzable groups are shown in red, and hydrolyzable groups are shown in blue. Suggested structures were retrieved from previous work.<sup>162–167</sup>

Observed Molecular Weight (Da)	Relative Abundance (%)	Compound Formulas and Suggested Structures
184	51	Pinonic Acid – $C_{10}H_{16}O_3$ – Monomer 
200	72	10-hydroxypinonic acid – $C_{10}H_{16}O_4$ – Monomer 
216	100	$C_{10}H_{16}O_5$ – Monomer 
340	30	$C_{18}H_{28}O_6$ – Dimer 
356	40	$C_{18}H_{28}O_7$ – Dimer 
370	60	$C_{19}H_{30}O_7$ – Dimer 

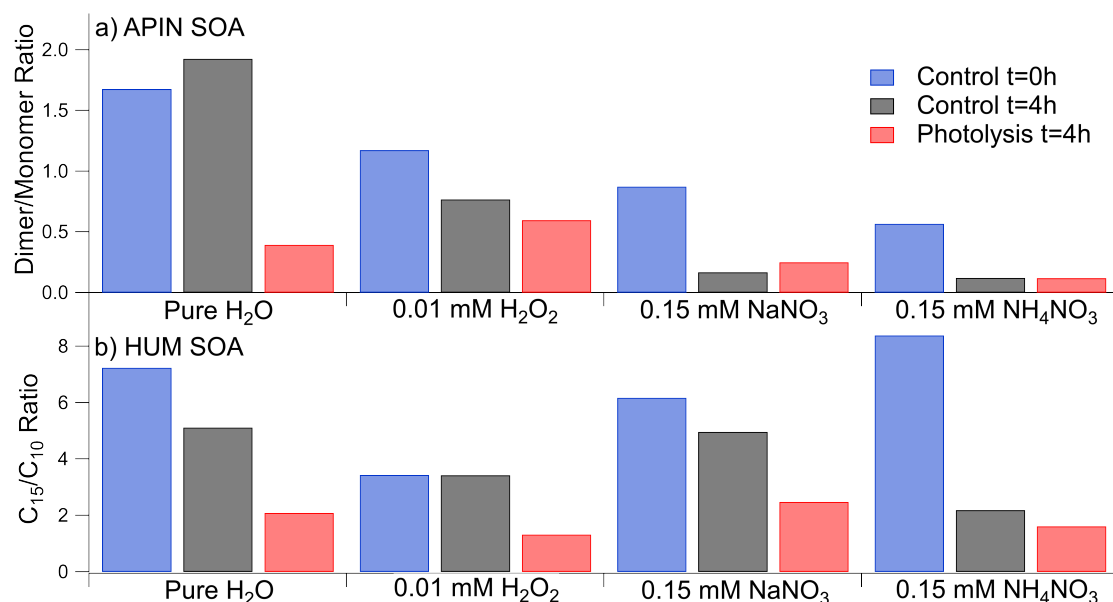


Figure 3.4: Dimer/monomer ratios and  $C_{15}/C_{10}$  ratios for APIN SOA (a) and HUM SOA (b), respectively, are shown for 0 h, the dark control at 4 h, and photolysis at 4 h. Data are grouped by aqueous aging conditions. Ratios are calculated by dividing the total dimer by the total monomer peak intensity or the total  $C_{15}$  by the total  $C_{10}$  peak intensity. These ratios are analogous in the sense that monomer and  $C_{10}$  peaks both represent lower molecular weight aging products in the performed experiments. Further explanation of  $C_{10}$  and  $C_{15}$  peaks is provided in the section discussing the effect of aging on HUM SOA mass spectra.

Figure 3.5 shows the HRMS spectra acquired from the APIN SOA + H<sub>2</sub>O<sub>2</sub> experiment. The spectra are qualitatively similar to those of APIN SOA in pure water (Figure 3.3). Again, there is a greater decrease in the dimer region of the spectra in the presence of H<sub>2</sub>O<sub>2</sub> than in the dark, as shown in Figure 3.4. However, the relative abundance of dimers is actually larger in Figure 3.5 (after irradiation of SOA with H<sub>2</sub>O<sub>2</sub>) than in Figure 3.3 with photolysis (after irradiation of SOA in pure water). This may be a result of the formation of peroxyacetals from reactions of H<sub>2</sub>O<sub>2</sub> and carbonyls present in the SOA.<sup>137</sup> This would decrease the rate of decay as the lifetimes of carbonyls<sup>72</sup> have been estimated to be shorter than the lifetimes of peroxides<sup>43</sup> at wavelengths above 300 nm, as are present in this study.

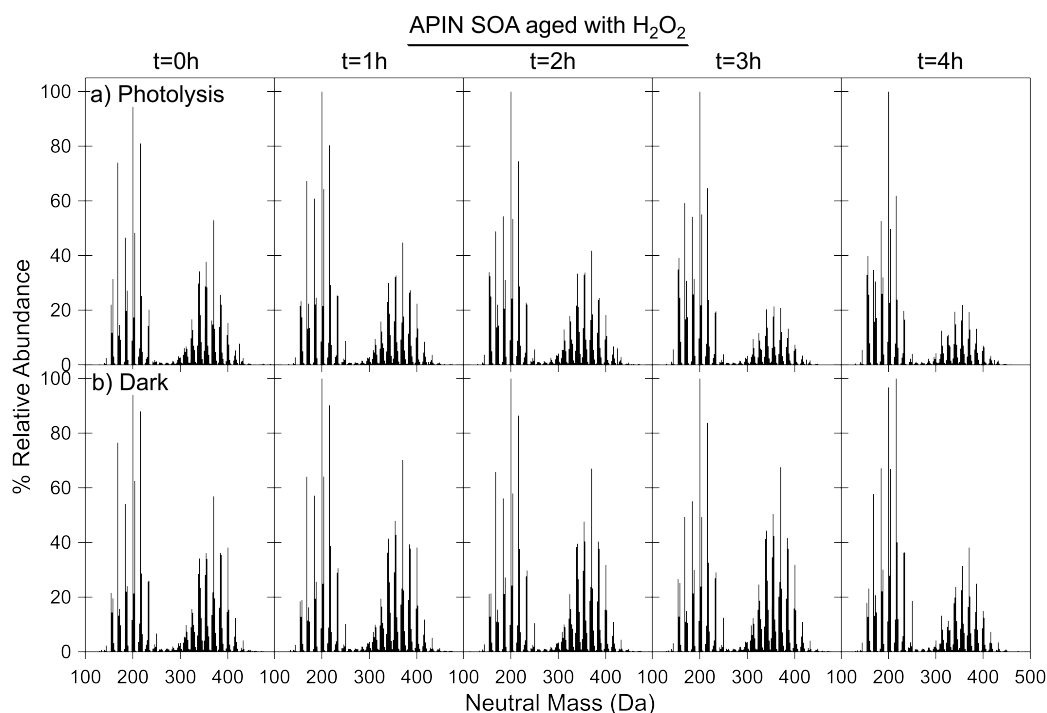


Figure 3.5: Mass spectra for the APIN SOA aged with 0.01 mM H<sub>2</sub>O<sub>2</sub>. Panel (a) shows aging with photolysis and panel (b) shows dark aging.

The most interesting feature of Figure 3.6 is the effect of nitrate salts on APIN SOA aging in the dark. Under these conditions, a large reduction in the relative abundance of dimers was observed. This is a significant departure from the minor effect of dark reactions in the pure water and H<sub>2</sub>O<sub>2</sub> conditions (also illustrated in Figure 3.4). The reduction in dimers in both



the photolysis and control conditions was much more significant in the presence of nitrates than in the other conditions. One possible explanation for the observed dark chemistry is that nucleophilic compounds, particularly oxyanions, have been shown to catalyze the hydrolysis of esters,<sup>168</sup> which are prevalent among dimers in APIN SOA. The final mass spectra of the photolysis and dark reactions with nitrate were compared in hope of finding unique peaks attributable to hydrolysis, but no systematic difference between peaks in irradiated and non-irradiated solutions was observed. The hydrolysis reaction converts dimers to monomers, which are also present in solution to begin with, making it hard to identify a signature of hydrolysis chemistry.

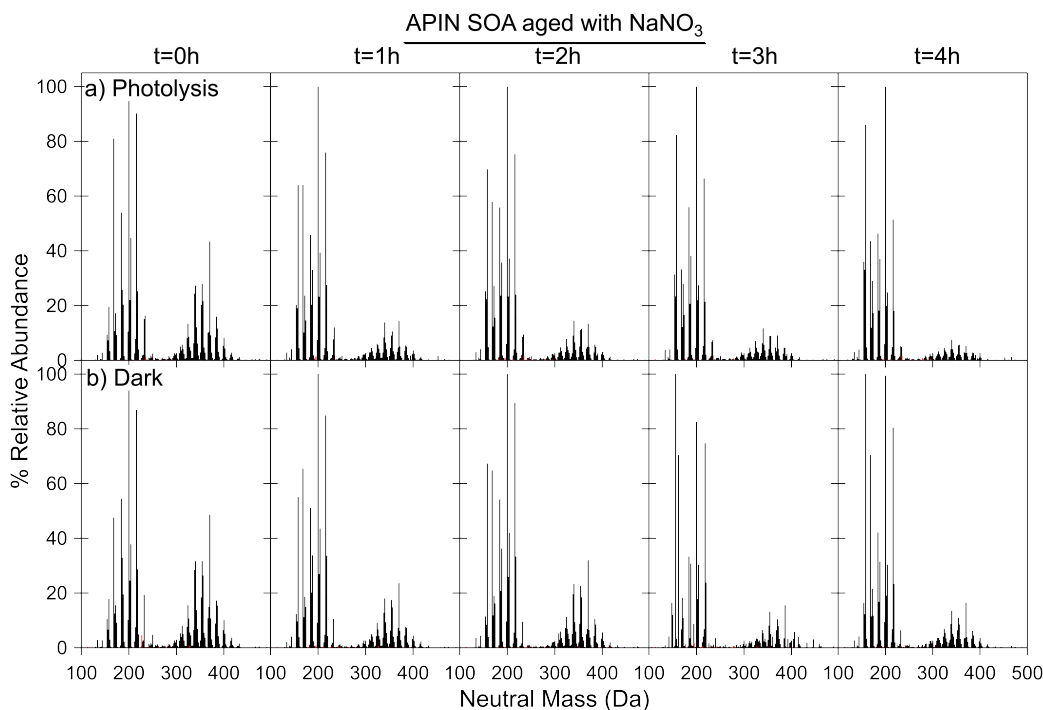


Figure 3.6: Mass spectra for the APIN SOA aged with 0.15 mM  $\text{NaNO}_3$ . Panel (a) shows aging with photolysis and panel (b) shows dark aging.

In the APIN +  $\text{NH}_4\text{NO}_3$  experiment shown in Figure 3.7 is that the dimer region in the  $t=0$  panels is already smaller than in the other experiments, even as compared to the analogous APIN +  $\text{NaNO}_3$  experiment (Figure 3.6). This implies that there was a significant reduction in dimers already in the short time between the ammonium nitrate being added and the

sample being analyzed by HRMS (about 10 minutes). Some of the reduction in the dimer peak abundances may also be due to ionization suppression effects known to be caused by the presence of salts in electrospray,<sup>169</sup> but the apparently time-dependent further reduction in the dimer peaks following hydrolysis and photolysis suggests that the ionization suppression effects cannot be solely responsible for these observations.

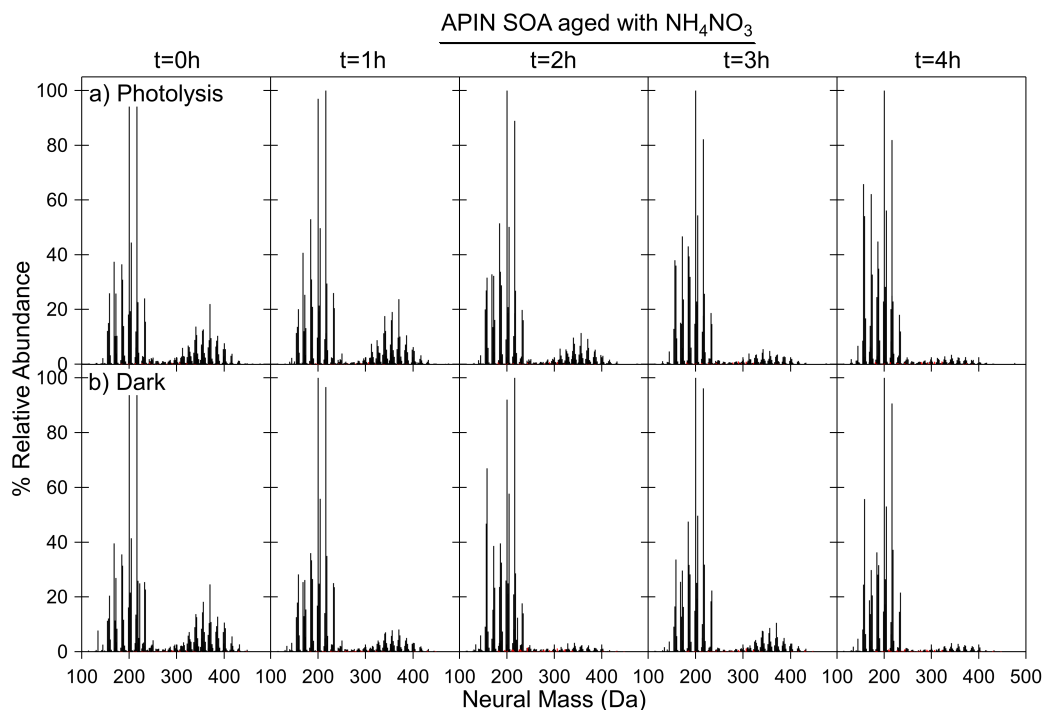


Figure 3.7: Mass spectra for the APIN SOA aged with 0.15 mM  $\text{NH}_4\text{NO}_3$ . Panel (a) shows aging with photolysis and panel (b) shows dark aging.

### 3.4.2 Effect of Aging on HUM SOA Mass Spectra

Mass spectra of HUM SOA in nanopure water are shown in Figure 3.8. The majority of the peaks are clustered around the  $\text{C}_{15}$  region that makes up the HUM carbon backbone. The largest peaks in the spectra are shown in Table 3.6 and have formulas  $\text{C}_{15}\text{H}_{24}\text{O}_x$  where  $x$  ranges from 4 to 8, with the most abundant compound in each spectrum being  $\text{C}_{15}\text{H}_{24}\text{O}_7$ . For the HUM SOA, the first-generation ozonolysis products of HUM have vapor pressures sufficiently low to form particles, and dimers are low in abundance.<sup>170</sup> There are a few

compounds in the  $C_{10}$  region (clustered around a mass of 200 Da) which have been reported in previous studies,<sup>60,134</sup> and seem to be common products of the fragmentation of HUM. The abundances of  $C_{10}$  peaks increase relative to those of  $C_{15}$  peaks with photolysis, but there is no significant change in the overall  $C_{15}/C_{10}$  peak ratio under dark conditions in water.

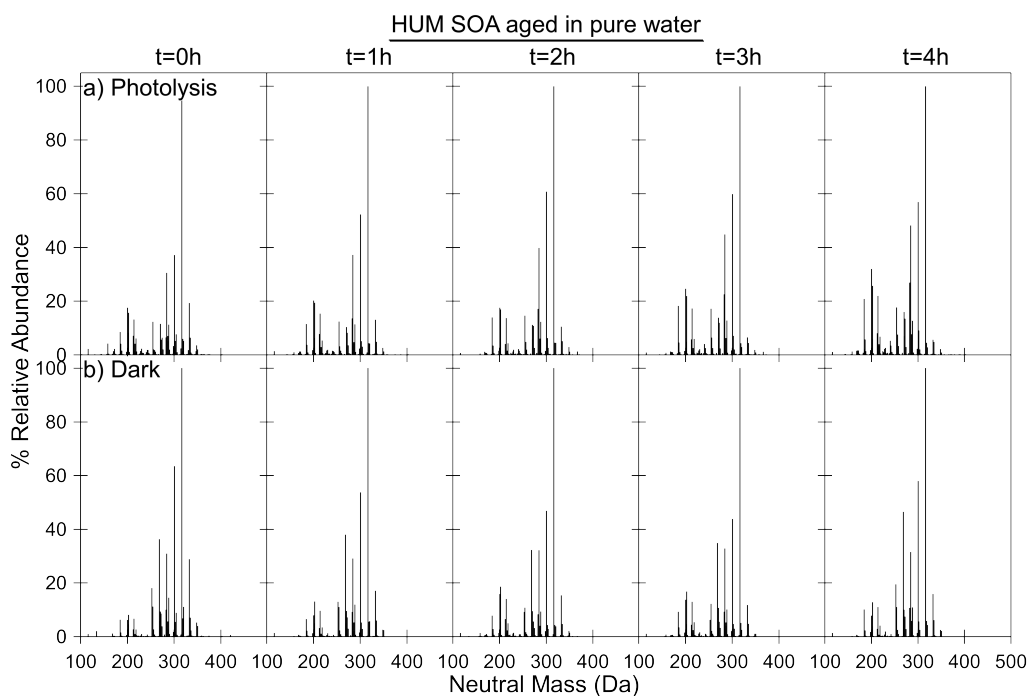


Figure 3.8: Mass spectra for the HUM SOA aged in nanopure water. Panel (a) shows aging with photolysis and panel (b) shows dark aging.

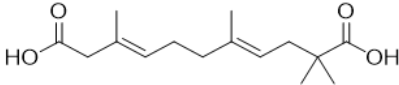
Observed Molecular Weight (Da)	Relative Abundance (%)	Compound Formula
268	36	C <sub>15</sub> H <sub>24</sub> O <sub>4</sub> 
284	31	C <sub>15</sub> H <sub>24</sub> O <sub>5</sub>
300	63	C <sub>15</sub> H <sub>24</sub> O <sub>6</sub>
316	100	C <sub>15</sub> H <sub>24</sub> O <sub>7</sub>
332	29	C <sub>15</sub> H <sub>24</sub> O <sub>8</sub>

Table 3.6: The major compounds detected in the HUM SOA before aging. The only previously identified HUM SOA compound structure is included.<sup>134</sup>

The effects of H<sub>2</sub>O<sub>2</sub> and inorganics were less prominent for HUM SOA than for APIN SOA. Figure 3.9 shows that HUM SOA experiences carbon chain shortening from photolysis with H<sub>2</sub>O<sub>2</sub>, as higher relative abundances of C<sub>10</sub> compounds were observed after four hours of photolysis with H<sub>2</sub>O<sub>2</sub>. This is qualitatively similar to the results for APIN SOA. Comparing the pure water experiment (Figure 3.8) with the HUM SOA + NaNO<sub>3</sub> experiment (Figure 3.10), the presence of NO<sub>3</sub><sup>-</sup> had little effect on the aging of the HUM SOA. This suggests that esters, which are present in APIN SOA and may be hydrolyzed with nitrate, are not as abundant in HUM SOA. There is a more dramatic decrease in the C<sub>15</sub>/C<sub>10</sub> ratio in the HUM SOA + NH<sub>4</sub>NO<sub>3</sub> condition (Figure 3.11) but the final mass spectrum after four hours is not too different from the mass spectra observed under other conditions.

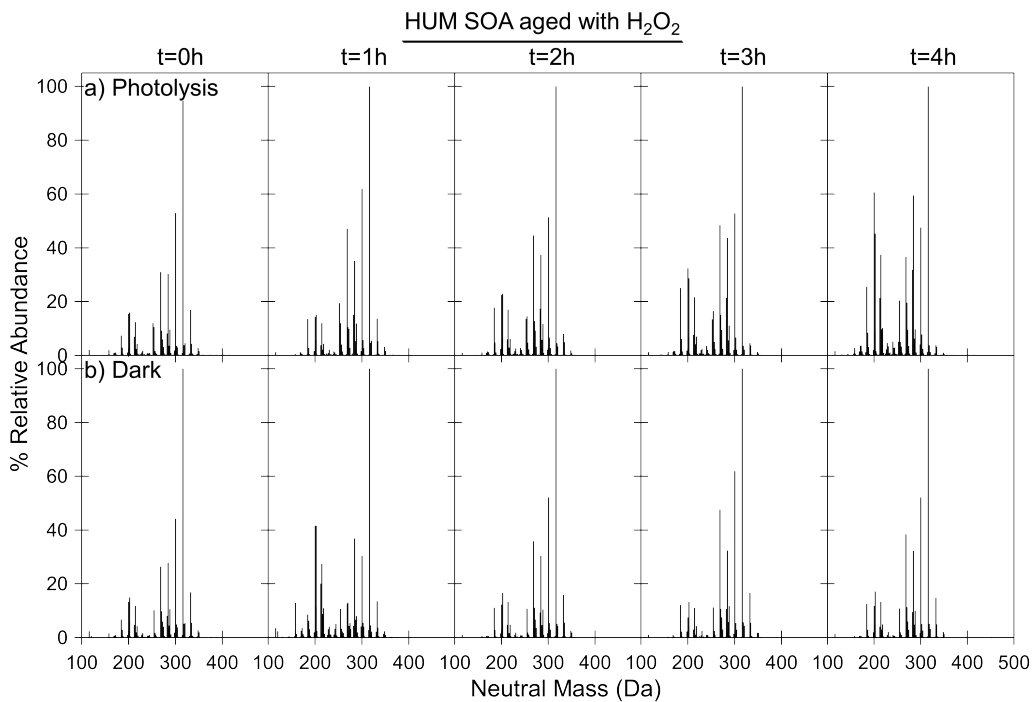


Figure 3.9: Mass spectra for the HUM SOA aged with 0.01 mM  $\text{H}_2\text{O}_2$ . Panel (a) shows aging with photolysis and panel (b) shows dark aging.

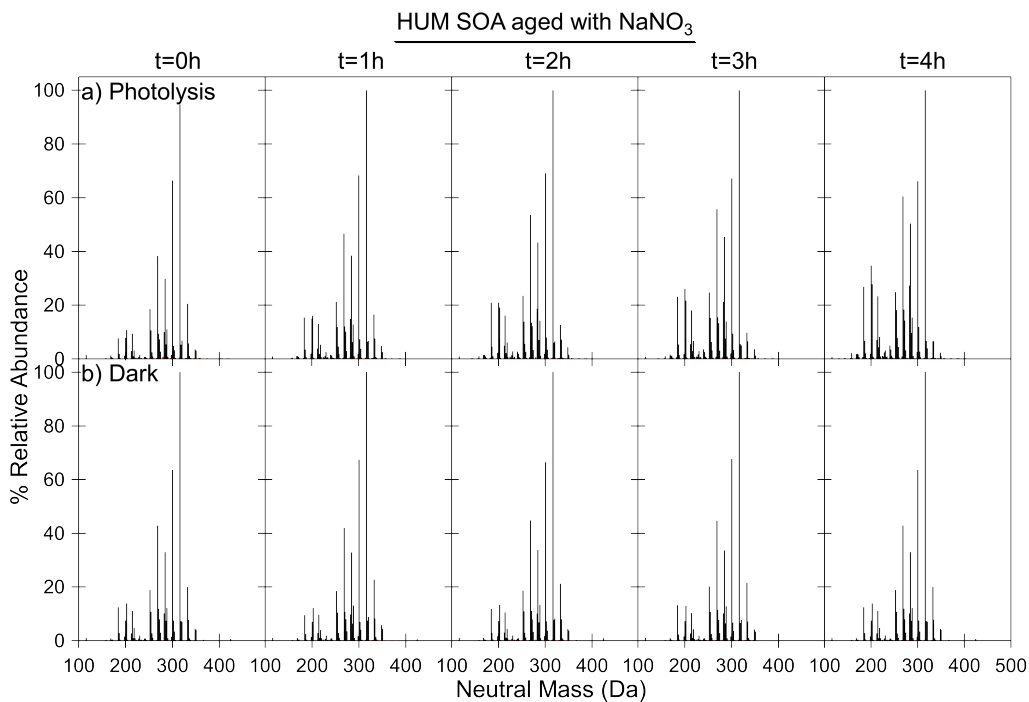


Figure 3.10: Mass spectra for the HUM SOA aged with 0.15 mM  $\text{NaNO}_3$ . Panel (a) shows aging with photolysis and panel (b) shows dark aging.

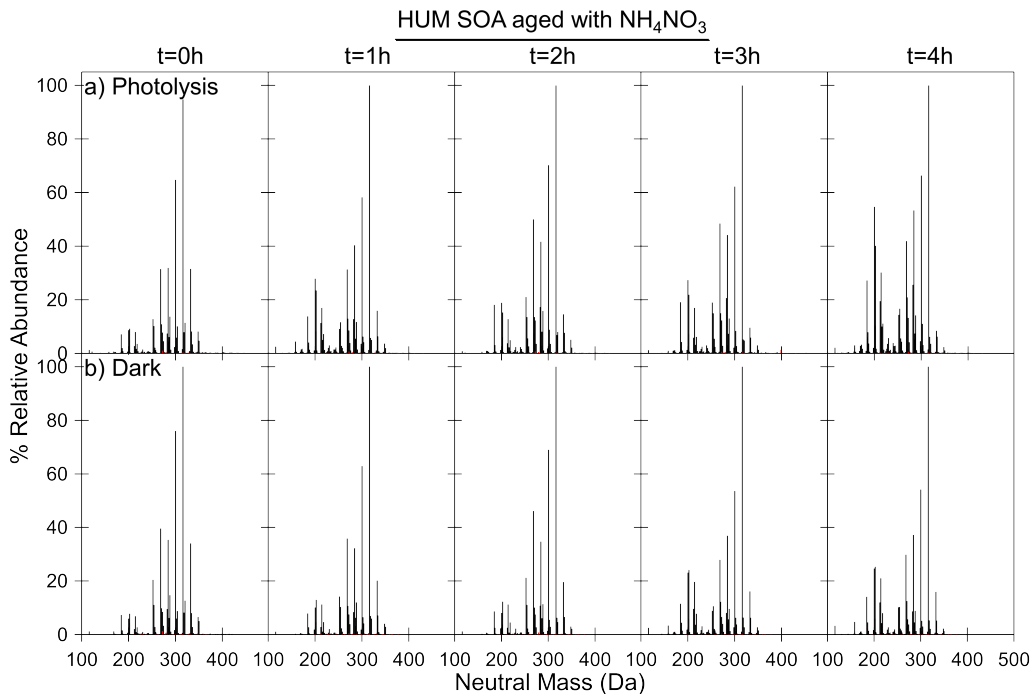


Figure 3.11: Mass spectra for the HUM SOA aged with 0.15 mM  $\text{NH}_4\text{NO}_3$ . Panel (a) shows aging with photolysis and panel (b) shows dark aging.

### 3.4.3 Effect of Aging on Elemental Ratios

O/C, H/C, and N/C values are reported in Figures 3.12 (APIN SOA) and 3.13 (HUM SOA) as a function of reaction time. The average carbon number is also reported in these figures to illustrate the average molecular size at each time point. These average values were calculated from the neutral molecular formulas using Equation 3.3, where  $I_i$  are the peak abundances:

$$\langle x \rangle = \frac{\sum I_i x_i}{\sum I_i} \quad (x = \#C, H/C, O/C, H/C) \quad (3.3)$$

As elemental ratios are of great interest to the AMS community, the O/C and H/C ratios calculated from ESI-MS were compared to those measured by the AMS when making the HUM SOA. Generally, O/C ratios calculated from ESI-MS are expected to be similar to those calculated by the AMS and have comparable accuracy.<sup>152</sup> In this study the O/C and

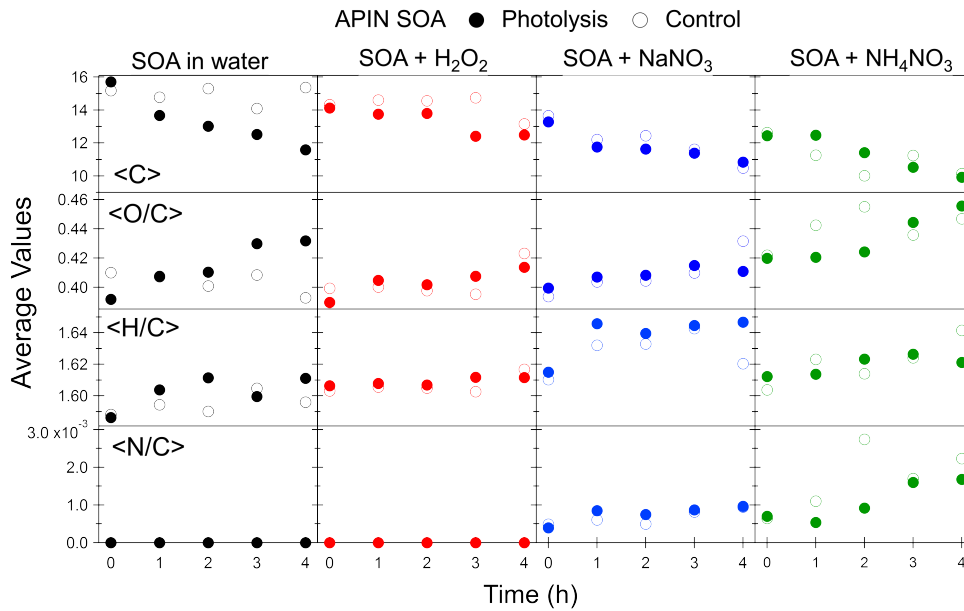


Figure 3.12: Average values for the number of carbon atoms, O/C ratios, H/C ratios, and N/C ratios are shown at each hour of the four-hour aging time of APIN SOA in nanopure water, 0.01 mM  $\text{H}_2\text{O}_2$ , 0.15 mM  $\text{NaNO}_3$ , and 0.15 mM  $\text{NH}_4\text{NO}_3$ . Open circles denote the dark control condition, and closed circles denote the photolysis condition.

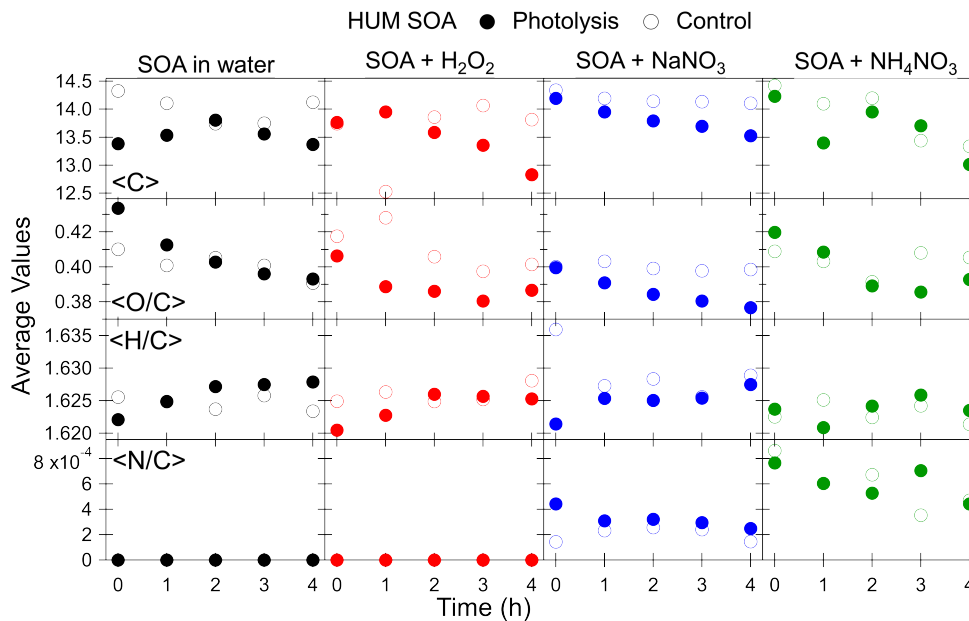


Figure 3.13: Average values for the number of carbon atoms, O/C ratios, H/C ratios, and N/C ratios are shown at each hour of the four-hour aging time of HUM SOA in nanopure water, 0.01 mM  $\text{H}_2\text{O}_2$ , 0.15 mM  $\text{NaNO}_3$ , and 0.15 mM  $\text{NH}_4\text{NO}_3$ . Open circles denote the dark control condition, and closed circles denote the photolysis condition.

H/C values were similar between the two instruments, though not exactly the same. The O/C ratio was about 0.40 when determined by ESI-MS and 0.37 when determined by AMS. The H/C ratios were 1.63 and 1.80 by ESI-MS and AMS, respectively. Some discrepancy should be expected as the ESI-MS and AMS analyses were performed on different chamber experiments.

Figures 3.12 and 3.13 show that APIN SOA and HUM SOA contain molecules of similar average carbon number ( $\sim C_{15}$ ). This is due to the comparable abundance of monomers ( $C_{10}$ ) and dimers ( $C_{20}$ ) in the APIN SOA mass spectra and the predominance of monomers ( $C_{15}$ ) in the HUM SOA mass spectra. The average carbon number decreased under all irradiated conditions indicating that APIN SOA dimers are degraded and HUM SOA  $C_{15}$  compounds are converted to  $C_{10}$  compounds with photolysis. Most of the samples aged in the dark did not exhibit a significant decrease in carbon number with reaction time. Two exceptions are the APIN SOA control experiments containing nitrate salts and the HUM SOA experiment containing ammonium. In these experiments, the photolysis and control samples had similar decreases in average carbon number over the four hours, which agrees with the shift toward lower molecular weights shown in these mass spectra in Figures 3.6, 3.7, and 3.11.

Average O/C ratios reflect the extent of SOA oxidation, which is indirectly related to the volatility of the SOA compounds. Within the uncertainty for the calculated O/C ratios, they do not change much with time, although subtle trends can be discerned. Previous studies of APIN SOA reactions in pure water have shown average O/C ratios to increase slowly with photolysis and decrease with hydrolysis,<sup>171,172</sup> and the same trends are observed here (Figure 3.12). In contrast, in presence of an aqueous oxidant, the average O/C ratio appears to increase for both the photolysis and control conditions. A decrease in O/C ratios was observed for HUM SOA photolysis and hydrolysis conditions in pure water (Figure 3.13),



confirming the results of previous work.<sup>60</sup> The same trend was observed in the presence of  $\text{H}_2\text{O}_2$ . However, in presence  $\text{NaNO}_3$  and  $\text{NH}_4\text{NO}_3$ , the average O/C ratio for the control conditions was approximately constant over time. These subtle differences in the behavior of aqueous SOA in the presence of aqueous oxidants versus in pure water show that SOA aging in pure water does not fully represent the chemistry occurring in ambient cloud droplets. Finally, the average N/C ratios were also calculated to check for the evidence of  $\text{NH}_4^+$  or  $\text{NO}_3^-$  driven chemistry leading to stable organonitrogen compounds. As pointed out above, the peak abundances of NOC were small, typically below 2% of the highest peak, and not visible in Figures 3.6, 3.7, 3.10 and 3.11.

### 3.5 Conclusions

Chemistry occurring in cloud and fog water is known to be an important aspect of SOA formation and aging. These atmospheric waters contain small concentrations of oxidants and inorganic salts, which may have various direct and indirect effects on aqueous reactions of SOA compounds. This study analyzed the effect of atmospheric oxidants ( $\text{H}_2\text{O}_2$ ) and inorganic salts ( $\text{NaNO}_3$  and  $\text{NH}_4\text{NO}_3$ ) on the aging of aqueous SOA in the dark and under UV irradiation conditions. The initial expectation was that the added solutes would not do much under dark conditions but would strongly accelerate the photodegradation of dissolved SOA. However, the presence of nitrate ions efficiently reduced dimer abundance in APIN SOA without photolysis, possibly through catalysis of hydrolysis of dimeric esters. The unusual effect of nitrate ions will be particularly important in urban areas where large amounts of  $\text{NO}_x$  from cars lead to significant amounts of  $\text{NO}_3^-$  in the atmospheric waters (for example, in the Los Angeles area). These results show that it is important to consider the presence of inorganic salts in cloud or fog water when studying aqueous SOA aging, both in the dark and under irradiated conditions.

## Chapter 4

# Effects of the sample matrix on the photobleaching and photodegradation of toluene-derived secondary organic aerosol compounds

Portions of this chapter were reproduced under the Creative Commons Attribution 4.0 License from: Klodt, A.; Adamek, M.; Dibley, M.; Nizkorodov, S.; O'Brien, R., Effects of the sample matrix on the photobleaching and photodegradation of toluene-derived secondary organic aerosol compounds, *Atmospheric Chemistry and Physics*, **2022**, *22*, 10155-10171, <https://doi.org/10.5194/acp-22-10155-2022>.

## 4.1 Abstract

Secondary organic aerosol (SOA) generated from the photooxidation of aromatic compounds in the presence of oxides of nitrogen ( $\text{NO}_x$ ) is known to efficiently absorb ultraviolet and visible radiation. With exposure to sunlight, the photodegradation of chromophoric compounds in the SOA causes this type of SOA to slowly photobleach. These photodegradation reactions may occur in cloud droplets, which are characterized by low concentrations of solutes, or in aerosol particles, which can have highly viscous organic phases and aqueous phases with high concentrations of inorganic salts. To investigate the effects of the surrounding matrix on the rates and mechanisms of photodegradation of SOA compounds, SOA was prepared in a smog chamber by photooxidation of toluene in the presence of  $\text{NO}_x$ . The collected SOA was photolyzed for up to 24 h using near-UV radiation (300-400 nm) from a Xenon arc lamp under different conditions: directly on the filter, dissolved in pure water, and dissolved in 1 M ammonium sulfate. The SOA mass absorption coefficient was measured as a function of irradiation time to determine photobleaching rates. Electrospray-ionization high-resolution mass spectrometry coupled to liquid chromatography separation was used to observe changes in SOA composition resulting from the irradiation. The rate of decrease in SOA mass absorption coefficient due to photobleaching was the fastest in water, with the presence of 1 M ammonium sulfate modestly slowing down the photobleaching. By contrast, photobleaching directly on the filter was much slower. The high-resolution mass spectrometry analysis revealed an efficient photodegradation of nitrophenol compounds on the filter but not in the aqueous phases, with relatively little change observed in the composition of the SOA irradiated in water or 1 M ammonium sulfate despite faster photobleaching than in the on-filter samples. This suggests that the photodegradation of nitrophenols contributes much more significantly to photobleaching in the organic phase than in the aqueous phase. We conclude that the SOA absorption coefficient lifetime with respect to photobleaching and

lifetimes of individual chromophores in SOA with respect to photodegradation will depend strongly on the sample matrix in which SOA compounds are exposed to sunlight.

## 4.2 Introduction

Brown carbon (BrC) aerosol has important impacts on the Earth’s radiative forcing.<sup>173</sup> Because it absorbs actinic radiation in the near-UV (300 to 400 nm) and visible spectral ranges, BrC aerosol reduces the scattering of solar radiation and cooling effect relative to non-absorbing aerosols.<sup>25</sup> BrC aerosol can be produced from biomass burning or various gas-phase or multiphase reactions in the atmosphere.<sup>25</sup> The photooxidation of aromatic compounds in the presence of nitrogen oxides (NO<sub>x</sub>) is a known anthropogenic source of BrC.<sup>58,70,174</sup> For example, secondary organic aerosol (SOA) formed from toluene is brown in appearance because it contains nitrophenols and other chromophoric species.<sup>175,176</sup>

After its formation, the composition and optical properties of BrC continue to slowly change, driven in part by direct and indirect photolysis processes (collectively referred to as “photodegradation” in this paper).<sup>40</sup> Studies of BrC aging by exposure to actinic radiation have largely focused on photodegradation processes occurring in cloud-water,<sup>40</sup> although aerosol particles are estimated to spend about 85% of their lifecycle under non-cloud conditions, i.e. RH <100%.<sup>47</sup> Less work has been done on photodegradation of BrC in submicron particles, which can include pockets of concentrated aqueous solutions as well as solid organic and inorganic phases with a limited amount of water in them. Water in deliquesced aerosol particles differs from cloud water in several ways, especially in terms of the concentrations of inorganic ions. While the dominant inorganic species in both deliquesced aerosol particles and cloud water are generally ammonium and sulfate,<sup>50</sup> aqueous particles have ionic strengths of greater than 1 M as compared to 10<sup>-5</sup> to 10<sup>-2</sup> M in cloud water.<sup>49</sup> Photochemical

processes occurring in the water present in deliquesced aerosol particles may potentially be altered by high concentrations of inorganic species.

Previous work has found complex effects of ionic strength on aqueous photochemistry in solutions meant to mimic deliquesced aerosol particles. These studies have largely looked at changes in the UV and visible absorption spectrum and photodegradation rate of single molecules in the presence of inert salts. For instance, the absorption spectrum of pyruvic acid experiences a bathochromic shift of the major absorption band along with the hyperchromic effect at increased ionic strength at lower ( $<4$ ) pH values.<sup>65,67</sup> However, the photodegradation rate has been shown to increase when the ionic strength was increased with  $\text{NaClO}_4$ ,<sup>65</sup> but decrease when the ionic strength was adjusted with  $\text{NaCl}$  and  $\text{CaCl}_2$ .<sup>67</sup> When similar experiments were conducted for lignin-derived compounds, increasing the ionic strength lead to the formation of a new major absorption band at longer, more atmospherically relevant, wavelengths.<sup>66,69</sup> Similar to pyruvic acid, photodegradation kinetics were observed to accelerate for acetosyringone in the presence of  $\text{NaClO}_4$ ,<sup>66</sup> but decelerate for vanillin in the presence of  $\text{NaNO}_3$  and  $\text{Na}_2\text{SO}_4$ .<sup>69</sup> To the best of our knowledge, only one study has considered the impact of varying ionic strength on the rate of photochemical reactions of complex mixtures of organics representative of aerosol particles. Ray et al.<sup>68</sup> irradiated solutions of rice-straw smoldering primary organic aerosol in the presence of  $\text{NaCl}$ ,  $\text{NaNO}_3$ , and  $\text{Na}_2\text{SO}_4$  to explore anionic effects and ionic strength effects on photo-bleaching kinetics. They found longer lifetimes of absorbing species in the presence of all ionic species studied. From these studies, it seems that the specific ionic species present during photolysis may be important; however, no photodegradation studies have been conducted in the presence of ammonium sulfate at high ionic strengths although ammonium and sulfate are the dominant contributors to ionic strength in deliquesced aerosol particles.<sup>50</sup>

Direct and indirect photolysis have been identified as potentially important sinks for SOA

compounds in the condensed-phase environment found in dry organic particles,<sup>70</sup> but there have only been a few studies of these processes. This environment is uniquely different from aqueous solutions in that SOA molecules are in a highly viscous organic matrix, and different photochemical mechanisms operate compared to those acting in water. Early indications that dry SOA is easily degraded by near-UV radiation – both UV-A and UV-B – came from examining the production of volatile products of SOA irradiated directly on its collection substrate.<sup>71–73</sup> Subsequent studies suggested that direct photolysis is an important sink for atmospheric SOA, but focused primarily on low-NO<sub>x</sub> terpene ozonolysis SOA and found that peroxide and carbonyl compounds were driving the photochemistry.<sup>41–46,74</sup> As a counter-example, Kourtchev et al.<sup>177</sup> found limited changes in the molecular composition of SOA by photolysis compared to heterogeneous oxidation by hydroxyl (OH) radicals for SOA suspended in an environmental simulation chamber, but it should be recognized that separating gas-phase and condensed-phase photochemistry in chamber experiments is challenging. Romonosky et al.<sup>70</sup> measured the absorption coefficients of a number of SOA types and estimated their photodegradation lifetimes, concluding that strongly light-absorbing SOA were predicted to have the shortest lifetimes. Subsequent experiments found that a stronger absorption coefficient does not necessarily translate to faster photodegradation, with SOA from aromatic precursors being more photostable than SOA from terpenes, even though the latter barely absorb near-UV radiation.<sup>75–77</sup> While these studies all gave insight into the mechanism of SOA photodegradation during UV-irradiation, none of them directly measured photobleaching rates in the organic phase.

This study was prompted by a hypothesis that the mechanism of SOA photodegradation in particles dominated by organic material (e.g., dry SOA with low inorganic content) should be different from that dominated by liquid water (e.g., cloud droplets containing dissolved SOA). This hypothesis was tested by UV-irradiation of toluene high-NO<sub>x</sub> SOA directly on filters and in aqueous solution and then contrasting the reaction products and absorption

spectra. Our second goal was to explore the importance of inorganic salts in photobleaching and photodegradation of aqueous SOA, and this was done by UV-irradiation of high-NO<sub>x</sub> toluene SOA in a concentrated ammonium sulfate solution and pure water. We present high-resolution mass spectrometry, offline-AMS, and FTIR results to provide an analysis of changes in chemical composition during photodegradation in different conditions, as well as UV-Visible spectroscopy results to monitor decay of the overall absorbance by SOA. We find that the compositional changes differ significantly between the organic particle and aqueous photodegradation. The presence of 1 M aqueous ammonium sulfate does not appear to significantly impact the changes in SOA composition, but the photobleaching kinetics are modestly slowed as compared to the experiment in pure water.

### 4.3 Methods

Experiments were performed at the University of California Irvine (UCI) and at the College of William and Mary (WM). A summary of the types of experiments performed and the datasets collected is provided in Table 4.1. Briefly, all SOA filter samples were prepared in the UCI smog chamber. Some filter samples were mailed to WM on dry ice for on-filter photodegradation experiments and FTIR analysis. All aqueous phase photodegradation experiments, photobleaching kinetics measurements, and aerosol mass spectrometry experiments were carried out at UCI.

Table 4.1: Summary of the experiments carried out as part of this study at the College of William and Mary (WM) and the University of California Irvine (UCI).

Experiment Description	Data sets collected	Location
SOA preparation ( $\times 14$ )	Online-AMS	UCI
Trial experiments on aging of SOA in the aqueous phase ( $\times 5$ )	UV-Vis, LC-ESI-MS	UCI
Trial experiments on aging of SOA on filters ( $\times 2$ )	UV-Vis, Direct infusion ESI-MS, FTIR	WM
Aging of SOA in water and in 1 M ammonium sulfate ( $\times 3$ )	UV-Vis, LC-ESI-MS	UCI
Aging of SOA on-filter and/or in water ( $\times 4$ )	UV-Vis, LC-ESI-MS, offline-AMS	UCI

### 4.3.1 Secondary Organic Aerosol Generation

SOA was prepared in a  $\sim 5 \text{ m}^3$  Teflon chamber. The chamber was first humidified to 40% RH. Then  $\text{H}_2\text{O}_2$  was injected through a heated inlet to achieve a mixing ratio of 2 ppm, followed by an injection of 1.5 ppm of toluene and 0.7 ppm of NO. UV-B lamps within the chamber with an emission spectrum centered at 310 nm were used to initiate photooxidation, with typical OH steady-state concentrations of about  $6 \times 10^6 \text{ molecule cm}^{-3}$ , similar to our previous work.<sup>178</sup> OH steady-state concentrations in the chamber were determined from the rate of toluene depletion using a Proton Transfer Time of Flight Mass Spectrometer (PTR-ToF-MS; Ionicon model 8000, Innsbruck, Austria) as described below (section 4.3.1.1). For the PTR-ToF-MS analysis, the drift tube operated at 60.0 °C ( $T_{\text{drift}}$ ), 2.30 mbar ( $P_{\text{drift}}$ ), and 600 V ( $U_{\text{drift}}$ ). Mass calibration for the PTR-ToF-MS was performed using three ions commonly observed in room air:  $m/z$  21.0226 ( $\text{H}_3^{18}\text{O}^+$ ), 29.9980 ( $\text{NO}^+$ ), and 59.0497 ( $\text{C}_3\text{H}_6\text{O}^+$ ). No seed particles were used in the chamber experiments. A Scanning Mobility Particle Sizer (TSI Model 3936),  $\text{NO}_y$  monitor (Thermo Scientific Model 42i-Y), and ozone monitor (Thermo Scientific Model 49i) were used during all experiments to track particle size distribution and NO,  $\text{NO}_y$ , and ozone mixing ratios. An Aerosol Mass Spectrometer (AMS) was also used in some experiments to observe composition during aerosol generation and collection. Particles were collected onto polytetrafluoroethylene (PTFE) filters (Millipore 0.2  $\mu\text{M}$  pore



size), then the filters were sealed and frozen at -20 °C until the aging experiments were performed. Data related to the chamber experiments, including SMPS, NO<sub>y</sub>, and online-AMS datasets are available online at the Index of Chamber Atmospheric Research in the United States (ICARUS).<sup>179</sup> Table 4.2 provides a summary of the finalized set of samples used in this work (it does not include additional samples prepared for preliminary tests to optimize the experimental conditions).

Table 4.2: Summary of samples prepared and the experiments they were used for at William and Mary (WM) and University of California Irvine (UCI).

Filter Number (Location of experiments)	Max SOA concentration in the chamber ( $\mu\text{g m}^{-3}$ )	Total SOA collected (mg)	Data sets collected <sup>a</sup>
1 (WM)	308	0.9	Online-AMS, FTIR
2 (WM)	328	1.1	Online-AMS, FTIR
3 (UCI)	225	1.0	H <sub>2</sub> O & Filter Offline-AMS, ESI(+,-)
4 (UCI)	159	0.6	AS & H <sub>2</sub> O kinetics, <sup>b</sup> ESI(+,-)
5 (UCI)	178	0.8	AS H <sub>2</sub> O kinetics <sup>b</sup>
6 (UCI)	208	0.8	AS H <sub>2</sub> O kinetics <sup>b</sup>
7 (UCI)	126	0.8	Filter kinetics <sup>b</sup>
8 (UCI)	196	0.6	Filter kinetics <sup>b</sup>
9 (UCI)	156	0.7	Filter kinetics <sup>b</sup>

<sup>a</sup>2 filters for FTIR experiments, 1 filter for splitting between aqueous and filter aging, 3 filters for splitting between aqueous and ammonium sulfate aging kinetics, and 3 filters for only filter aging kinetics.

<sup>b</sup>AS & H<sub>2</sub>O kinetics refers to kinetic experiments in 1 M ammonium sulfate and pure water solutions, while filter kinetics refers to kinetic experiments on the filter.

#### 4.3.1.1 Chamber OH Steady-State Estimation

The OH steady-state concentration in the chamber was estimated from the rate of depletion of the VOC reactant, in this case, toluene. The rate of change of toluene concentration is given by Equation 4.1.

$$\frac{d[VOC]}{dt} = -k_{OH} [OH]_{SS} [VOC] + k_{wall} \quad (4.1)$$

Where  $[VOC]$  is the concentration of toluene.  $\frac{d[VOC]}{dt}$  is the change in toluene concentration with time,  $k_{OH} = 5.63 \times 10^{-12} \text{ cm}^3 \text{ molecule}^{-1} \text{ s}^{-1}$  is the bimolecular rate constant for the reaction of toluene with the OH radical,  $[OH]_{SS}$  is the steady-state OH radical concentration, and  $k_{wall}$  is the loss rate due to uptake into the chamber wall and leaks, which is a minor process under our conditions. The gas-phase concentration of toluene, monitored by the  $^{13}\text{C}$  isotope  $[^{13}\text{C}_6\text{H}_8 + \text{H}]^+$ , was measured here using a Proton Transfer Time of Flight Mass Spectrometer (PTR-ToF-MS; Ionicon model 8000, Innsbruck, Austria), shown in Figure 4.1(a). Integrating Equation 4.1 and incorporating these values, we determined the OH steady-state concentration from Figure 4.1(b) to be about  $6 \times 10^6 \text{ molecules cm}^{-3}$ .

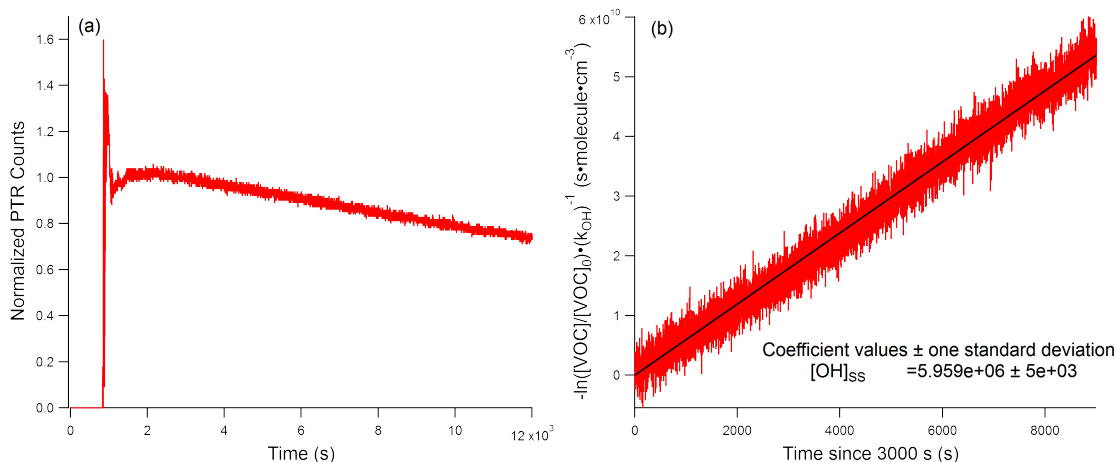


Figure 4.1: PTR-ToF-MS data using the  $[^{13}\text{C}_6\text{H}_8 + \text{H}]^+$  trace to estimate the OH steady-state concentrations in the chamber during SOA formation. The unsteady signal at early times arises from incomplete mixing in the chamber during the toluene injection. Panel (a) shows the data series normalized to the count value at 3000 s where we began the linear fit in panel (b). Panel (b) shows  $-\ln\left(\frac{[\text{VOC}]}{[\text{VOC}]_0}\right) \times k_{\text{OH}}^{-1}$ , with  $\frac{[\text{VOC}]}{[\text{VOC}]_0}$  being the normalized PTR counts shown in panel (a) as a function of time since 3000 s as a rearrangement of Equation 4.1. The slope of this trace represents the OH steady-state concentration in the chamber.

### 4.3.2 Photolysis Experiments

SOA samples were exposed to near-UV radiation from a Xenon arc lamp (Newport Model 66902). The broadband light was reflected at a  $90^\circ$  angle with a dichroic mirror and then passed through a 295 nm long-pass filter (Schott WG295) and a UV bandpass filter (Schott BG1) to remove UVC and visible wavelengths, leaving the majority of the radiation between 280 and 400 nm. A comparison of our lamp spectrum and ambient sunlight is shown in Figure 4.2 and Table 4.3. The comparison shows that, in terms of the 280-400 nm radiation dose, 1 h in our photolysis setup is equivalent to approximately 1.7 h under the 24-hour average Los Angeles solar flux (average taken for June 20th) as calculated using the Quick TUV calculator.<sup>142</sup> Photolysis was carried out for 5 h through the side of a 0.5 cm quartz cuvette containing SOA solution exposed to open air for the aqueous samples or with a filter quarter placed such that the filter surface was uncovered and open to laboratory air in the same position as the cuvettes used in the aqueous experiments. Three photolysis experiments

were performed for each experimental condition, as well as one additional experiment for photolysis in pure water and photolysis on-filter to be used for offline-AMS and UPLC-PDA-HRMS, as described in Table 4.2. Further experimental details on the two setups are provided in the following sections.

#### 4.3.2.1 Scaling Photodegradation Rates to Atmospheric Conditions

The effective rate of photodegradation of SOA is given by Equation 4.2.

$$J = \int F(\lambda)\phi(\lambda)\sigma(\lambda)d\lambda \quad (4.2)$$

Where  $F(\lambda)$  is the spectral photon flux density,  $\phi(\lambda)$  is the quantum yield for dissociation, and  $\sigma(\lambda)$  is the effective Napierian (i.e., base  $e$ ) absorption cross-section of the SOA. To calculate the predicted relative photodegradation rate in the atmosphere, we assumed the dissociation quantum yield was constant over the UV region (280 to 400 nm) and that the absorption cross-section of the SOA could be expressed as the measured mass absorption coefficient (MAC) scaled by a wavelength-independent constant. The relative rate of photodegradation in the atmosphere then simplifies to Equation 4.3.

$$\frac{J_{atmosphere}}{J_{lamp}} = \frac{\int F_{atmosphere}(\lambda)MAC(\lambda)d\lambda}{\int F_{lamp}(\lambda)MAC(\lambda)d\lambda} \quad (4.3)$$

The spectral photon flux density ( $F(\lambda)$ ) and its product with MAC ( $F(\lambda) \times MAC(\lambda)$ ) for our photolysis set-up, the 24 h average values for LA (taken on June 20<sup>th</sup>), and the maximal achievable flux at the SZA = 0 are shown in Figure 4.2 and the ratios of theoretical atmospheric photodegradation rate to photodegradation rate in our set-up are shown in Table 4.3 The parameters used for the “Quick TUV” calculator,<sup>142</sup> which was used to estimate the spectral flux densities, were:

- Latitude/Longitude: 34°N 118°W or SZA = 0
- Date and Time: June 20, 2021
- Overhead Ozone: 300 du
- Surface Albedo: 0.1
- Ground Altitude: 0 km
- Measured Altitude: 0 km
- Clouds Optical Depth/Base/Top: 0.00/4.00/5.00
- Aerosols Optical Depth/S-S Albedo/Alpha: 0.235/0.990/1.000
- Sunlight Direct Beam/Diffuse Down/Diffuse Up: 1.0/1.0/0.0
- 4 streams transfer model

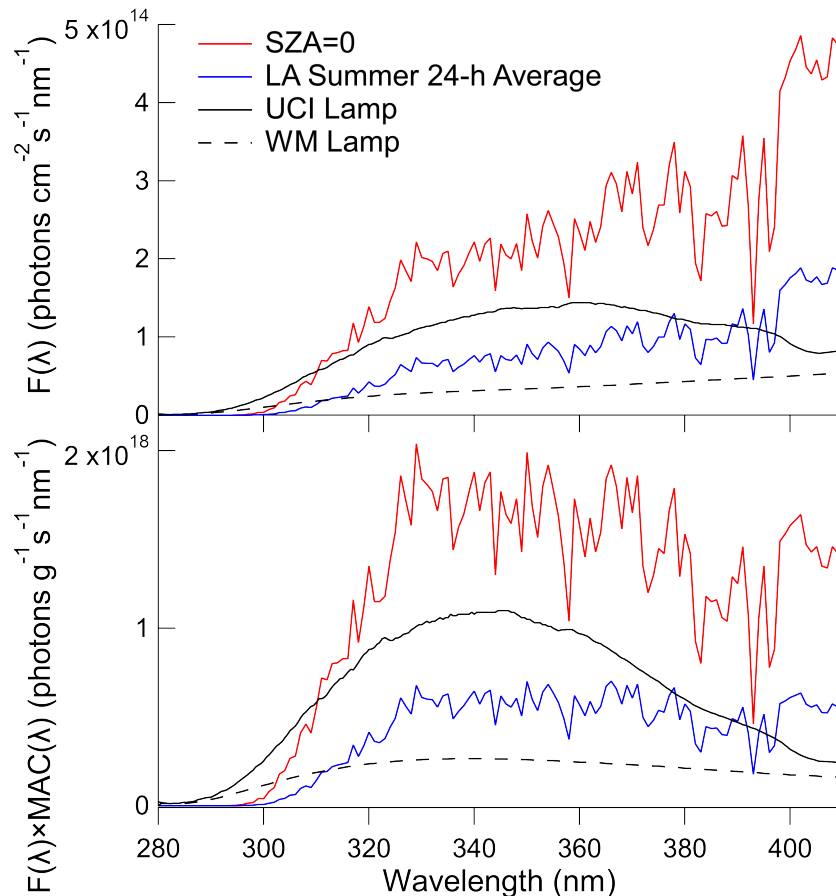


Figure 4.2: Spectral photon flux density ( $F(\lambda)$ ) and its product with the mass absorption coefficient ( $F(\lambda) \times MAC(\lambda)$ ) for UCI photolysis lamp (black solid), WM photolysis lamp (black dashed), solar zenith angle zero (red), and the Los Angeles 24-h average (blue).

Table 4.3: The integrated photon flux densities and the number of hours equivalent to one hour under the UCI and WM photolysis set-ups for the 24-h average solar flux in Los Angeles, California in summer and the maximal achievable flux at the  $SZA = 0$ . The calculation was performed by integrating  $F(\lambda) \times MAC(\lambda)$  from Figure 4.2 from 280 to 400 nm, the UV wavelength range that likely drives photochemistry for our samples. The values on the last two columns represent the ratios of the UV lamp's integrated flux to the solar integrated flux.

Lamp location	Integrated $F(\lambda) \times MAC(\lambda)$ from the UV lamp (photons $\text{g}^{-1} \text{s}^{-1}$ )	Integrated $F(\lambda) \times MAC(\lambda)$ for the 24h-average in Los Angeles (photons $\text{g}^{-1} \text{s}^{-1}$ )	Equivalent hours at 24-h average sunlight in Los Angeles
UCI	$7.94 \times 10^{19}$	$4.62 \times 10^{19}$	1.7
WM	$2.35 \times 10^{19}$	$4.62 \times 10^{19}$	0.5

### 4.3.2.2 Aqueous Photolysis Experiments

Aqueous UV-irradiation of the samples was carried out at UCI. After several preliminary experiments to determine the best combination of experimental parameters, including extraction methods and aging conditions, three filters of SOA (numbered 4, 5, and 6 in Table 4.2) were collected. Each filter was cut in half so that half of the filter could be extracted with acetonitrile and then photolyzed in water and the other half extracted with acetonitrile and then photolyzed in 1 M ammonium sulfate. Each filter was weighed whole, and then each half of the filter was weighed for a more accurate estimation of the mass of aerosol used in each experiment. The SOA material was extracted from the filter half by shaking it gently for 10 min in 5 mL of acetonitrile. The acetonitrile was then removed by rotary evaporation at room temperature (to avoid losing more volatile SOA compounds), and 2.1 to 3 mL of Milli-Q water (18.2 M $\Omega$ -cm, generated using a Thermo Scientific Barnstead NANOpure system) or 1 M ammonium sulfate solution was added to the SOA residue for the photolysis experiments. The SOA dissolved readily in the solution, so no further shaking was necessary. The SOA mass concentration in the solutions was close to 250 mg L<sup>-1</sup> in all trials (the actual mass concentrations for individual trials are shown in Table 4.4), and the unadjusted pH of the solutions was about 4.5 in both the ammonium sulfate and pure water conditions. These values are comparable to atmospheric cloud water, which generally contains about 100 mg L<sup>-1</sup> of dissolved organics and has pH values of between 3 and 6, but the concentrations of organics used here are likely lower than found in particulate matter.<sup>49,180,181</sup> The solutions were split into three 0.7 to 1 mL (depending on the mass of SOA on the filter) aliquots to serve as the unaged, dark aged, and photolyzed samples. The aliquot designated as “unaged” was prepared immediately for mass spectrometry analysis as described in the next paragraph. As high concentrations of inorganic ions should not be used with electrospray mass spectrometry, it was necessary to remove the ammonium sulfate from the SOA solutions before performing mass spectrometry analysis. Salt removal for mass spectrometry analysis is com-

monly accomplished using solid phase extraction (SPE).<sup>182</sup> However, SPE for inorganic salt extraction has been shown to reduce the recovery of more highly oxygenated and polar compounds as compared to organic solvent extracts, and these compounds are important for our analysis of SOA composition.<sup>183</sup> Therefore, we chose to extract with organic solvent rather than use SPE. To this end, the majority of the water was removed by rotary evaporation at room temperature. Water removal was stopped when the ammonium sulfate began to precipitate out of the solution, but care was taken to not evaporate to dryness, as evaporation of water in the presence of ammonium sulfate has been shown to cause condensation-type reactions that change the SOA composition.<sup>184</sup> The SOA was extracted from the vial containing ammonium sulfate by adding 5 mL of acetonitrile in two 2.5 mL rinses (the addition of acetonitrile caused most of the remaining ammonium sulfate to precipitate and all liquid was removed from the vial). This acetonitrile was also removed by rotary evaporation at room temperature, and a 1:1 mixture of water:acetonitrile was added to the SOA such that the SOA concentration was about 350 mg L<sup>-1</sup>, assuming complete extraction, for mass spectrometry analysis. The same procedure was used for the solutions which did not contain ammonium sulfate for the sake of consistency.

Table 4.4: Summary of aqueous SOA samples and their mass concentrations for aqueous-phase photolysis experiments. Mass concentrations from the same filter vary slightly between experiments aged in water versus aged in ammonium sulfate because the exact mass of the filter half was divided by the total mass of the filter and then multiplied by the mass of SOA collected in an attempt to account for differences in sizes of the filter sections. The mass concentrations are still somewhat approximate because the SOA may not have been completely evenly distributed on the filter after collection.

Photolysis experiment	Filter number	Mass concentration for photolysis (mg L <sup>-1</sup> )
Water 1	4	233
Water 2	5	220
Water 3	6	238
Ammonium Sulfate 1	4	224
Ammonium Sulfate 2	5	249
Ammonium Sulfate 3	6	253



### 4.3.2.3 On-Filter Photolysis Experiments

Preliminary on-filter photolysis experiments, from Filters 1 and 2 in Table 4.2, were performed at WM. Samples were irradiated in a photolysis box that has been described previously.<sup>185</sup> Briefly, the filter was sliced into four segments and three of the segments were placed in the box mounted vertically in front of a Xenon arc lamp (Newport model 66902). The photolysis box was air-tight, had a Teflon film (0.001 in inch) taped across a hole cut into the front panel to allow the UV radiation pass through, and had  $\sim 1\text{-}2\text{ L min}^{-1}$  of zero air (EnviroNics 7000) at 50-60% RH continuously flowing through it. The spectral flux density on the irradiated filters is shown in Figure 4.2. A second dark box was placed after the photolysis box with the same airflow. The control filter segment was placed there immediately, the second filter segment was moved there after 6 h of photolysis, the third filter segment was moved there after 18 h, and the irradiation ended after 24 h. This ensured that all the filter segments were exposed to the same airflow for the same amount of time, resulting in comparable SOA material loss to vaporization. The observed differences should therefore be dominantly due to photolysis, although we cannot fully rule out additional volatilization due to absorption of light by the chromophores in the SOA material.

These experiments were then replicated at UCI to allow better intercomparison with the aqueous results using the same photolysis set-up, especially since the WM and UCI photolysis set-ups had different spectra and intensities. Both photobleaching kinetics and UPLC-PDA-HRMS experiments for the on-filter samples were performed at UCI. Filters 7, 8, and 9 were cut into quarters, and each quarter was weighed to get a better estimate of the mass of toluene SOA used for each data point. For aging, one filter quarter was placed in front of the photolysis set up such that the filter surface was uncovered and open to laboratory air. While not being photolyzed, the other filter quarters were re-sealed and kept frozen. After photolysis, the filter quarter was extracted with acetonitrile to take a UV-Vis spectrum with the instrument described above. Since UV-Vis sample preparation was destructive, each

time point required an entire filter quarter and so only four time points could be taken per filter. Based on the observed photobleaching rate, 0, 1, 3, and 5 h were chosen as time points.

### 4.3.3 Sample and Data Analyses

#### 4.3.3.1 UV-Vis Analyses

A UV-Vis spectrometer (Shimadzu UV-2450) was used to observe the change in optical properties during photolysis in water or 1 M ammonium sulfate solution. The spectrometer was a double-beam instrument, and the sample solvent was used in the reference cell for each experiment (water for samples collected in water, 1 M ammonium sulfate for samples collected in 1 M ammonium sulfate, etc.). The UV-Vis spectra for the aqueous samples were collected in the 0.5 cm quartz cuvettes used for aging. Data collection involved moving the whole cuvette from in front of the irradiation set up into the UV-Vis spectrometer, taking the spectrum, and then returning the sample to the irradiation set up. Therefore, each UV-Vis spectrum was taken only once per sample at each time point. To keep the organic concentration similar for the on-filter and aqueous photolysis samples, the same 0.5 cm cuvettes were also used after extraction for the samples photolyzed on the filter, although the UV-Vis spectra were taken in acetonitrile (rather than water) after it was confirmed that the spectra did not look different between the two solvents (see section 4.3.3.2 on Extraction Efficiency). In the samples where a baseline shift was observed at long wavelengths, corrections were applied by averaging the absorbance from 680 to 700 nm and subtracting the average from all wavelengths (there are no strong absorbers in the SOA at these wavelengths). These corrections were never greater than 0.011 absorbance units. At the sample concentrations used here, the UV-Vis absorbance was less than 1 at all wavelengths longer than 250 nm and within the linear range of the instrument.

The UV-Vis data were used to calculate the mass absorption coefficient (MAC):

$$MAC(\lambda) = \frac{A_{10}(\lambda) \times \ln(10)}{b \times C_{org}} \quad (4.4)$$

where  $A_{10}(\lambda)$  is base-10 absorbance,  $b$  is the path length, and  $C_{org}$  is the mass concentration of the SOA sample in solution ( $\text{g cm}^{-3}$ ). Additionally, SOA recovery for each step of the procedure was roughly determined by UV-Vis spectroscopy as the experiment went on, and the results of these checks are provided in the next section.

#### 4.3.3.2 Extraction Efficiency Determination

After the initial extraction of the filter with 5 mL of acetonitrile, the filter was re-extracted in 3 mL of methanol and a UV-Vis spectrum was taken (Figure 4.3(a)). Assuming that the integrated absorbance between 250 nm and 550 nm can be used as a metric for the amount of extracted SOA, >90% of the SOA was extracted from the filters. SOA recovery from the aqueous solution (Figure 4.3(b)) and the ammonium sulfate solution (Figure 4.3(c)) was also tested. After the SOA was extracted from the evaporated solution of SOA in water or ammonium sulfate, 1 mL of water was added back to the empty vial or the residual salt, replacing the 1 mL of water that had been removed by rotary evaporation, and a UV-Vis spectrum was taken. A comparison of the post-extraction spectrum with the initial spectrum shows that the extraction procedure generally recovered about 50-70% of the SOA from the ammonium sulfate solution and greater than 90% from the solutions without ammonium sulfate. The reason for the retention of some 30-50% SOA by the wet ammonium sulfate residue is unclear and will be investigated in the future.

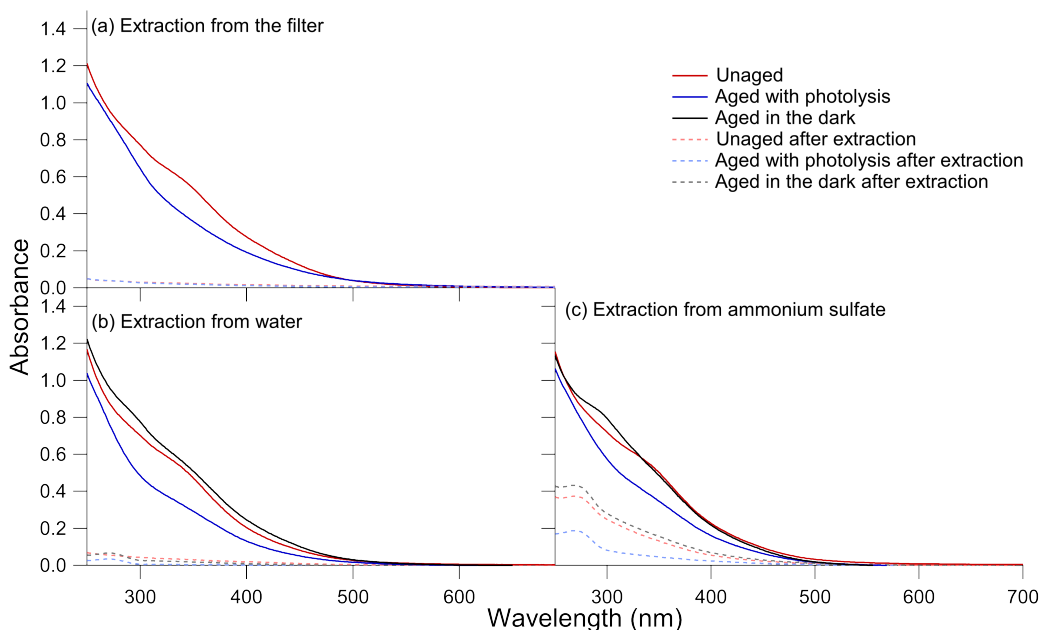


Figure 4.3: A test of the extraction efficiency of the toluene SOA (a) from the Teflon filters, (b) from the pure water solutions, and (c) from the 1 M ammonium sulfate solutions.

#### 4.3.3.3 UPLC-HRMS Analysis

Changes in the molecular composition of the UV-irradiated SOA were analyzed by high-resolution mass spectrometry (HRMS) similar to as described previously.<sup>186</sup> Briefly, the instrument was a Thermo Q-Exactive Plus mass spectrometer (Thermo Scientific) with a resolving power of  $1.4 \times 10^5$  at  $m/z$  400 equipped with a heated electrospray ionization inlet. The instrument was operated in both positive (spray voltage +3.5 kV) and negative ion modes (spray voltage -2.5 kV). Ultrahigh performance liquid chromatography (UPLC) and photodiode array (PDA) detection (scanning 190 to 680 nm) were performed to analyze the relative contributions of individual compounds to the total SOA absorption. The column was Phenomenex Luna Omega Polar C18,  $150 \times 2.1$  mm, with  $1.6 \mu\text{m}$  particles and  $100 \text{ \AA}$  pores. The UPLC solvent gradient was 95% solvent A (water acidified to pH 3 with 0.1% formic acid) and 5% solvent B (acetonitrile acidified with 0.1% formic acid) for minutes 0 to 3, followed by a linear ramp to 95% solvent B and 5% solvent A from 3 to 14 minutes, a hold at 95% solvent B from 14 to 16 minutes, and a linear ramp back to 95% solvent

A and 5% solvent B for 16 to 22 minutes in preparation for the next run. Separating the samples via liquid chromatography provided the benefit of reducing matrix effects and preventing ionization suppression from any inorganic ions not removed during the extraction process. The separation additionally allowed us to assign formulas to specific peaks in the PDA chromatogram and therefore better quantify formulas that decreased or remained stable in abundance during photolysis, improving characterization.

Analysis of the PDA-HRMS data was performed using FreeStyle 1.6 from Thermo Scientific, and the peaks with the greatest absorbance when the PDA chromatogram was integrated from 300 and 700 nm were correlated to the peaks in the total ion chromatogram (TIC) based on the instrument's PDA-MS time delay of 0.06 min. Molecular formulas for these chromophores were determined using FreeStyle. Additionally, FreeStyle was used to integrate over the full total ion chromatogram and generate a raw time-integrated (1 to 18 min) mass spectrum. Decon2LS (<https://omics.pnl.gov/software/decontools-decon2ls>) was used to extract peak positions and relative intensities from the time-integrated mass spectrum, and peaks representing  $^{13}\text{C}$  compounds were removed. Peaks from the blank, unaged, and two aging conditions were aligned with a tolerance of 0.0005 m/z. A blank sample was prepared by repeating the SOA extraction and mass spectrometry preparation process with a clean filter. Peaks that were present in the blank at the same or greater intensity as the samples were also removed. Finally, the mass spectra were assigned assuming an accuracy of 0.0005 m/z with a formula of  $[\text{C}_c\text{H}_h\text{O}_x\text{N}_{0-3}\text{S}_{0-1} + \text{Na}]^+$  and  $[\text{C}_c\text{H}_h\text{O}_x\text{N}_{0-3}\text{S}_{0-1} + \text{H}]^+$  for positive ion mode and  $[\text{C}_c\text{H}_h\text{O}_x\text{N}_{0-3}\text{S}_{0-1} - \text{H}]^-$  for negative ion mode (although no sulfur-containing compounds were identified with greater than 0.01% abundance of the maximum peak height). Assigned peaks were used to verify the internal calibration of the m/z axis in both ion modes and adjust the calibration if needed. The internal calibration improved the m/z accuracy and usually led to a few additional assignments for peaks that could not be assigned within 0.0005 m/z in the uncalibrated mass spectra. Finally, neutral formulas were determined from the assignments, and the data from the positive and negative

ion modes were clustered together. The mass spectra presented below show the combined peak abundance in the positive and negative ion mode data referenced to formulas of the unionized SOA compounds.

#### **4.3.3.4 FTIR Analysis**

A Shimadzu IR Tracer-100 MIRacle 10 with a diamond crystal ATR probe was used to collect ATR-FTIR spectra from 600-4000  $\text{cm}^{-1}$ . A total of 45 scans were averaged per sample, and for each sample, an air background was collected before the filter was adhered to the crystal. After irradiating the filter segments for 0 (control), 6, 18, and 24 h, small slivers of the filters were cut off and pressed onto an ATR-FTIR crystal (diamond) using the swivel press. The filters were then detached, an unpressed area of the filter was moved overtop the crystal, and the filter was pressed onto the crystal again. After the second press, the filters were removed from the crystal, leaving behind a thin film of sample material. The spectra of the adhered SOA without the Teflon filter were collected. The spectra were converted to absorbance and the baseline for each spectrum was corrected using a Baseline Spline Fit (<http://wavemetrics.com/project/BaselineSpline>) using an Akima spline. The baseline corrected spectra were normalized to the total absorbance and smoothed with a three-point rolling average to improve inter-comparison.

#### **4.3.3.5 Offline-AMS Analysis**

A High-Resolution Time-of-Flight Aerosol Mass Spectrometer (HR-ToF-AMS or AMS; Aerodyne, Billerica, MA, USA) operated in V-mode and a custom ultrasonic small volume nebulizer, described elsewhere,<sup>187</sup> were used to analyze the composition during and after photolysis. For AMS analysis, particles were vaporized at 600 °C and ionized using electron impact ionization at 70 eV. For the ultrasonic small volume nebulizer, sample preparation involved

combining  $\sim 3$   $\mu\text{L}$  of sample solutions with  $\sim 2$   $\mu\text{L}$  of internal standard solution, consisting of a mixture of  $0.25$   $\text{g L}^{-1}$  isotopically labeled  $\text{NH}_4^{15}\text{NO}_3$  and  $0.25$   $\text{g L}^{-1}$   $\text{NH}_4\text{I}$ . The  $5$   $\mu\text{L}$  of prepared sample was then loaded onto a clean Kapton film in the nebulizer. The sample was nebulized, and the aerosol particles were carried with a flow of clean air into the inlet of the AMS. The AMS data were analyzed with Igor Pro (version 7.0.8.1, WaveMetrics Inc.) using the ToF-AMS Analysis Toolkit 1.63H and ToF-AMS HR Analysis 1.23H software packages. The signals for the  $\text{NO}^+$  and  $\text{NO}_2^+$  ions were quantified for each injection and intercompared between different samples after calculating the ratios with the signals for the corresponding isotopically labeled ions from the ammonium nitrate internal standard ( $^{15}\text{NO}^+$  and  $^{15}\text{NO}_2^+$ ).

## 4.4 Results and Discussion

### 4.4.1 Optical Properties

Figure 4.4 shows how the wavelength-dependent MAC of toluene SOA changes with photolysis and under dark conditions. The decrease in absorption between  $300$  and  $700$  nm over the five hours of photolysis was used to calculate the photobleaching lifetime of the chromophoric compounds in the SOA. Previous work on toluene SOA suggests the absorption band at  $350$  nm, the most prominent peak in the spectrum, is mostly attributable to the  $\pi$  to  $\pi^*$  transition of nitrophenols, such as methylnitrocatechol.<sup>176</sup>

The time-dependent change in absorbance integrated from  $300$  to  $700$  nm for all photolysis conditions is shown in Figure 4.5. In the case of the aqueous samples, a correction was applied for absorbance changes occurring in the dark by subtracting the change in integrated MAC as compared to time zero for the dark condition from the integrated MAC of the corresponding photolysis condition. This was particularly necessary for the  $1$  M ammonium sulfate trials because a small peak slowly forms at  $300$  nm under these conditions in the dark (see Figure

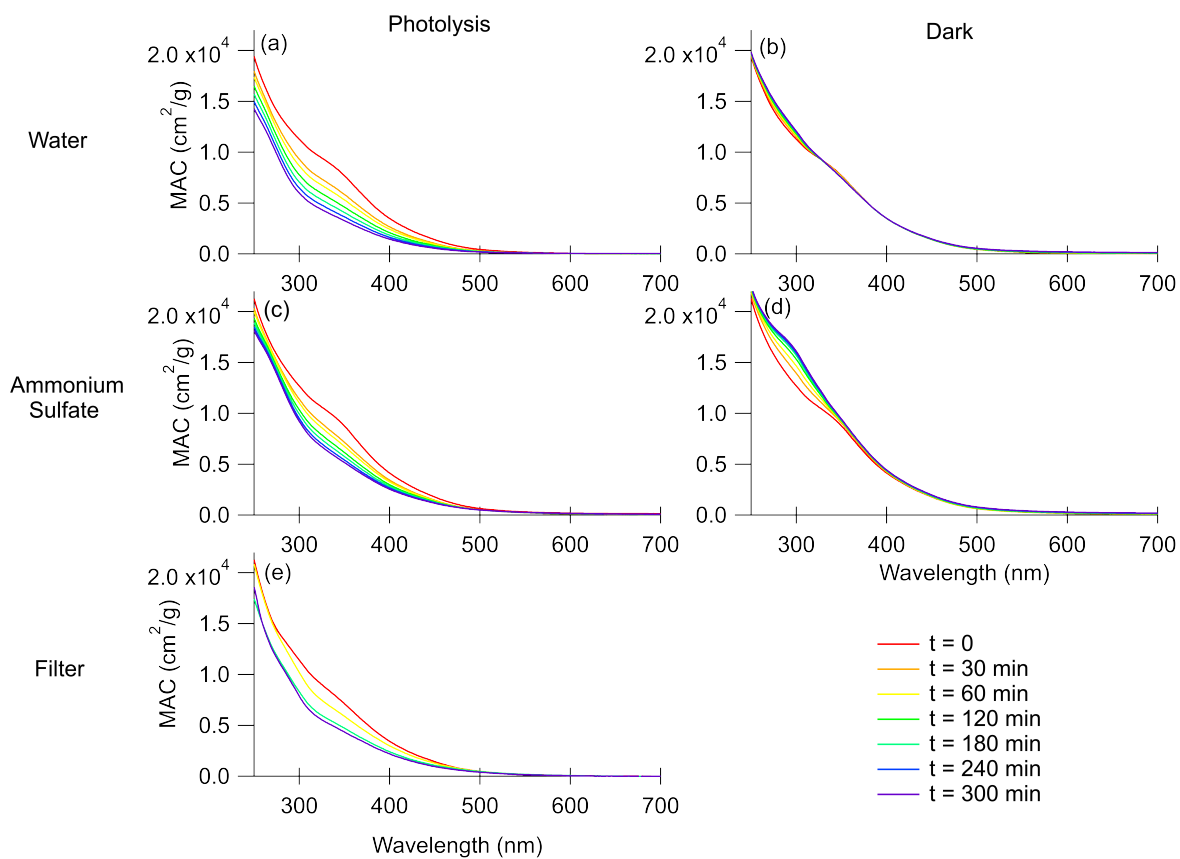


Figure 4.4: The wavelength-dependent mass absorption coefficient plots for each experimental condition and control. Photolysis in water is in panel (a), dark aging in water is in panel (b), photolysis in 1 M ammonium sulfate is in panel (c), dark aging in 1 M ammonium sulfate is in panel (d), and photolysis on the filter is in panel (e). Note that there are only four traces for the filter photolysis in panel (e) because measuring the absorbance requires extraction of the filter and therefore is destructive.



4.4) as a result of ammonia-carbonyl reactions.<sup>25</sup> The integrated MAC values for the dark controls and a fit to the MAC changes are shown in Figure 4.6. The absorbances over time were then normalized to the initial absorbance (t=0) and were fit to the biexponential decay shown in equation (2),

$$y(t) = A_1e^{-k_1t} + A_2e^{-k_2t} \quad (4.5)$$

where  $y(t)$  is the normalized absorbance as a function of time,  $k_1$  and  $k_2$  are first-order rate constants for a faster and a slower process, and  $A_1$  and  $A_2$  are relative normalized absorbance contributions of compounds decaying through the faster and slower processes, respectively. We stress that this is a purely empirical fit, as in reality there are a large number of light-absorbing compounds in SOA, each with its own complex time dependence.

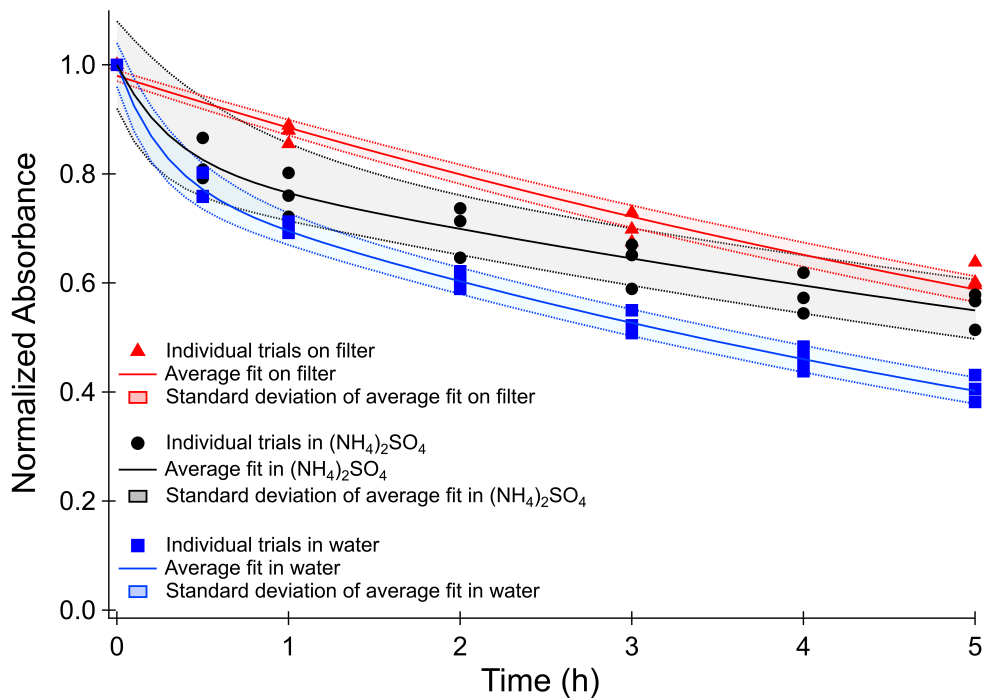


Figure 4.5: Normalized absorbance decay of the wavelengths integrated from 300 to 700 nm with photolysis. Photolysis experiments in 1 M ammonium sulfate are shown in black circles, in pure water are shown in blue squares, and on the filter are shown in red triangles. Values on the y-axis were corrected for changes in the dark and then normalized to the mass absorption coefficient at zero minutes. Shaded areas represent one standard deviation of the fit of the three combined trials.

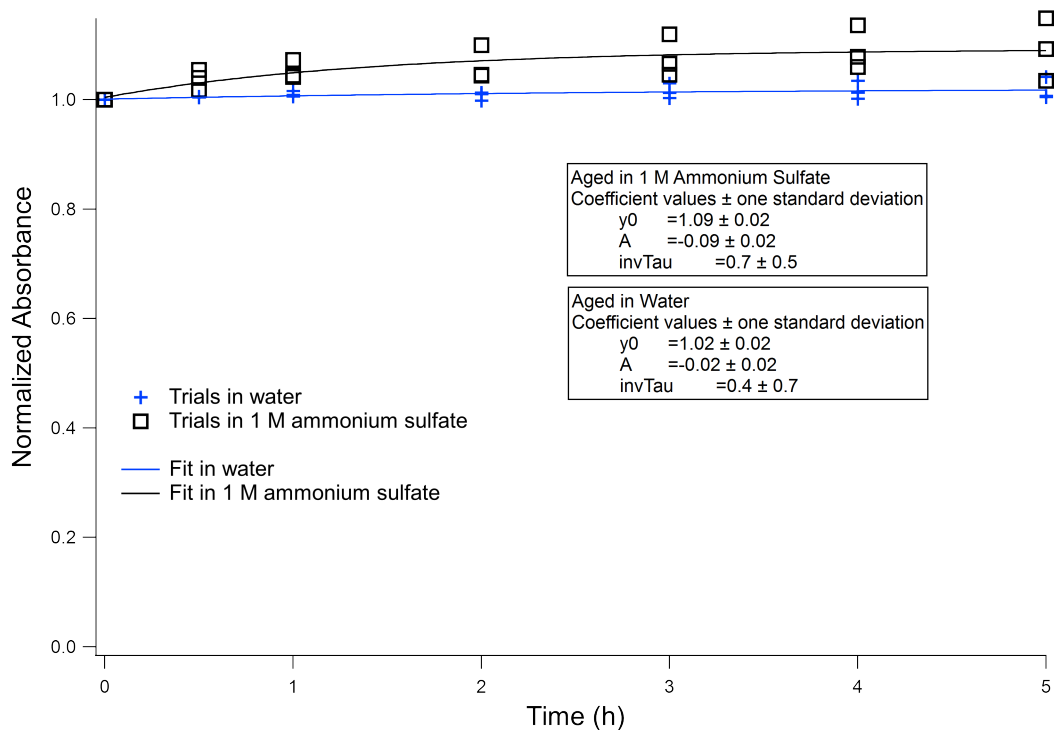


Figure 4.6: Changes in the normalized absorbance of wavelengths integrated from 300 to 700 nm in the dark for aqueous samples. Individual trials aged in water are shown with blue crosses and individual trials aged in 1 M ammonium sulfate are shown with black squares. Fits are shown in blue for water and black for 1 M ammonium sulfate. The slight increase in absorbance in the ammonium sulfate solutions is due to reactions of ammonia with SOA carbonyl compounds producing light-absorbing products.

Based on this analysis, we observed a considerably slower decay in MAC on-filter as compared to in the aqueous phase. However, for the filter samples, we could only collect 4 data points, which may introduce a bias in our analysis. In particular, the on-filter data did not include the 0.5 h time point, which characterizes the fast-reacting chromophore pool in the aqueous samples. As a result,  $A_1$  was constrained to zero for the filter samples to avoid over-fitting, and this fit is shown in Figure 4.5. The fit for the on-filter data can be improved slightly by including a parameter representing a photorecalcitrant fraction ( $R^2=0.99$  compared to  $R^2=0.97$ ), shown in Figure 4.7. Previous studies have found significant fractions of photorecalcitrant material when SOA photolysis was performed in the organic particle phase, including for toluene high- $\text{NO}_x$  SOA,<sup>77,185,188,189</sup> and based on these previous studies we expect a photorecalcitrant fraction for the SOA studied here. When the photorecalcitrant fraction was not constrained to zero, the fit obtained estimates a large photorecalcitrant absorbance fraction ( $49 \pm 5\%$ ). This fraction of photorecalcitrant absorbance is similar to the Baboornian et al.<sup>77</sup> estimate of 50% photorecalcitrant mass fraction after photolysis of toluene-derived high- $\text{NO}_x$  SOA deposited on a gold surface. Future longer-term photolysis experiments on filters are needed to quantify what fraction of the absorbance is fully photorecalcitrant in the atmosphere versus much slower than the rates observed for the aqueous samples.

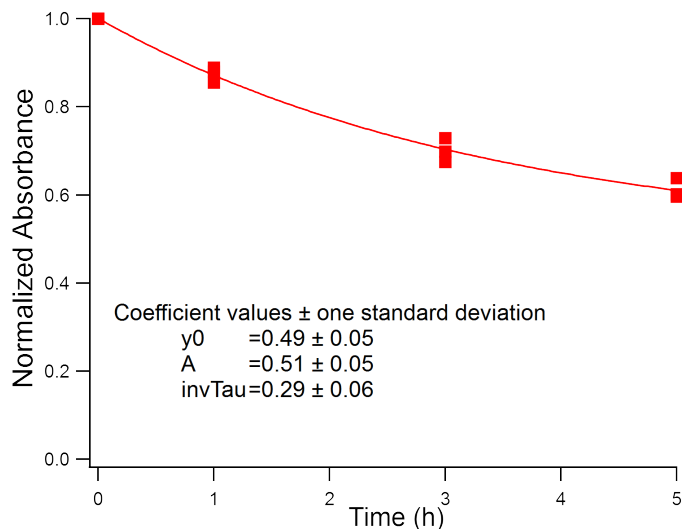


Figure 4.7: Normalized absorbance decay of wavelengths integrated from 300 to 700 nm with photolysis on the filter fit to a single exponential decay without constraining absorbance at time infinity to zero, i.e. allowing a photorecalcitrant fraction.

Calculated fitting parameters from Figure 4.5 are summarized in Table 4.5. Absorbance lifetimes calculated from these values and scaled to the 24-h average solar actinic flux in Los Angeles, California are shown in Table 4.6. The shortest photobleaching lifetimes are seen for photolysis in water, while the lifetimes are about twice as long in 1 M ammonium sulfate.

Table 4.5: Kinetic parameters for exponential and biexponential fits to absorbance data. Error represents the standard deviation of fitting parameters over the three combined trials.

Aging condition	$A_1 \pm 1$ std dev	$k_1 \pm 1$ std dev ( $\text{h}^{-1}$ )	$A_2 \pm 1$ std dev	$k_2 \pm 1$ std dev ( $\text{h}^{-1}$ )
H <sub>2</sub> O	$0.79 \pm 0.02$	$0.135 \pm 0.007$	$0.21 \pm 0.02$	$3.7 \pm 1.0$
AS	$0.85 \pm 0.04$	$0.08 \pm 0.01$	$0.18 \pm 0.04$	$3.1 \pm 1.7$
Filter	NA	NA	$0.98 \pm 0.01$	$0.102 \pm 0.006$

Table 4.6: Absorbance lifetimes for photobleaching processes described by Equation 4.5 scaled to the 24-h average solar actinic flux in Los Angeles. Errors represent the standard deviations over the three combined trials.

Aging condition	$\tau_1 \pm 1$ std dev (h)	$\tau_2 \pm 1$ std dev (h)
H <sub>2</sub> O	$0.5 \pm 0.12$	$12.6 \pm 0.7$
AS	$0.5 \pm 0.30$	$21 \pm 2.7$
Filter	NA	$1.7 \pm 1.0$

## 4.4.2 Chemical Composition Changes with Photolysis

### 4.4.2.1 PDA Data

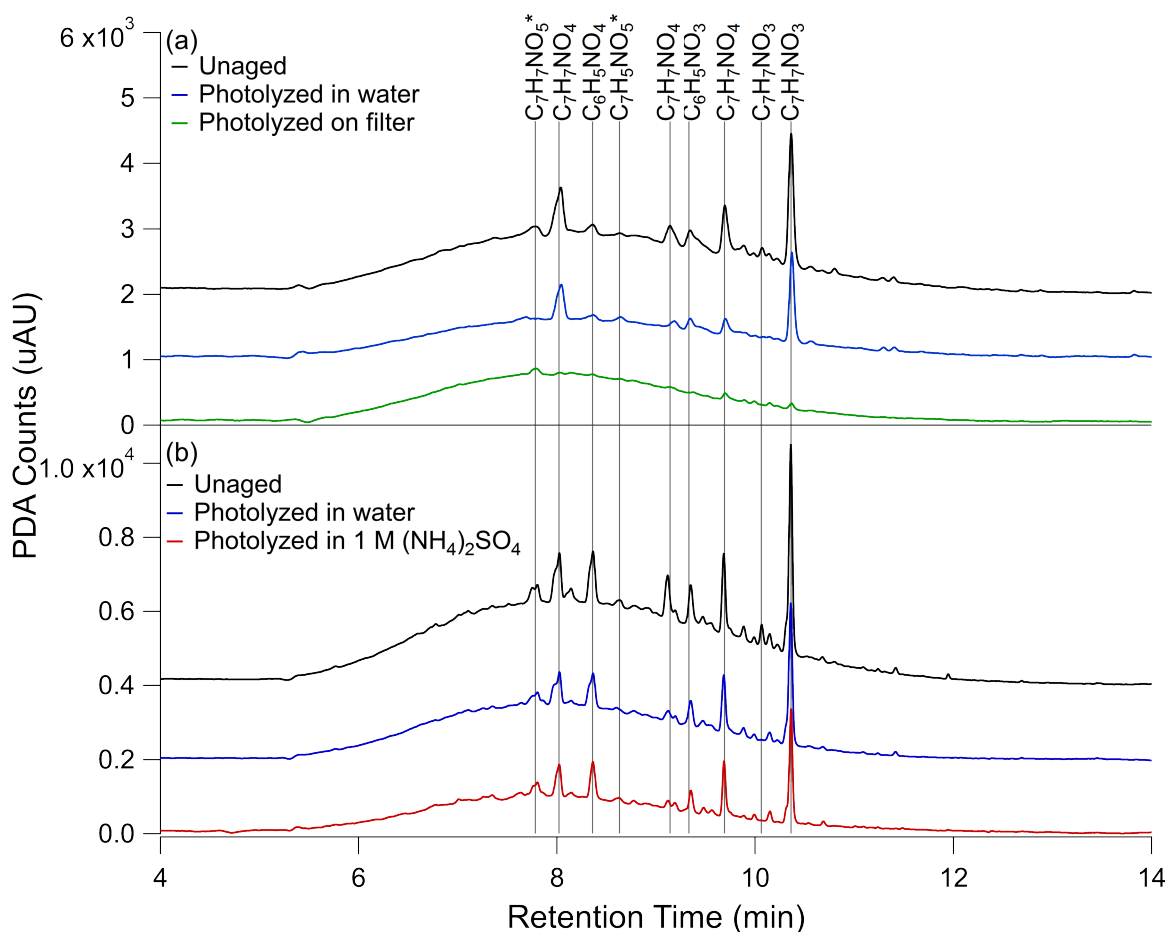


Figure 4.8: UPLC-PDA chromatograms for (a) unaged toluene SOA sample (black trace), photolyzed 5 h in water (blue trace), and photolyzed 5 h on the filter (green trace) from Filter 3 and (b) unaged toluene SOA (black trace), photolyzed 5 h in water (blue trace), and photolyzed 5 h in 1 M ammonium sulfate (red trace) from Filter 4. The black (unaged) and blue (photolyzed in water) traces are shown twice to illustrate the extent of reproducibility of this analysis. PDA counts were integrated over 300 to 680 nm wavelength range to match with the UV-Vis data analysis. A blank PDA spectrum (see Figure 4.9), also integrated from 300 to 680 nm, was subtracted from each PDA spectrum shown here. The peaks for which molecular formulas could be assigned are marked on the graph and their assigned formulas are indicated, while asterisks denote unnamed formulas. In the case of 1 M ammonium sulfate, PDA counts were adjusted for the estimated 50% extraction efficiency. Additionally, the baselines are each offset by  $10^3$  PDA counts on the y-axis of panel (a) and  $2 \times 10^3$  PDA counts on the y-axis of panel (b) for ease of comparison.

In an effort to tie the photobleaching behavior observed in the UV-Vis data to changes in composition, UPLC-PDA-HRMS analysis was performed on the samples before and after aging. PDA data for the photolysis conditions are shown in Figure 4.8 – unaged, photolyzed in water, and photolyzed on-filter from Filter 3 (Figure 4.8(a)) and unaged, photolyzed in water, and photolyzed in 1 M ammonium sulfate from Filter 4 (Figure 4.8(b)). The PDA counts were integrated from 300 to 680 nm to correspond to the analysis of the UV-Vis data. Under all conditions, a large fraction of the eluting compounds was unresolved, forming a broad peak stretching from 5 to 12 min. Superimposed on top of the unresolved peak were several well-resolved peaks. Additionally, some loss of resolution is seen between the two panels in Figure 4.8. We attribute this to the deterioration of the HPLC column as the data in Figure 4.8(b) were taken nearly a year before the data in Figure 4.8(a). To keep our conclusions robust, we compared the changes between the unaged and photolyzed in water samples, which are included in both experiments, and have excluded peaks that were not reproducible between the two trials from our discussion. In the unaged chromatogram, the most abundant species corresponding to major PDA peaks are all nitrophenol-type compounds. Those to which we were able to assign a chemical name based on previous work<sup>176</sup> include:  $C_7H_7NO_3$  (two structural isomers of nitroresol 10.06 and 10.36 min),  $C_7H_7NO_4$  (three structural isomers of methylnitrocatechol - 8.04, 9.14, and 9.69 min),  $C_6H_5NO_3$  (nitrophenol - 9.35 min), and  $C_6H_5NO_4$  (nitrocatechol - 8.37). The peaks for which the name is not known are marked with an asterisk in Figure 4.8. The major peaks marked in Figure 4.8 are also the most abundant compounds in the integrated mass spectrum shown in Figures 4.10 and 4.11.

In Figure 4.8(a), a significant difference can be seen in the PDA data after photolysis on the filter compared to photolysis in water. These differences are further quantified in Tables 4.7 and 4.8. After 5 h of photolysis in water (blue trace) there is only about a 40% change in the resolved features in both trials shown in Figure 4.8, but after 5 h of photolysis on the filter

(green trace) the resolved features are greatly reduced – by about 90%. By contrast, the area of the unresolved absorbance in the filter photolysis decreased by about 20% compared to the unaged sample (black trace) while the unresolved absorbance in the aqueous photolysis trace decreased by 35%. The control conditions (Figure 4.9) show little change in resolved or unresolved peak areas with dark aging, generally within 10% of the unaged condition.

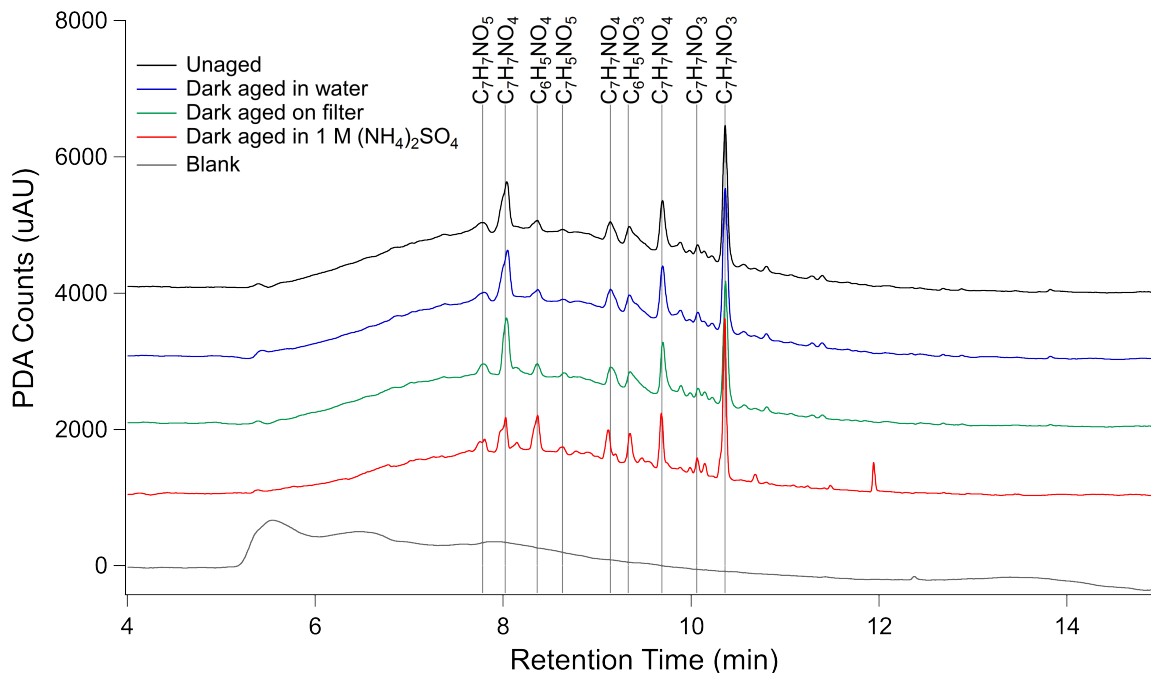


Figure 4.9: HPLC-PDA chromatograms for all dark conditions studied. PDA counts were integrated over 300 to 680 nm wavelength range. The blank PDA chromatogram shown as the last trace was subtracted from the rest of the traces. For display purposes, the traces are offset by adding  $10^3$  unit spacing between them.



Table 4.7: Formulas associated with the well-defined peaks in the integrated (300 to 680 nm) unaged PDA data and the percent change from unaged after aging for individual peaks, the total resolved peak area, and the area of the unresolved baseline. The area of the unresolved baseline feature was calculated by integrating the sample PDA from 300 to 680 nm and summing from 5 to 12 min and then subtracting the area of the blank integrated from 300 to 680 nm summed from 5 to 12 min and the area of the resolved peaks.

PDA Retention Time (min)	Neutral Formula	Dark aged in water (% change)	Photolyzed in water (% change)	Dark aged on filter (% change)	Photolyzed on filter (% change)
7.78	C <sub>7</sub> H <sub>7</sub> NO <sub>5</sub>	-18	-93	-13	-60
8.02	C <sub>7</sub> H <sub>7</sub> NO <sub>4</sub>	-1	-32	-11	-95
8.37	C <sub>6</sub> H <sub>5</sub> NO <sub>4</sub>	-19	-36	-5	-92
8.63	C <sub>7</sub> H <sub>5</sub> NO <sub>5</sub>	-47	43	4	-88
9.14	C <sub>7</sub> H <sub>7</sub> NO <sub>4</sub>	-1	-70	-12	-86
9.33	C <sub>6</sub> H <sub>5</sub> NO <sub>3</sub>	-7	-44	-9	-95
9.72	C <sub>7</sub> H <sub>7</sub> NO <sub>4</sub>	8	-69	3	-84
10.06	C <sub>7</sub> H <sub>7</sub> NO <sub>3</sub>	22	-92	-13	-100
10.35	C <sub>7</sub> H <sub>7</sub> NO <sub>3</sub>	12	-29	-9	-95
<b>Total area 5 to 12 min (minus blank area)</b>		<b>7</b>	<b>-35</b>	<b>-4</b>	<b>-29</b>
<b>(Defined peak area)</b>		<b>2</b>	<b>-44</b>	<b>-8</b>	<b>-90</b>
<b>Unresolved baseline (feature area)</b>		<b>8</b>	<b>-34</b>	<b>-3</b>	<b>-21</b>

Table 4.8: Formulas associated with the well-defined peaks in the integrated (300 to 680 nm) unaged PDA data and the percent change from unaged after aging for individual peaks, the total resolved peak area, and the area of the unresolved baseline. The area of the unresolved baseline feature was calculated by integrating the sample PDA from 300 to 680 nm and summing from 5 to 12 min and then subtracting the area of the blank integrated from 300 to 680 nm summed from 5 to 12 min and the area of the resolved peaks.

PDA Retention Time (min)	Neutral Formula	Dark aged in water (% change)	Photolyzed in water (% change)	Dark aged in 1 M $(NH_4)_2SO_4$ (% change)	Photolyzed in 1 M $(NH_4)_2SO_4$ (% change)
7.78	$C_7H_7NO_5$	12	-30	40	-27
8.02	$C_7H_7NO_4$	5	-24	-9	-32
8.37	$C_6H_5NO_4$	8	-33	-5	-25
8.63	$C_7H_5NO_5$	-21	-74	-29	-43
9.14	$C_7H_7NO_4$	3	-67	-13	-71
9.33	$C_6H_5NO_3$	10	-49	0	-47
9.72	$C_7H_7NO_4$	10	-27	9	-15
10.06	$C_7H_7NO_3$	-24	-99	-12	-100
10.35	$C_7H_7NO_3$	15	-32	-19	-40
<b>Total area 5 to 12 min (minus blank area)</b>		<b>9</b>	<b>-35</b>	<b>-19</b>	<b>-44</b>
<b>(Defined peak area)</b>		<b>9</b>	<b>-37</b>	<b>-2</b>	<b>-37</b>
<b>Unresolved baseline (feature area)</b>		<b>9</b>	<b>-35</b>	<b>-21</b>	<b>-45</b>

Figure 4.8(b) compares the PDA absorbance with photolysis in water and 1 M ammonium sulfate. The addition of ammonium sulfate produced results similar to pure water in the PDA chromatogram, although the lower extraction efficiency may influence these results. For instance, our calculations in Table 4.8 suggest the baseline feature decreased more with photolysis in 1 M ammonium sulfate (45%) than in water (35%) but considering the similar decrease in resolved peak area in the two conditions (both about 40%) and the slower photobleaching observed in the UV-Vis data with 1 M ammonium sulfate, this is likely an effect of extraction efficiency. If some compounds preferentially remain with the ammonium sulfate after extraction, we will miss them in this analysis.

#### 4.4.2.2 SOA Composition - High Resolution Mass Spectrometry

Unaged toluene SOA composition has been well characterized using HRMS previously,<sup>176</sup> so we will focus our discussion on composition changes before and after photolysis. Figure 4.10 compares the retention time-integrated SOA mass spectra for photolysis in water and on-filter (from Filter 3), while Figure 4.11 contrasts the behavior of SOA from a separate experiment in water and in 1 M ammonium sulfate (from Filter 4). In all cases, the mass spectra represent combined positive and negative ion modes scaled to the approximate mass concentration of organics in the samples. The mass spectra, including the sample extracted from 1 M ammonium sulfate, show excellent reproducibility in terms of the peak height of all major peaks and the shape of peak distribution after accounting for the concentration of organics in the mass spectrometry samples, demonstrating that the extraction method used here is effective for extracting SOA samples for mass spectrometry analysis. The unaged SOA mass spectra are dominated by nitrogen-containing compounds, the most abundant of which are  $C_7H_7NO_3$  (153 Da – nitrocresol) and  $C_7H_7NO_4$  (169 Da – methylnitrocatechol), in agreement with previous work on high- $NO_x$  toluene SOA.<sup>175,176,178</sup> It should be noted that these are also the most abundant peaks observed in the PDA data in Figures 4.8 and 4.9.

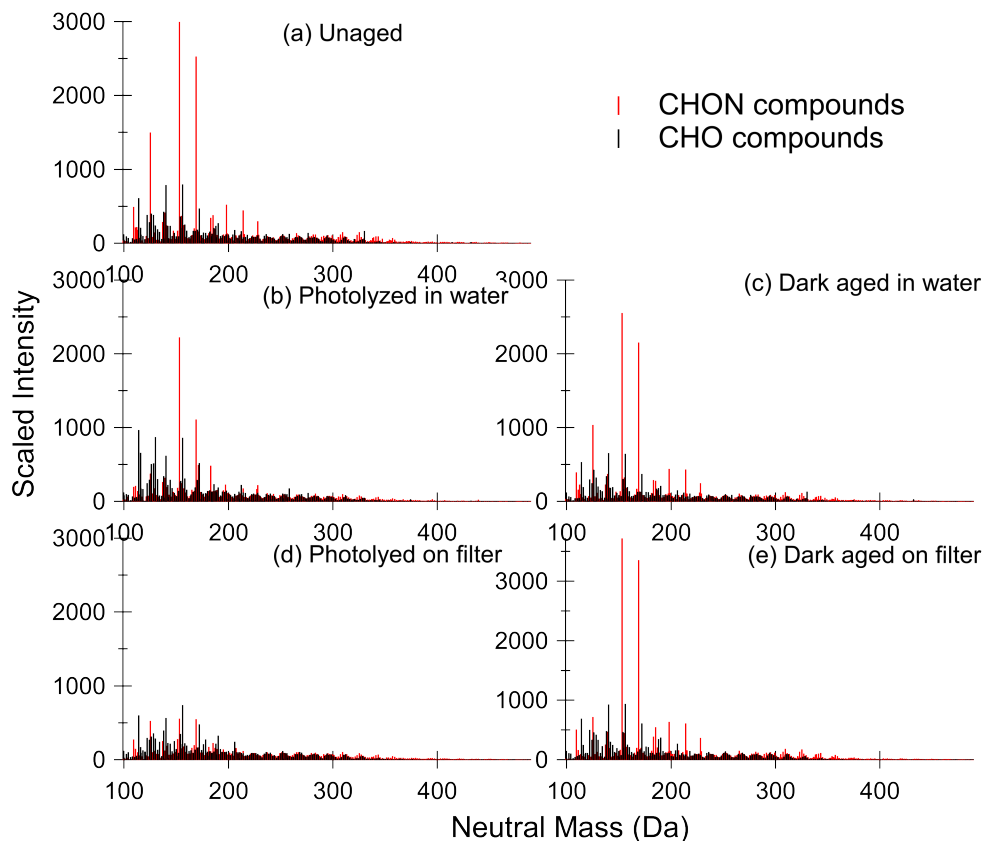


Figure 4.10: Mass spectra for all photolysis and dark aged samples comparing aging in water and on the filter. CHON compounds are shown in red and CHO compounds are shown in black.

A visual comparison of the highest peak intensities in the mass spectra in Figure 4.10(a) (unaged) and 4.10(b) (photolyzed in water) suggests that photolysis in water does not lead to a large change in the overall composition. There is some decrease in the abundance of nitrogen-containing compounds upon UV irradiation, but many of the major peaks are the same as in the unaged spectrum. Some formation of CHO compounds at lower molecular weights (less than 150 Da) can be seen. This is not observed in the dark-aged aqueous sample in 4.10(c). The peaks that are most different in abundance between the photolysis and dark samples (such that they are among the 10 most abundant peaks after photolysis but not after dark aging) are present at much greater abundances in the negative mode than in the positive mode and can be assigned to small organic acids, such as maleic acid at 116 Da. Organic acids are established aqueous photolysis products of nitrophenols.<sup>190</sup>

The difference in the composition after on-filter photolysis (Figure 4.10(d)) is much more apparent. In contrast to the aqueous photolysis condition (Figure 4.10(b)) where the nitrogen-containing peaks are relatively unaffected, the nitrogen-containing peaks in the organic-rich phase are greatly reduced in abundance with photolysis – such that the CHON compounds no longer dominate the mass spectrum. In contrast to the large reduction in CHON compounds, the CHO compound abundance appears relatively unchanged. We do not observe an increase in peak abundances at low molecular weights as we did with aqueous photolysis. This suggests the photolysis products may be different in the organic phase as compared to the aqueous phase. We should note that the aqueous photolysis products may remain dissolved in water after formation, while those from filter photolysis may more easily escape into the gas phase if they are formed on the surface of the SOA film.

The unaged samples and the results of aging in water appear reproducible when comparing the two separate experiments depicted in Figures 4.10 and 4.11 – little change is observed other than a modest increase in abundance of low molecular weight CHO compounds with photolysis in water. Further, the addition of 1 M ammonium sulfate (Figure 4.11(d)) did not have a significant impact on the composition after photolysis as compared to pure water (Figure 4.11(b)). There does appear to be less increase in low molecular weight CHO compounds, which is reasonable considering the photobleaching was about half as fast in the ammonium sulfate condition as in the pure water condition. We conclude that ammonium sulfate did not have a large effect on changes in SOA composition with photolysis as compared to pure water, but rather simply slowed down the photolysis rate.

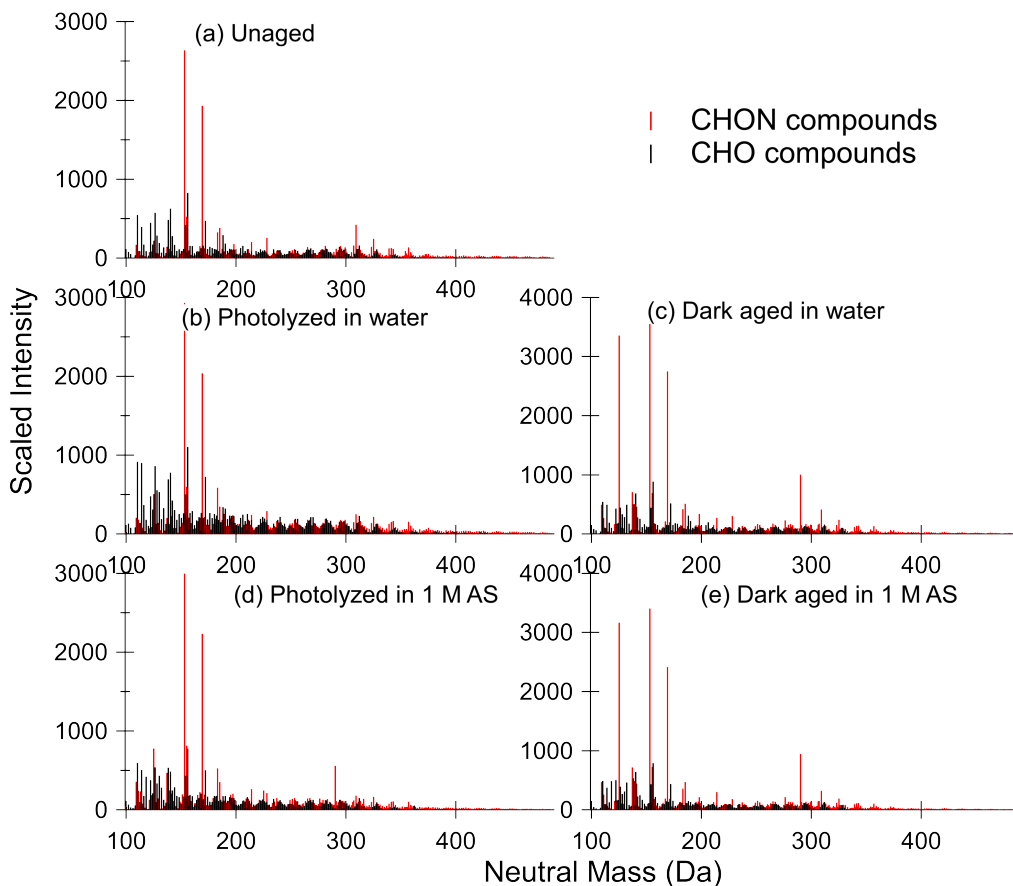


Figure 4.11: Mass spectra for all photolysis and dark aged samples comparing aging in water and 1 M ammonium sulfate. CHON compounds are shown in red and CHO compounds are shown in black.

Visualization methods such as the Van Krevelen diagram are useful in interpreting the large amount of data obtained from high-resolution mass spectrometry.<sup>191–193</sup> Van Krevelen diagrams for all experiments are shown in Figures 4.12 and 4.13. For these plots, compounds were sorted into groups of CHO (in black) and CHON (in red), and then H:C and O:C ratios were binned and summed so that each marker on the diagram represents the sum of all compounds with that H:C and O:C ratio, and marker size was scaled to this value. The discussion of the Van Krevelen diagrams presented here describes visually identified qualitative changes between conditions. We leave the quantitative discussions to the other techniques presented in this work. In the unaged SOA (Figures 4.12(a) and 4.13(a)), the markers are clustered around an O:C ratio of 0.5 and an H:C ratio of 1.0, which is typical of

oxidized aromatic hydrocarbons.<sup>192,194</sup> The largest markers in the unaged samples represent CHON compounds, with the most abundant summed CHO ratios being much less abundant. After photolysis in water in Figures 4.12(c) and 4.13(c), there was a modest reduction in the total abundance of compounds with CHON formulas and an increase in total abundance of compounds with CHO formulas. The ratios that increased in summed intensity generally had both higher H:C and O:C ratios than the ratios that decreased in summed abundance. There is little change observed after aging in the dark as seen in Figure 4.12(b). The shift in summed ratio abundance observed with photolysis in water was also observed for the sample aged in 1 M ammonium sulfate (Figure 4.13(d)), although to a lesser extent. Finally, after photolysis on the filter (Figure 4.12(d)), there was a dramatic reduction in the summed abundances of CHON compounds. Further, an increase in summed abundances of CHO compounds is not evident, demonstrating that changes in molecular composition with photolysis in water are very different from changes in molecular composition with photolysis on the filter.

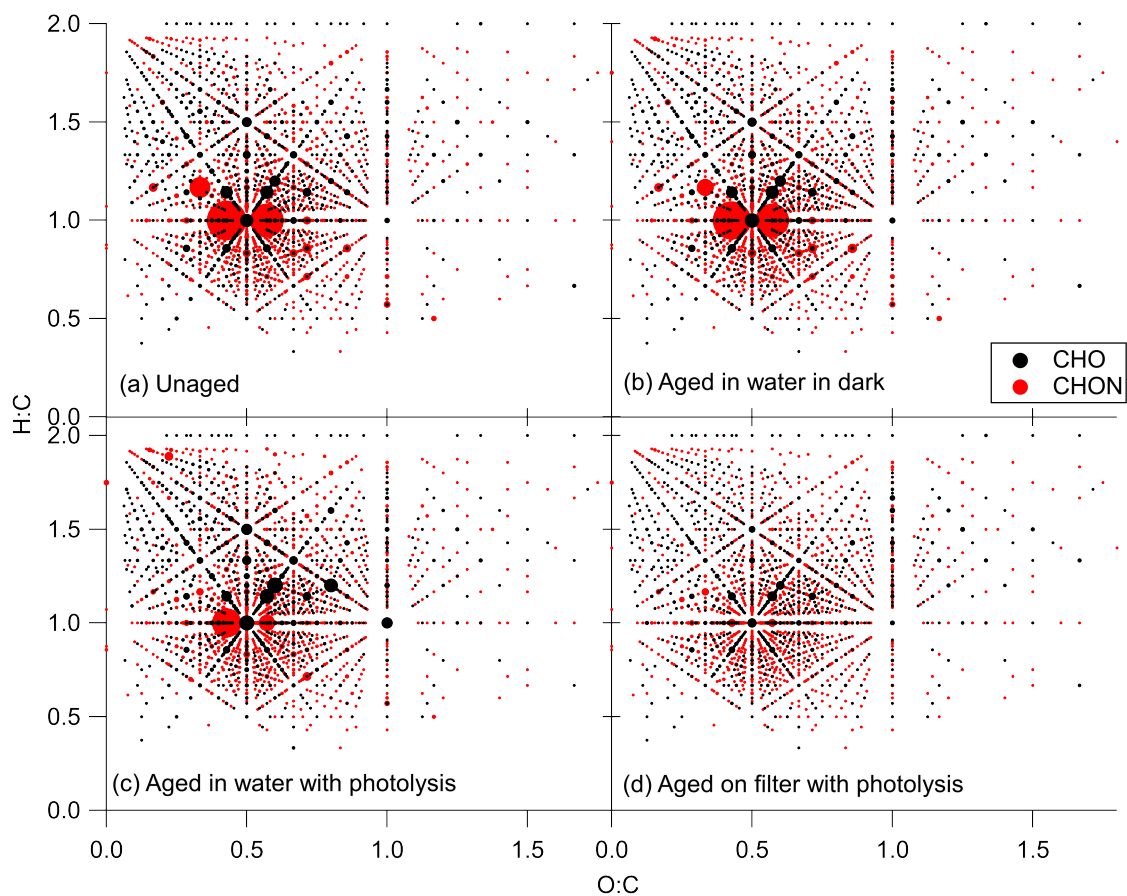


Figure 4.12: Van Krevelen diagrams for the (a) unaged sample, (b) sample aged in water in the dark, (c) sample photolyzed in water, and (d) sample photolyzed on the filter from Filter 3. CHO formulas are shown in black and CHON formulas are shown in red. The size of the marker represents the summed mass spectrometry abundance of all CHO or CHON compounds with the corresponding H:C and O:C ratios.



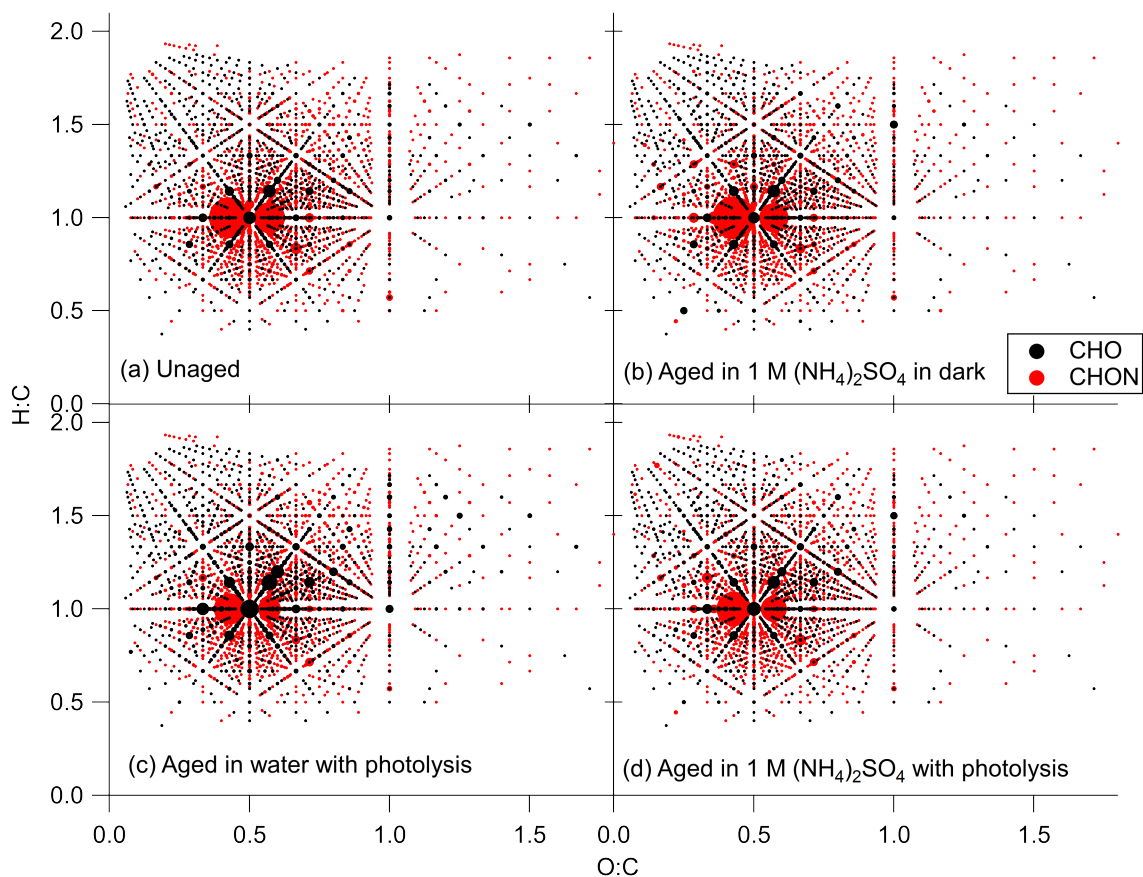


Figure 4.13: Van Krevelen diagrams for the (a) unaged sample, (b) sample aged in 1 M ammonium sulfate in the dark, (c) sample photolyzed in water, and (d) sample photolyzed in 1 M ammonium sulfate from Filter 4. CHO formulas are shown in black and CHON formulas are shown in red. The size of the marker represents the summed mass spectrometry abundance of all CHO or CHON compounds with the corresponding H:C and O:C ratios.

### 4.4.2.3 Changes in Nitrogen-Containing Groups with On-Filter Photolysis

To confirm the removal of nitrogen-containing compounds during on-filter photolysis, nitrogen content was quantified with offline-AMS data. The purpose of this analysis was to directly contrast the difference in composition changes with photolysis. Since we did not observe dramatic changes in chemical composition during the aging of toluene SOA between the water and 1 M ammonium sulfate conditions, and given the low concentrations of SOA mass on our sample filters, the 1 M ammonium sulfate conditions were excluded from this analysis. This allowed us to perform this analysis on a single filter split between the water and filter aging conditions, making the SOA composition of the two samples as identical as possible. Analysis was performed by normalizing the  $\text{NO}^+$  and  $\text{NO}_2^+$  signal to the labeled  $\text{NO}^+$  and  $\text{NO}_2^+$  signals from the internal standard as shown in Figure 4.14. The normalization accounts for variations in the signal for each nebulization pulse, which has been demonstrated to occur with the small volume nebulizer.<sup>187</sup> Organonitrates and organic nitro groups generate  $\text{NO}^+$  and  $\text{NO}_2^+$  when ionized in the AMS, thus differences in the total amount of these ions suggest a loss of these functional groups in the samples.<sup>195</sup> Before photolysis, the concentrations of nitrogen-containing compounds for the aqueous and on-filter samples are slightly outside of each other's standard deviations, which may be a result of small differences in the amount of labeled ammonium nitrate added to the solutions or a small variation in extraction efficiencies between the two filter halves. There is no apparent change in nitrogen content after 5 h of photolysis in pure water. In stark contrast, there is a reduction in nitrogen content after 5 h of photolysis directly on the filter. Inorganic nitrate groups may also contribute to the  $\text{NO}^+$  and  $\text{NO}_2^+$  signals. However, organic and inorganic nitrate fragment with different  $\text{NO}^+/\text{NO}_2^+$  fragment ratios,<sup>196,197</sup> with fragment ratios from ammonium nitrate being lower than fragment ratios from nitrogen-containing organic compounds. We calculated the  $\text{NO}^+/\text{NO}_2^+$  fragment ratios for our samples as well as for the isotopically labeled ammonium nitrate standard that was added to the samples, and these results are

shown in Figure 4.14(b) and 4.14(c). After photolysis, the  $\text{NO}^+/\text{NO}_2^+$  fragment ratios in both the aqueous and filter conditions decreased somewhat (Figure 4.14(b)), but not to the level of the  $\text{NO}^+/\text{NO}_2^+$  fragment ratios from the inorganic standard (Figure 4.14(c)). We, therefore, do not believe the resistance of the aqueous sample to losing nitrogen-containing peaks with photolysis is solely due to interference with inorganic nitrate, although the results here do suggest some change in the relative amounts of organic and possibly inorganic nitrogen-containing groups with photolysis.

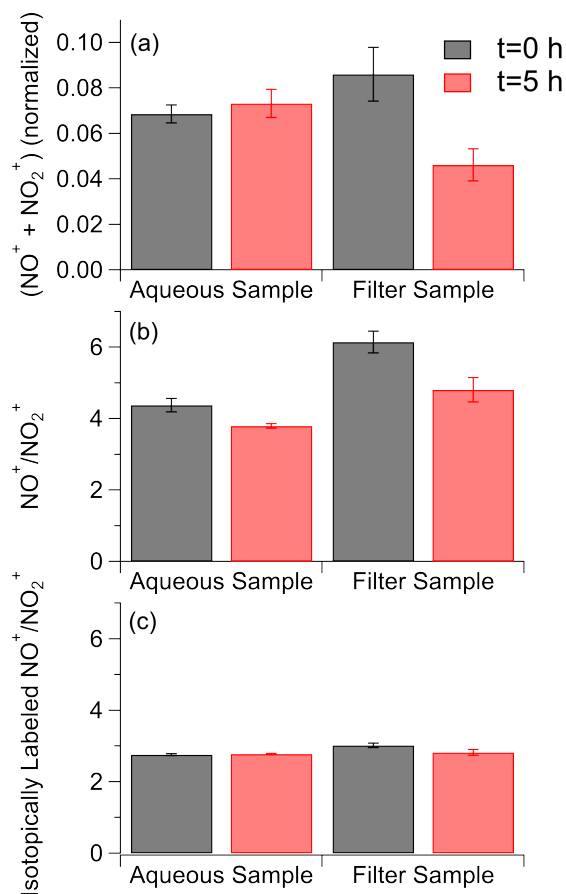


Figure 4.14: (a) Totals for the main fragment ions for nitrogen-containing groups measured by aerosol mass spectrometry before (in black) and after 5 h of photolysis (in red) in the aqueous phase and organic particle phase.  $\text{NO}^+$  and  $\text{NO}_2^+$  fragment concentrations are normalized to an internal standard. (b)  $\text{NO}^+/\text{NO}_2^+$  fragment ratios before (in black) and after 5 h of photolysis (in red) for samples age in water and on the filter. (c)  $\text{NO}^+/\text{NO}_2^+$  fragment ratios for the isotopically labeled inorganic internal standard. Error bars represent one standard deviation over five injections.

Figure 4.15 shows the evolution of the FTIR spectra of the toluene SOA during on-filter photolysis. The aqueous conditions were too dilute for FTIR analysis, so they are not included in this method. Absorbance values are normalized to the peak intensity at 1717  $\text{cm}^{-1}$ , which represents the carbonyl group stretching vibration. We expect carbonyl groups belonging to ketone and aldehyde functionalities to be removed through Norrish-I type reactions with photolysis.<sup>72,136</sup> Peaks that decrease in this plot, therefore, photolyze more readily than carbonyl compounds. Peaks corresponding to nitroaromatics ( $\text{Ar-NO}_2$ ) and organonitrates ( $\text{RONO}_2$ ) are denoted in the figure.<sup>198-200</sup> It can be observed that the peaks at 1643, 1275, and 850  $\text{cm}^{-1}$  corresponding to organonitrates decrease relative to the carbonyl peak over time. Peaks at 1556, 1539, 1360, and 1337  $\text{cm}^{-1}$  corresponding to nitroaromatics also decrease relative to the carbonyl peak, although they do so less efficiently than the organonitrate peaks. This suggests the nitroaromatic compounds may photolyze at a slower rate than organonitrate compounds. These experiments were carried out at WM using a different lamp, so the timescales are not directly comparable with the kinetic measurements. Overall, the FTIR results show that nitrogen-containing compounds are removed during photolysis of the filters in the organic condensed phase, consistent with the HRMS results.

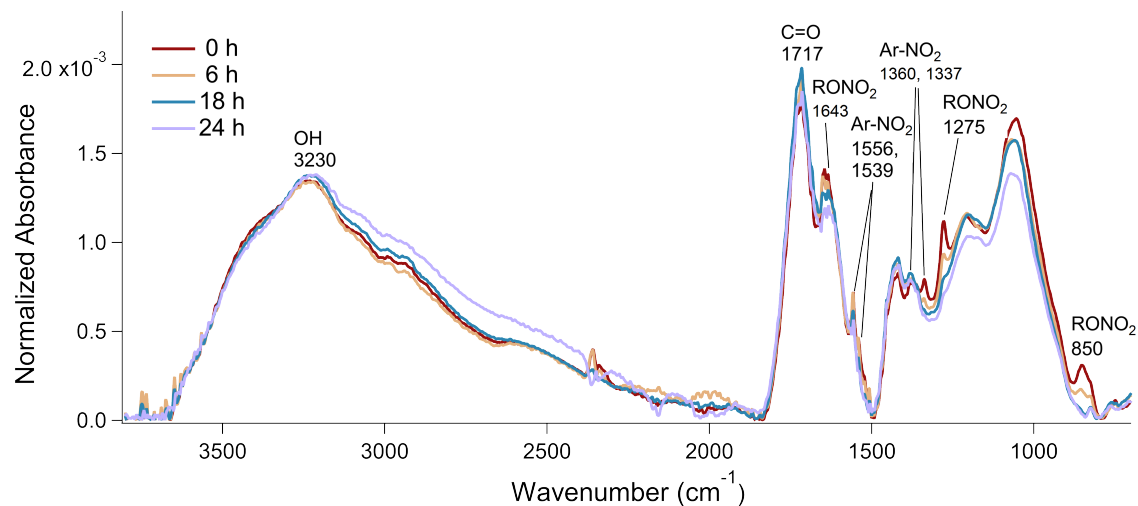


Figure 4.15: ATR-FTIR spectra taken after different times of on-filter photolysis normalized to the highest peak in each spectrum – the C=O peak at  $1717\text{ cm}^{-1}$  from Filter 2. The trace for before photolysis is shown in dark red, after 6 h of photolysis in yellow, after 18 h in teal, and after 24 h in light blue. The photolysis for this experiment was performed with the irradiation set up at WM.

The removal of nitrogen-containing compounds from the on-filter samples suggests that the nitrogen-containing groups present in the SOA are being converted to gas-phase products that volatilize from the filter. Indeed, photolysis of gaseous ortho-nitrophenols was shown to produce HONO (although there was significant disagreement on the HONO quantum yield).<sup>201,202</sup> Photolysis of para-nitrophenols in solutions, including viscous solutions containing organic solutes, has also been shown to produce HONO/NO<sub>2</sub><sup>-</sup>.<sup>203</sup> It is likely that HONO/NO<sub>2</sub><sup>-</sup> production is suppressed in a condensed-phase environment by excitation quenching. The extent of this suppression could be stronger under aqueous conditions compared to an organic matrix, resulting in slower removal of nitrogen from the photolyzed aqueous sample. In addition, HONO would more easily volatilize from the filter than from an aqueous solution further reducing the AMS signal from nitrogen compounds in on-filter photolysis experiments.

#### 4.4.2.4 Effect of Photolysis Matrix on the Photo-degradation Mechanism

It is clear from the UPLC-PDA-HRMS data that the photolysis of toluene SOA proceeds differently in the viscous organic phase compared to the aqueous phase, and here we aim to propose plausible explanations for our observed experimental results based on previous studies. Our experiments show that nitrophenols, which are mostly resolved in the PDA data and are expected to be major chromophores in this SOA, are preferentially photolyzed in the viscous organic phase. Previous studies have established that nitrophenols photolyze more quickly in the organic phase than in the aqueous phase, and the proposed mechanism is the abstraction of a hydrogen atom from surrounding organic molecules by a triplet state of an excited nitrophenol.<sup>78,81</sup> For 3-nitropyrene, hydrogen abstraction was observed to be nearly diffusion controlled, while charge transfer reactions were not observed in organic solvents.<sup>204</sup> Further, it was observed that phenolic hydrogens were most efficiently abstracted by the triplet excited states of nitro-polycyclic aromatic hydrocarbons (PAH), with other types of easily-abstractable hydrogens not participating in photodegradation.<sup>205</sup> We expect a significant fraction of phenolic compounds in our SOA, and in the organic phase an excited triplet state will be in closer proximity to abstractable phenolic hydrogens than in the aqueous phase, making this a plausible explanation for relatively fast removal of CHON compounds in the organic phase. Additionally, oxy-PAHs with an  $n$  to  $\pi^*$  triplet character have been shown to strongly accelerate nitro-PAH decay through the initiation of a radical chain reaction.<sup>205</sup> This pathway is more important in the organic phase than in the aqueous phase because differences in matrix polarity change the relative energies of the  $n$  to  $\pi^*$  and  $\pi$  to  $\pi^*$  transitions for many aromatic carbonyls, such that the more reactive  $n$  to  $\pi^*$  transition is favored in less polar matrices and the less reactive  $\pi$  to  $\pi^*$  transition is favored in polar matrices.<sup>206</sup> These mechanisms in combination likely explain the relatively rapid loss of nitrophenols in the organic phase as observed by mass spectrometry.

In spite of slower photodegradation of nitrophenols (assessed via HRMS, offline-AMS, and FTIR analyses), the overall photobleaching (assessed via UV-Vis analyses) was actually faster in the aqueous phase as compared to on-filter photodegradation. Since we observed minimal composition change with mass spectrometry, photolysis in the aqueous phase must result in the decay of highly absorbing compounds with low relative abundance or poor electrospray ionization efficiency. This observation correlates well to the observations in Lin et al.,<sup>176</sup> which catalogued the chromophores in toluene SOA, and attributed 40 to 60% of the PDA absorbance to poorly separated chromophores with low peak abundances in ESI mass spectra.<sup>176</sup> Additionally, this may agree with the larger decrease in the unresolved baseline feature observed in our aqueous PDA samples (-35% and -45% for the pure water and ammonium sulfate conditions, respectively) as compared to our on-filter PDA samples (-21%). The chromophores which are being photolyzed in the aqueous conditions contribute strongly to the sample absorbance, but not necessarily to the mass spectrum. Further, the fact that photobleaching is slowed with the addition of ammonium sulfate suggests that these lower abundance compounds may still react through a triplet state when photolyzed. Ionic species may quench an excited triplet compound before it reacts,<sup>207</sup> leading to slower chromophore loss with the addition of ammonium sulfate.

There is also a possible role of reactions between aqueous ammonia and carbonyl compounds in SOA, which are known to cause browning through the formation of imine-type chromophores.<sup>25</sup> While these reactions were shown to contribute to only a modest change in the MAC of high-NO<sub>x</sub> SOA from aromatic hydrocarbon precursors,<sup>141</sup> and the nitrogen-containing products formed through these processes tend to have short photolysis lifetimes,<sup>40</sup> aqueous photolysis reactions would lead to continuous formation of these small carbonyl compounds and potentially continuous formation of these imine-type chromophores.<sup>208</sup> We do see a peak slowly forming at about 300 nm in the dark with ammonium sulfate, which has a similar peak position to that previously observed for trimethylbenzene high-NO<sub>x</sub> SOA

aged with ammonium.<sup>141</sup> Unfortunately, it is hard to directly observe these compounds by our mass spectrometry methods,<sup>157</sup> because they have been shown to hydrolyze in the mass spectrometry solvent.<sup>209</sup> Therefore, we suggest that reaction of carbonyls with dissolved ammonia plays only a secondary role in the photochemistry of aqueous toluene SOA in presence of ammonium sulfate.

## 4.5 Conclusions/Atmospheric Implications

Toluene high-NO<sub>x</sub> SOA was aged by direct photolysis on filters simulating the viscous organic phase in aerosol particles and in aqueous solution with and without 1 M ammonium sulfate representing dilute atmospheric cloud water and concentrated aerosol-phase water, respectively. UV-Vis measurements reported here show that photobleaching is fastest in pure water, while the presence of ammonium sulfate modestly slows the rates of photobleaching. Photobleaching in the viscous organic phase is much slower and likely results in the formation of photorecalcitrant compounds. Chromatographic analysis showed that nitrophenols, as well as a large number of unresolved chromophores, contribute to the absorption coefficient of this type of SOA. We find that the decay of nitrophenol compounds proceeds more quickly in the viscous organic phase than in the aqueous phase, in agreement with previous studies measuring the photolysis of single nitrophenols in aqueous solutions and in viscous organics.<sup>81</sup> In contrast, the SOA composition of the aqueous phase samples does not change appreciably over the 5 h photolysis experiment in spite of the observed faster overall photobleaching (assessed by UV-Vis analysis). This suggests preferential photodegradation of unidentified chromophores with high absorptivity but low peak abundance in the mass spectra.

Based on previous studies, we propose that the differences in photolytic aging may be ex-



plained by differences in triplet state reactivity between sample matrices. Previous work has observed different photolysis rates for the same chromophore in different atmospherically-relevant environments, such as water, alcohol solutions, and glassy organic matrices.<sup>78–81</sup> These studies mostly focused on the photolysis of select nitrophenol compounds and found nitrophenols to photolyze faster in the organic solvents than in water. Our results confirm that SOA nitrophenols, as a group, appear to be the more efficiently photolyzed chromophores in the organic phase. However, this cannot be generalized to all chromophores because we observe that other, presently unidentified, chromophores are more efficiently photolyzed in aqueous solution. Therefore, generally speaking, photolysis rates of individual major chromophores can be quite different from the overall photobleaching rates, particularly when measured in the aqueous phase, and the study of individual chromophores does not fully represent the behavior of complex SOA particles.

Reaction with the OH radical is considered the most important sink for organic molecules in the atmosphere. In the case of SOA, biomass burning organic aerosol, and individual nitrophenol compounds, OH reactions are often observed to cause chromophore formation for a short time period before leading to overall photobleaching for both heterogeneous reactions on particles and reactions in the aqueous phase.<sup>40</sup> Subsequent photobleaching of various BrC aerosol types has a wide variety of OH lifetimes ranging from hours to days,<sup>40</sup> which is of the same order we measure for our UV-irradiation experiments. Nitrophenols react relatively quickly with OH in the aqueous phase – lifetimes of several hours have been reported for a few representative compounds – so OH will likely be a more important sink for nitrophenols in clouds and aqueous aerosol.<sup>210,211</sup> However, since we observe that photobleaching occurs much more quickly than nitrophenol loss in the aqueous phase, we can expect both OH reaction and photodegradation to be important factors affecting the lifetimes of individual chromophores in the atmosphere. The results reported here will likely vary depending on ionic strength or particle viscosity. The ammonium sulfate concentration used here – 1

M – is on the low end of ionic strengths found in atmospheric particles.<sup>49</sup> If our proposed explanation is correct, higher salt concentrations will likely quench triplet reactivity more efficiently and so may slow photodegradation further. Additionally, higher ammonium concentrations may also lead to faster formation of imine-based chromophores. Future work is needed to determine the precise relationship between the ionic strength and photobleaching rate for different types of SOA. Furthermore, this study was limited to ammonium sulfate, but other anions, such as halides, are more effective triplet quenchers than sulfate.<sup>212,213</sup> More importantly, more work on the impact of the matrix viscosity on photodegradation of SOA should be done. Previous studies have found higher viscosity to sometimes slow down and sometimes accelerate photodegradation of individual nitroaromatics.<sup>79,81</sup> The conflicting results are likely due to the specific reactivity of nearby molecules during photolysis as well as triplet lifetime of the absorber. Therefore, it will be useful to independently vary the organic matrix viscosity and the types of surrounding species in future studies in order to fully understand the factors controlling photobleaching and photodegradation lifetimes of SOA. Further work is needed to confirm the underlying mechanism causing the differences in photodegradation and photobleaching rates observed here and in previous studies.

# Chapter 5

## Conclusions

This thesis demonstrates that the aging processes of organic compounds commonly found in atmospheric aerosol particles will vary based on the surrounding matrix of the medium (aqueous aerosol, organic aerosol, or cloud/fog droplet) where the aerosol particle constituents age. This was demonstrated by examining how these compounds change during aging in dilute aqueous solutions representing cloud water, high ionic strength solutions representing deliquesced aerosols, and a viscous organic medium representing organic aerosol particles with low liquid water content. Changes in the composition and optical properties of the organic compounds were observed, showing that both inorganic ions and highly viscous organic matrices influence their photochemical and dark processing occurring in the atmosphere.

In Chapter 2, the influence of ammonium salts on the decarboxylation of oxaloacetic acid (OAA) was observed. While it was concluded that the lifetime of OAA will be strongly dependent on the aqueous system in which the decarboxylation occurs, with pH having the strongest effect followed by the ammonium concentration, decarboxylation will likely be more important than OH oxidation under most atmospheric conditions. Decarboxylation will also likely be more important than other possible reactions that have been measured for small

carbonyl compounds such as aldol condensation. These results explain why this compound is not frequently observed in field studies despite the abundance of its atmospheric precursors and frequent observation in laboratory studies.

In future work, the results from Chapter 2 should be expanded to other 3-oxocarboxylic acids as decarboxylation will occur in this entire class of molecules, although other molecules will like have different reactivity than OAA. The decarboxylation rates of 3-oxocarboxylic acids, such as acetoacetic acid and  $\alpha,\alpha$ -dimethylacetoacetic acid, are thought to be similar in magnitude to OAA's decarboxylation rate in pure water,<sup>132,133</sup> but the changes in decarboxylation rates with ammonium salts have not been determined. Further, the OH reactivity of other 3-oxocarboxylic acids will differ from OAA as a result of structural differences and types of hydrogen atoms that are available for abstraction by the OH radical. The relative importance of OH oxidation and decarboxylation for other 3-oxocarboxylic acids and how the structure of these molecules affects the ammonium-catalyzed decarboxylation should be determined. Additionally, transition metals have been observed to catalyze the decarboxylation of oxaloacetic acid,<sup>214</sup> which may become important in areas affected by sea spray aerosol,<sup>215</sup> so this could be an additional avenue for future experiments.

The effect of low concentrations of hydrogen peroxide and nitrate salts, common atmospheric solutes, on the aqueous-phase aging of SOA was discussed in Chapter 3. These conditions represent cloud and fog water, which are known to be important media for SOA formation and aging.<sup>51</sup> Even without photolysis, the presence of nitrate ions was observed to reduce the abundance of higher-molecular-weight compounds in  $\alpha$ -pinene SOA particle extracts but not in  $\alpha$ -humulene SOA particle extracts, suggesting an increased rate of loss of dimeric species at low nitrate concentrations. The results from this study have implications for the role of salts in the aging of SOA dissolved in cloud and fog water. The results presented in Chapter 3 will be particularly important in urban areas, where anthropogenic sources con-

tribute high levels of  $\text{NO}_x$ , leading to significant amounts of  $\text{NO}_3^-$  in the atmospheric waters.

The effect of nitrate ions observed here is unusual, and future work should be conducted to identify the structural motifs of the dimers that decay with the addition of nitrate ions as well as the mechanism for the observed effect. At the time of the study, we assumed that nitrate catalyzes the hydrolysis of ester linkages in dimer species in SOA. A recent publication synthesized an ester-dimer commonly produced in  $\alpha$ -pinene oxidation,<sup>216</sup> and the first author of this study examined hydrolysis of this molecule and found it to be stable (informal communication with Christopher Kenseth during a poster discussion). Additionally, it should be ascertained if this effect is also observed in the particle phase, where concentrations of inorganics, and therefore nitrate, are many orders of magnitude higher than in cloud and fog water.<sup>49</sup>

Chapter 4 investigated the differences in the photodegradation of toluene high- $\text{NO}_x$  SOA in various atmospheric matrices. It was concluded that nitrophenol-type compounds, which are the most abundant chromophores in toluene high- $\text{NO}_x$  SOA, photodegrade most efficiently in the organic phase, while the overall photobleaching of the SOA was fastest in the aqueous phase. This suggests that the photodegradation behavior of individual chromophores does not always predict the photobleaching behavior of a complex SOA particle. The results of Chapter 4 suggest it is important to look at the photobleaching rates of complex aerosol particles, rather than only major chromophores, to understand the photobleaching rates of particles in the atmosphere. Additionally, it was shown that rates and mechanisms measured under dilute aqueous conditions will not necessarily be applicable to high-ionic strength solutions or viscous organic solutions.

There are several opportunities for future work stemming from Chapter 4. First, the results for the ammonium sulfate-containing conditions will likely vary depending on ionic

strength. This study used a fixed value of ammonium sulfate concentration (1 M), a relatively low ionic strength compared to the range of conditions observed in atmospheric particles.<sup>49</sup> Higher salt concentrations may quench triplet reactivity more efficiently and slow photodegradation further than observed here. Additionally, phase separation can occur at very high salt concentrations, with potentially important chemistry occurring at the interface between the two phases. Mechanisms other than triplet quenching may become important at higher ammonium concentrations, such as the formation of imine-based chromophores which could in fact lead to the browning of SOA.<sup>25</sup> Additionally, this study only observed the effects of ammonium sulfate, but other anions are more effective triplet quenchers than sulfate.<sup>212,213</sup> With that being said, future work on the effect of the matrix viscosity on the photodegradation of SOA should be prioritized compared to studying the effects of ionic strength, as much less information is available about this topic. It will be important to independently vary the viscosity of the organic matrix and the types of surrounding species to parse the different effects of these two factors. This is particularly important because previous studies have found increased viscosity to both accelerate and slow photodegradation of nitrophenols,<sup>81,178</sup> and the reason for the discrepancy should be explored.

In conclusion, the aging chemistry of atmospheric particles changes based on the medium in which the aging occurs. The topics and methods presented in this dissertation only began to explore various conditions an aerosol organic molecule might experience during its atmospheric lifetime, and are in fact highly simplified compared to atmospheric conditions. Therefore, more work needs to be done to understand the influence of the types of molecular environment found in realistic atmospheric particles on reactions of both individual compounds and complex mixtures of SOA compounds leading to their atmospheric aging.

# References

- (1) Hallquist, M. et al. The formation, properties and impact of secondary organic aerosol: current and emerging issues. *Atmos. Chem. Phys.* **2009**, *9*, 5155–5236.
- (2) Pöschl, U. Atmospheric aerosols: Composition, transformation, climate and health effects. *Angew. Chemie Int. Ed.* **2005**, *44*, 7520–7540.
- (3) George, C.; Ammann, M.; D’Anna, B.; Donaldson, D. J.; Nizkorodov, S. A. Heterogeneous photochemistry in the atmosphere. *Chem. Rev.* **2015**, *115*, 4218–4258.
- (4) Kanakidou, M. et al. Organic aerosol and global climate modelling: a review. *Atmos. Chem. Phys.* **2005**, *5*, 1053–1123.
- (5) Hodzic, A.; Kasibhatla, P. S.; Jo, D. S.; Cappa, C. D.; Jimenez, J. L.; Madronich, S.; Park, R. J. Rethinking the global secondary organic aerosol (SOA) budget: Stronger production, faster removal, shorter lifetime. *Atmos. Chem. Phys.* **2016**, *16*, 7917–7941.
- (6) Lim, H. J.; Turpin, B. J. Origins of primary and secondary organic aerosol in Atlanta: Results of time-resolved measurements during the Atlanta Supersite Experiment. *Environ. Sci. Technol.* **2002**, *36*, 4489–4496.
- (7) Finlayson-Pitts, B. J.; Pitts, J. N., *Chemistry of the upper and lower atmosphere : theory, experiments, and applications*; Academic Press: 2000, p 969.
- (8) Lee Ng, N. et al. Nitrate radicals and biogenic volatile organic compounds: Oxidation, mechanisms, and organic aerosol. *Atmos. Chem. Phys.* **2017**, *17*, 2103–2162.
- (9) M. F. Barreira, L.; Helin, A.; Aurela, M.; Teinila, K.; Friman, M.; Kangas, L.; V. Niemi, J.; Portin, H.; Kousa, A.; Pirjola, L.; Ronkko, T.; Saarikoski, S.; Timonen, H. In-depth characterization of submicron particulate matter inter-annual variations at a street canyon site in northern Europe. *Atmos. Chem. Phys.* **2021**, *21*, 6297–6314.
- (10) Atkinson, R.; Arey, J. Atmospheric degradation of volatile organic compounds. *Chem. Rev.* **2003**, *103*, 4605–4638.
- (11) Bouvier-Brown, N. C.; Goldstein, A. H.; Gilman, J. B.; Kuster, W. C.; De Gouw, J. A. In-situ ambient quantification of monoterpenes, sesquiterpenes and related oxygenated compounds during BEARPEX 2007: Implications for gas- and particle-phase chemistry. *Atmos. Chem. Phys.* **2009**, *9*, 5505–5518.

- (12) Calvert, J. G.; Atkinson, R.; Becker, K.; Kamens, R.; Seinfeld, J.; Wallington, T.; Yarwood, G., *The Mechanisms of Atmospheric Oxidation of Aromatic Hydrocarbons*; Oxford University Press: New York, 2002, p 556.
- (13) Kroll, J. H.; Seinfeld, J. H. Chemistry of secondary organic aerosol: Formation and evolution of low-volatility organics in the atmosphere. *Atmos. Environ.* **2008**, *42*, 3593–3624.
- (14) Zhang, H. et al. Monoterpenes are the largest source of summertime organic aerosol in the southeastern United States. *Proc. Natl. Acad. Sci. U. S. A.* **2018**, *115*, 2038–2043.
- (15) Guenther, A. et al. A global model of natural volatile organic compound emissions. *J. Geophys. Res.* **1995**, *100*, 8873–8892.
- (16) Kansal, A. Sources and reactivity of NMHCs and VOCs in the atmosphere: A review. *J. Hazard. Mater.* **2009**, *166*, 17–26.
- (17) Chan, A. W.; Kautzman, K. E.; Chhabra, P. S.; Surratt, J. D.; Chan, M. N.; Crouse, J. D.; Kürten, A.; Wennberg, P. O.; Flagan, R. C.; Seinfeld, J. H. Secondary organic aerosol formation from photooxidation of naphthalene and alkylnaphthalenes: Implications for oxidation of intermediate volatility organic compounds (IVOCs). *Atmos. Chem. Phys.* **2009**, *9*, 3049–3060.
- (18) Lenner, M. Nitrogen dioxide in exhaust emissions from motor vehicles. *Atmos. Environ.* **1987**, *21*, 37–43.
- (19) Saxena, P.; Hildemann, L. M. Water-soluble organics in atmospheric particles: A critical review of the literature and application of thermodynamics to identify candidate compounds. *J. Atmos. Chem.* **1996**, *24*, 57–109.
- (20) Reid, J. P.; Bertram, A. K.; Topping, D. O.; Laskin, A.; Martin, S. T.; Petters, M. D.; Pope, F. D.; Rovelli, G. The viscosity of atmospherically relevant organic particles. *Nat. Commun.* **2018**, *9*, 1–14.
- (21) Smith, N. R.; Crescenzo, G. V.; Huang, Y.; Hettiyadura, A. P.; Siemens, K.; Li, Y.; Faiola, C. L.; Laskin, A.; Shiraiwa, M.; Bertram, A. K.; Nizkorodov, S. A. Viscosity and liquid–liquid phase separation in healthy and stressed plant SOA. *Environ. Sci. Atmos.* **2021**, *1*, 140–153.
- (22) Liu, P.; Song, M.; Zhao, T.; Gunthe, S. S.; Ham, S.; He, Y.; Qin, Y. M.; Gong, Z.; Amorim, J. C.; Bertram, A. K.; Martin, S. T. Resolving the mechanisms of hygroscopic growth and cloud condensation nuclei activity for organic particulate matter. *Nat. Commun.* **2018**, *9*, 1–10.
- (23) Davies, J. F.; Zuend, A.; Wilson, K. R. Technical note: The role of evolving surface tension in the formation of cloud droplets. *Atmos. Chem. Phys.* **2019**, *19*, 2933–2946.
- (24) Ovadnevaite, J.; Zuend, A.; Laaksonen, A.; Sanchez, K. J.; Roberts, G.; Ceburnis, D.; Decesari, S.; Rinaldi, M.; Hodas, N.; Facchini, M. C.; Seinfeld, J. H.; O’Dowd, C. Surface tension prevails over solute effect in organic-influenced cloud droplet activation. *Nature* **2017**, *546*, 637–641.



- (25) Laskin, A.; Laskin, J.; Nizkorodov, S. A. Chemistry of atmospheric brown carbon. *Chem. Rev.* **2015**, *115*, 4335–4382.
- (26) Bohren, C. F.; Huffman, D. R., *Absorption and Scattering of Light by Small Particles*; Wiley: 1998.
- (27) Ångström, A. On the atmospheric transmission of sun radiation and on dust in the air. *Geogr. Ann.* **1929**, *11*, 156.
- (28) Masson-Delmotte, V. et al., *Climate Change 2021: The Physical Science Basis. Contribution of Working group I to the Sixth Assessment Report of the Intergovernmental Panel on Climate Change*; Cambridge University Press: 2021.
- (29) Tsigaridis, K. et al. The AeroCom evaluation and intercomparison of organic aerosol in global models. *Atmos. Chem. Phys.* **2014**, *14*, 10845–10895.
- (30) Robinson, A. L.; Donahue, N. M.; Shrivastava, M. K.; Weitkamp, E. A.; Sage, A. M.; Grieshop, A. P.; Lane, T. E.; Pierce, J. R.; Pandis, S. N. Rethinking organic aerosols: Semivolatile emissions and photochemical aging. *Science* **2007**, *315*, 1259–1262.
- (31) Carrico, C. M.; Petters, M. D.; Kreidenweis, S. M.; Sullivan, A. P.; McMeeking, G. R.; Levin, E. J.; Engling, G.; Malm, W. C.; Collett, J. L. Water uptake and chemical composition of fresh aerosols generated in open burning of biomass. *Atmos. Chem. Phys.* **2010**, *10*, 5165–5178.
- (32) Mikhailov, E.; Vlasenko, S.; Martin, S. T.; Koop, T.; Pöschl, U. Amorphous and crystalline aerosol particles interacting with water vapor: Conceptual framework and experimental evidence for restructuring, phase transitions and kinetic limitations. *Atmos. Chem. Phys.* **2009**, *9*, 9491–9522.
- (33) Odum, J. R.; Hoffman, T.; Bowman, F.; Collins, D.; Flagan, R. C.; Seinfeld, J. H. Gas/particle partitioning and secondary organic aerosol yields. *Environ. Sci. Technol.* **1996**, *30*, 2580–2585.
- (34) Darer, A. I.; Cole-Filipiak, N. C.; O’Connor, A. E.; Elrod, M. J. Formation and stability of atmospherically relevant isoprene-derived organosulfates and organonitrates. *Environ. Sci. Technol.* **2011**, *45*, 1895–1902.
- (35) Hu, K. S.; Darer, A. I.; Elrod, M. J. Thermodynamics and kinetics of the hydrolysis of atmospherically relevant organonitrates and organosulfates. *Atmos. Chem. Phys.* **2011**, *11*, 8307–8320.
- (36) Al-Abadleh, H. A. Review of the bulk and surface chemistry of iron in atmospherically relevant systems containing humic-like substances. *RSC Adv.* **2015**, *5*, 45785–45811.
- (37) Häkkinen, S. A. K.; McNeill, V. F.; Riipinen, I. Effect of inorganic salts on the volatility of organic acids. *Environ. Sci. Technol.* **2014**, *48*, 13718–26.
- (38) Wang, B.; O’Brien, R. E.; Kelly, S. T.; Shilling, J. E.; Moffet, R. C.; Gilles, M. K.; Laskin, A. Reactivity of liquid and semisolid secondary organic carbon with chloride and nitrate in atmospheric aerosols. *J. Phys. Chem. A* **2015**, *119*, 4498–4508.
- (39) Aljawhary, D.; Zhao, R.; Lee, A. K.; Wang, C.; Abbatt, J. P. Kinetics, mechanism, and secondary organic aerosol yield of aqueous phase photo-oxidation of  $\alpha$ -pinene oxidation products. *J. Phys. Chem. A* **2016**, *120*, 1395–1407.

- (40) Hems, R. F.; Schnitzler, E. G.; Liu-Kang, C.; Cappa, C. D.; Abbatt, J. P. Aging of atmospheric brown carbon aerosol. *ACS Earth Sp. Chem.* **2021**, *5*, 722–748.
- (41) Henry, K. M.; Donahue, N. M. Photochemical aging of  $\alpha$ -pinene secondary organic aerosol: Effects of OH radical sources and photolysis. *J. Phys. Chem. A* **2012**, *116*, 5932–5940.
- (42) Hung, H. M.; Chen, Y. Q.; Martin, S. T. Reactive aging of films of secondary organic material studied by infrared spectroscopy. *J. Phys. Chem. A* **2013**, *117*, 108–116.
- (43) Epstein, S. A.; Blair, S. L.; Nizkorodov, S. A. Direct photolysis of  $\alpha$ -pinene ozonolysis secondary organic aerosol: Effect on particle mass and peroxide content. *Environ. Sci. Technol.* **2014**, *48*, 11251–11258.
- (44) Hodzic, A.; Madronich, S.; Kasibhatla, P. S.; Tyndall, G.; Aumont, B.; Jimenez, J. L.; Lee-Taylor, J.; Orlando, J. Organic photolysis reactions in tropospheric aerosols: Effect on secondary organic aerosol formation and lifetime. *Atmos. Chem. Phys.* **2015**, *15*, 9253–9269.
- (45) Badali, K. M.; Zhou, S.; Aljawhary, D.; Antiñolo, M.; Chen, W. J.; Lok, A.; Mungall, E.; Wong, J. P.; Zhao, R.; Abbatt, J. P. Formation of hydroxyl radicals from photolysis of secondary organic aerosol material. *Atmos. Chem. Phys.* **2015**, *15*, 7831–7840.
- (46) Wong, J. P.; Zhou, S.; Abbatt, J. P. Changes in secondary organic aerosol composition and mass due to photolysis: Relative humidity dependence. *J. Phys. Chem. A* **2015**, *119*, 4309–4316.
- (47) Pruppacher, H. R.; Jaenicke, R. The processing of water vapor and aerosols by atmospheric clouds, a global estimate. *Atmos. Res.* **1995**, *38*, 283–295.
- (48) Herckes, P.; Valsaraj, K. T.; Collett, J. L. A review of observations of organic matter in fogs and clouds: Origin, processing and fate. *Atmos. Res.* **2013**, *132-133*, 434–449.
- (49) Herrmann, H.; Schaefer, T.; Tilgner, A.; Styler, S. A.; Weller, C.; Teich, M.; Otto, T. Tropospheric aqueous-phase chemistry: Kinetics, mechanisms, and its coupling to a changing gas phase. *Chem. Rev.* **2015**, *115*, 4259–4334.
- (50) Bikkina, S.; Kawamura, K.; Sarin, M. Secondary organic aerosol formation over coastal ocean: Inferences from atmospheric water-soluble low molecular weight organic compounds. *Environ. Sci. Technol.* **2017**, *51*, 4347–4357.
- (51) McNeill, V. F. Aqueous organic chemistry in the atmosphere: Sources and chemical processing of organic aerosols. *Environ. Sci. Technol.* **2015**, *49*, 1237–1244.
- (52) Ervens, B.; Volkamer, R. Glyoxal processing by aerosol multiphase chemistry: Towards a kinetic modeling framework of secondary organic aerosol formation in aqueous particles. *Atmos. Chem. Phys.* **2010**, *10*, 8219–8244.
- (53) Ng, N. L. et al. Organic aerosol components observed in Northern Hemispheric datasets from Aerosol Mass Spectrometry. *Atmos. Chem. Phys.* **2010**, *10*, 4625–4641.

- (54) Lim, H. J.; Carlton, A. G.; Turpin, B. J. Isoprene forms secondary organic aerosol through cloud processing: Model simulations. *Environ. Sci. Technol.* **2005**, *39*, 4441–4446.
- (55) Carlton, A. G.; Wiedinmyer, C.; Kroll, J. H. A review of secondary organic aerosol (SOA) formation from isoprene. *Atmos. Chem. Phys.* **2009**, *9*, 4987–5005.
- (56) Bateman, A. P.; Nizkorodov, S. A.; Laskin, J.; Laskin, A. Photolytic processing of secondary organic aerosols dissolved in cloud droplets. *Phys. Chem. Chem. Phys.* **2011**, *13*, 12199–12212.
- (57) Nguyen, T. B.; Laskin, A.; Laskin, J.; Nizkorodov, S. A. Direct aqueous photochemistry of isoprene high-NO<sub>x</sub> secondary organic aerosol. *Phys. Chem. Chem. Phys.* **2012**, *14*, 9702–9714.
- (58) Lee, H. J.; Aiona, P. K.; Laskin, A.; Laskin, J.; Nizkorodov, S. A. Effect of solar radiation on the optical properties and molecular composition of laboratory proxies of atmospheric brown carbon. *Environ. Sci. Technol.* **2014**, *48*, 10217–10226.
- (59) Romonosky, D. E.; Laskin, A.; Laskin, J.; Nizkorodov, S. A. High-resolution mass spectrometry and molecular characterization of aqueous photochemistry products of common types of secondary organic aerosols. *J. Phys. Chem. A* **2015**, *119*, 2594–2606.
- (60) Romonosky, D. E.; Li, Y.; Shiraiwa, M.; Laskin, A.; Laskin, J.; Nizkorodov, S. A. Aqueous photochemistry of secondary organic aerosol of  $\alpha$ -pinene and  $\alpha$ -humulene oxidized with ozone, hydroxyl radical, and nitrate radical. *J. Phys. Chem. A* **2017**, *121*, 1298–1309.
- (61) Mack, J.; Bolton, J. R. Photochemistry of nitrite and nitrate in aqueous solution: a review. *J. Photochem. Photobiol. A Chem.* **1999**, *128*, 1–13.
- (62) Huang, D. D.; Zhang, Q.; Cheung, H. H.; Yu, L.; Zhou, S.; Anastasio, C.; Smith, J. D.; Chan, C. K. Formation and evolution of aqSOA from aqueous-phase reactions of phenolic carbonyls: Comparison between ammonium sulfate and ammonium nitrate solutions. *Environ. Sci. Technol.* **2018**, *52*, 9215–9224.
- (63) Nozière, B.; Dziedzic, P.; Córdova, A. Inorganic ammonium salts and carbonate salts are efficient catalysts for aldol condensation in atmospheric aerosols. *Phys. Chem. Chem. Phys.* **2010**, *12*, 3864–3872.
- (64) Nozière, B.; Fache, F.; Maxut, A.; Fenet, B.; Baudouin, A.; Fine, L.; Ferronato, C. The hydrolysis of epoxides catalyzed by inorganic ammonium salts in water: kinetic evidence for hydrogen bond catalysis. *Phys. Chem. Chem. Phys.* **2018**, *20*, 1583–1590.
- (65) Mekic, M.; Brigante, M.; Vione, D.; Gligorovski, S. Exploring the ionic strength effects on the photochemical degradation of pyruvic acid in atmospheric deliquescent aerosol particles. *Atmos. Environ.* **2018**, *185*, 237–242.
- (66) Zhou, W.; Mekic, M.; Liu, J.; Loisel, G.; Jin, B.; Vione, D.; Gligorovski, S. Ionic strength effects on the photochemical degradation of acetosyringone in atmospheric deliquescent aerosol particles. *Atmos. Environ.* **2019**, *198*, 83–88.

- (67) Luo, M.; Shemesh, D.; Sullivan, M. N.; Alves, M. R.; Song, M.; Gerber, R. B.; Grassian, V. H. Impact of pH and NaCl and CaCl<sub>2</sub> salts on the speciation and photochemistry of pyruvic acid in the aqueous phase. *J. Phys. Chem* **2020**, *124*, 5071–5080.
- (68) Ray, D.; Ghosh, S. K.; Raha, S. Impacts of some co-dissolved inorganics on in-cloud photochemistry of aqueous brown carbon. *Atmos. Environ.* **2020**, *223*, 117250.
- (69) Loisel, G.; Mekic, M.; Liu, S.; Song, W.; Jiang, B.; Wang, Y.; Deng, H.; Gligorovski, S. Ionic strength effect on the formation of organonitrate compounds through photochemical degradation of vanillin in liquid water of aerosols. *Atmos. Environ.* **2021**, *246*, 118140.
- (70) Romonosky, D. E.; Ali, N. N.; Saiduddin, M. N.; Wu, M.; Lee, H. J. (; Aiona, P. K.; Nizkorodov, S. A. Effective absorption cross sections and photolysis rates of anthropogenic and biogenic secondary organic aerosols. *Atmos. Environ.* **2016**, *130*, 172–179.
- (71) Walser, M. L.; Park, J.; Gomez, A. L.; Russell, A. R.; Nizkorodov, S. A. Photochemical aging of secondary organic aerosol particles generated from the oxidation of d-limonene. *J. Phys. Chem. A* **2007**, *111*, 1907–1913.
- (72) Mang, S. A.; Henriksen, D. K.; Bateman, A. P.; Andersen, M. P. S.; Blake, D. R.; Nizkorodov, S. A. Contribution of carbonyl photochemistry to aging of atmospheric secondary organic aerosol. *J. Phys. Chemistry A* **2008**, *112*, 8337–8344.
- (73) Pan, X.; Underwood, J. S.; Xing, J. H.; Mang, S. A.; Nizkorodov, S. A. Photodegradation of secondary organic aerosol generated from limonene oxidation by ozone studied with chemical ionization mass spectrometry. *Atmos. Chem. Phys.* **2009**, *9*, 3851–3865.
- (74) Krapf, M.; El Haddad, I.; Bruns, E. A.; Molteni, U.; Daellenbach, K. R.; Prévôt, A. S.; Baltensperger, U.; Dommen, J. Labile peroxides in secondary organic aerosol. *Chem* **2016**, *1*, 603–616.
- (75) Malecha, K. T.; Nizkorodov, S. A. Photodegradation of secondary organic aerosol particles as a source of small, oxygenated volatile organic compounds. *Environ. Sci. Technol.* **2016**, *50*, 9990–9997.
- (76) Malecha, K. T.; Cai, Z.; Nizkorodov, S. A. Photodegradation of secondary organic aerosol material quantified with a quartz crystal microbalance. *Environ. Sci. Technol. Lett.* **2018**, *5*, 366–371.
- (77) Baboomian, V. J.; Gu, Y.; Nizkorodov, S. A. Photodegradation of secondary organic aerosols by long-term exposure to solar actinic radiation. *ACS Earth Sp. Chem* **2020**, *4*, 1078–1089.
- (78) Lignell, H.; Hinks, M. L.; Nizkorodov, S. A. Exploring matrix effects on photochemistry of organic aerosols. *Proc. Natl. Acad. Sci. U. S. A.* **2014**, *111*, 13780–13785.

- (79) Hinks, M. L.; Brady, M. V.; Lignell, H.; Song, M.; Grayson, J. W.; Bertram, A. K.; Lin, P.; Laskin, A.; Laskin, J.; Nizkorodov, S. A. Effect of viscosity on photodegradation rates in complex secondary organic aerosol materials. *Phys. Chem. Chem. Phys.* **2016**, *18*, 8785–8793.
- (80) Fleming, L. T.; Lin, P.; Roberts, J. M.; Selimovic, V.; Yokelson, R.; Laskin, J.; Laskin, A.; Nizkorodov, S. A. Molecular composition and photochemical lifetimes of brown carbon chromophores in biomass burning organic aerosol. *Atmos. Chem. Phys.* **2020**, *20*, 1105–1129.
- (81) Dalton, A. B.; Nizkorodov, S. A. Photochemical degradation of 4-nitrocatechol and 2,4-dinitrophenol in a sugar-glass secondary organic aerosol surrogate. *Environ. Sci. Technol.* **2021**, *55*, 14586–14594.
- (82) Fuzzi, S.; Facchini, M. C.; Decesari, S.; Matta, E.; Mircea, M. Soluble organic compounds in fog and cloud droplets: What have we learned over the past few years? *Atmos. Res.* **2002**, *64*, 89–98.
- (83) Mochida, M.; Kawabata, A.; Kawamura, K.; Hatsushika, H.; Yamazaki, K. Seasonal variation and origins of dicarboxylic acids in the marine atmosphere over the western North Pacific. *J. Geophys. Res. D Atmos.* **2003**, *108*, DOI: 10.1029/2002jd002355.
- (84) Sempéré, R.; Kawamura, K. Trans-hemispheric contribution of C<sub>2</sub>-C<sub>10</sub>  $\alpha$ ,  $\omega$ -dicarboxylic acids, and related polar compounds to water-soluble organic carbon in the western Pacific aerosols in relation to photochemical oxidation reactions. *Global Biogeochem. Cycles* **2003**, *17*, 449–459.
- (85) Römpp, A.; Winterhalter, R.; Moortgat, G. K. Oxodicarboxylic acids in atmospheric aerosol particles. *Atmos. Environ.* **2006**, *40*, 6846–6862.
- (86) Gowda, D.; Kawamura, K.; Tachibana, E. Identification of hydroxy- and keto-dicarboxylic acids in remote marine aerosols using gas chromatography/quadruple and time-of-flight mass spectrometry. *Rapid Commun. Mass Spectrom.* **2016**, *30*, 992–1000.
- (87) Gowda, D.; Kawamura, K. Seasonal variations of low molecular weight hydroxy-dicarboxylic acids and oxaloacetic acid in remote marine aerosols from Chichijima Island in the western North Pacific (December 2010–November 2011). *Atmos. Res.* **2018**, *204*, 128–135.
- (88) Chan, M. N.; Zhang, H.; Goldstein, A. H.; Wilson, K. R. Role of water and phase in the heterogeneous oxidation of solid and aqueous succinic acid aerosol by hydroxyl radicals. *J. Phys. Chem. C* **2014**, *118*, 28978–28992.
- (89) Rousová, J.; Chintapalli, M. R.; Lindahl, A.; Casey, J.; Kubátová, A. Simultaneous determination of trace concentrations of aldehydes and carboxylic acids in particulate matter. *J. Chromatogr. A* **2018**, *1544*, 49–61.
- (90) Kaneko, V. On the catalytic decarboxylation of  $\beta$ -ketoic acid. *J. Biochem.* **1938**, *28*, 1–18.
- (91) Utter, M. In *Citric Acid Cycle*; New York: Marcel Dekker: 1969, pp 249–296.
- (92) Pedersen, K. J.; Wickberg, B.; Gustafsson, C.; Sörensen, N. A. Amine catalysis in the decarboxylation of oxalacetic acid. *Acta Chem. Scand.* **1954**, *8*, 710–722.

- (93) Gelles, E. Kinetics of the decarboxylation of oxaloacetic acid. *J. Chem. Soc.* **1956**, 4715–4727.
- (94) Kozłowski, J.; Zuman, P. Acid-base, hydration-dehydration and keto-enol equilibria in aqueous solutions of  $\alpha$ -ketoacids: Study by spectroscopy, polarography and linear sweep voltammetry. *Bioelectrochemistry Bioenerg.* **1992**, *28*, 43–70.
- (95) Thalji, N. K.; Crowe, W. E.; Waldrop, G. L. Kinetic mechanism and structural requirements of the amine-catalyzed decarboxylation of oxaloacetic acid. *J. Org. Chem.* **2009**, *74*, 144–152.
- (96) Song, M.; Zhang, Z.; Fan, C.; Li, D.; Xu, Q.; Zhang, S. A theoretical study on ethylenediamine catalyzed decarboxylation of oxaloacetic acid. *Comput. Theor. Chem.* **2013**, *1022*, 29–34.
- (97) Cheng, X. Coupling and decarboxylation mechanism of oxaloacetic acid and ethylenediamine: A theoretical investigation. *J. Phys. Org. Chem.* **2019**, *32*, e3955.
- (98) Fan, C.; Song, M. Mechanistic insights into protonated diamine-catalyzed decarboxylation of oxaloacetate. *Lett. Org. Chem.* **2019**, *16*, 202–208.
- (99) Pedersen, K. J. The dissociation constants of pyruvic and oxaloacetic acid. *Acta Chem. Scand.* **1952**, *6*, 243–256.
- (100) Ito, H.; Kobayashi, H.; Nomiya, K. Metal-ion catalyzed decarboxylation of oxaloacetic acid. *R. Soc. Chem.* **1973**, *69*, 113–121.
- (101) Westheimer, F. H.; Jones, W. A. The effect of solvent on some reaction rates. *J. Am. Chem. Soc.* **1941**, *63*, 3283–3286.
- (102) Epstein, S. A.; Tapavicza, E.; Furche, F.; Nizkorodov, S. A. Direct photolysis of carbonyl compounds dissolved in cloud and fog droplets. *Atmos. Chem. Phys.* **2013**, *13*, 9461–9477.
- (103) Arakaki, T.; Anastasio, C.; Kuroki, Y.; Nakajima, H.; Okada, K.; Kotani, Y.; Handa, D.; Azechi, S.; Kimura, T.; Tsuchi, A.; Miyagi, Y. A general scavenging rate constant for reaction of hydroxyl radical with organic carbon in atmospheric waters. *Environ. Sci. Technol.* **2013**, *47*, 8196–8203.
- (104) Kaur, R.; Anastasio, C. Light absorption and the photoformation of hydroxyl radical and singlet oxygen in fog waters. *Atmos. Environ.* **2017**, *164*, 387–397.
- (105) Kaur, R.; Labins, J. R.; Helbock, S. S.; Jiang, W.; Bein, K. J.; Zhang, Q.; Anastasio, C. Photooxidants from brown carbon and other chromophores in illuminated particle extracts. *Atmos. Chem. Phys.* **2019**, *19*, 6579–6594.
- (106) Monod, A.; Doussin, J. F. Structure-activity relationship for the estimation of OH-oxidation rate constants of aliphatic organic compounds in the aqueous phase: alkanes, alcohols, organic acids and bases. *Atmos. Environ.* **2008**, *42*, 7611–7622.
- (107) Doussin, J. F.; Monod, A. Structure-activity relationship for the estimation of OH-oxidation rate constants of carbonyl compounds in the aqueous phase. *Atmos. Chem. Phys.* **2013**, *13*, 11625–11641.

- (108) Buxton, G. V.; Greenstock, C. L.; Phillips Helman, W.; Ross, A. B.; Helman, W. P. Critical review of aqueous solution reaction rate constants for hydrogen atoms and hydroxyl radicals in aqueous solution. *J. Phys. Chem. Ref. Data* **1988**, *17*, 663.
- (109) Merz, J. H.; Waters, W. A. Some oxidations involving the free hydroxyl radical. *J. Chem. Soc.* **1949**, S15–S25.
- (110) Perdew, J. P.; Ernzerhof, M.; Burke, K. Rationale for mixing exact exchange with density functional approximations. *J. Chem. Phys.* **1996**, *105*, 9982–9985.
- (111) Weigend, F.; Häser, M. RI-MP2: First derivatives and global consistency. *Theor. Chem. Acc.* **1997**, *97*, 331–340.
- (112) Weigend, F.; Häser, M.; Patzelt, H.; Ahlrichs, R. RI-MP2: Optimized auxiliary basis sets and demonstration of efficiency. *Chem. Phys. Lett.* **1998**, *294*, 143–152.
- (113) Von Arnim, M.; Ahlrichs, R. Performance of parallel TURBOMOLE for density functional calculations. *J. Comput. Chem.* **1998**, *19*, 1746–1757.
- (114) Deglmann, P.; Furche, F. Efficient characterization of stationary points on potential energy surfaces. *J. Chem. Phys.* **2002**, *117*, 9535–9538.
- (115) Klamt, A.; Schuurmann, G. COSMO: A new approach to dielectric screening in solvents with explicit expressions for the screening energy and its gradient. *J. Chem. Soc.* **1993**, *5*, 799–805.
- (116) Haynes, W. M., *CRC Handbook of Chemistry and Physics*, 93rd; CRC Press: Boca Raton, FL, 2012, p 2664.
- (117) Schäfer, A.; Klamt, A.; Sattel, D.; Lohrenz, J. C.; Eckert, F. COSMO implementation in TURBOMOLE: Extension of an efficient quantum chemical code towards liquid systems. *Phys. Chem. Chem. Phys.* **2000**, *2*, 2187–2193.
- (118) Balasubramani, S. G. et al. TURBOMOLE: Modular program suite for ab initio quantum-chemical and condensed-matter simulations. *J. Chem. Phys.* **2020**, *152*, 184107.
- (119) Bruice, P. Y. Formation of a carbinolamine intermediate in the tertiary amine catalyzed enolization of oxaloacetic acid. An alternative mechanism for enolization. *J. Am. Chem. Soc.* **1983**, *105*, 4982–4996.
- (120) Herrmann, H. Kinetics of aqueous phase reactions relevant for atmospheric chemistry. *Chem. Rev.* **2003**, *103*, 4691–4716.
- (121) Ervens, B.; Turpin, B. J.; Weber, R. J. Secondary organic aerosol formation in cloud droplets and aqueous particles (aqSOA): A review of laboratory, field and model studies. *Atmos. Chem. Phys.* **2011**, *11*, 11069–11102.
- (122) Dawson, R. M. C.; Elliott, D.; Elliott, W. H.; Jones, K. M., *Data for Biochemical Research*; Clarendon Press: Oxford, 1959.
- (123) Huang, C. L.; Wu, C. C.; Lien, M. H. Ab initio studies of decarboxylations of the  $\beta$ -keto carboxylic acids XCOCH<sub>2</sub>COOH (X = H, OH, and CH<sub>3</sub>). *J. Phys. Chem. A* **1997**, *101*, 7867–7873.

- (124) Staikova, M.; Oh, M.; Donaldson, D. J. Overtone-induced decarboxylation: A potential sink for atmospheric diacids. *J. Phys. Chem. A* **2005**, *109*, 597–602.
- (125) Seeman, J. I. The Curtin-Hammett Principle and the Winstein-Holness Equation: New definition and recent extensions to classical concepts. *J. Chem. Educ.* **1986**, *63*, 42–48.
- (126) Leussing, D. L.; Raghavan, N. V. Ethylenediamine and aminoacetonitrile catalyzed decarboxylation of oxalacetate. *J. Am. Chem. Soc.* **1980**, *102*, 5635–5647.
- (127) Smith, J. N.; Barsantia, K. C.; Friedli, H. R.; Ehnd, M.; Kulmala, M.; Collins, D. R.; Scheckman, J. H.; Williams, B. J.; McMurry, P. H. Observations of aminium salts in atmospheric nanoparticles and possible climatic implications. *Proc. Natl. Acad. Sci. U. S. A.* **2010**, *107*, 6634–6639.
- (128) Surratt, J. D.; Kroll, J. H.; Kleindienst, T. E.; Edney, E. O.; Claeys, M.; Sorooshian, A.; Ng, N. L.; Offenberg, J. H.; Lewandowski, M.; Jaoui, M.; Flagan, R. C.; Seinfeld, J. H. Evidence for organosulfates in secondary organic aerosol. *Environ. Sci. Technol.* **2007**, *41*, 517–527.
- (129) Minerath, E. C.; Elrod, M. J. Assessing the potential for diol and hydroxy sulfate ester formation from the reaction of epoxides in tropospheric aerosols. *Environ. Sci. Technol.* **2009**, *43*, 1386–1392.
- (130) Surratt, J. D.; Chan, A. W.; Eddingsaas, N. C.; Chan, M. N.; Loza, C. L.; Kwan, A. J.; Hersey, S. P.; Flagan, R. C.; Wennberg, P. O.; Seinfeld, J. H. Reactive intermediates revealed in secondary organic aerosol formation from isoprene. *Proc. Natl. Acad. Sci. U. S. A.* **2010**, *107*, 6640–6645.
- (131) Nozière, B.; Dziedzic, P.; Córdoba, A. Products and kinetics of the liquid-phase reaction of glyoxal catalyzed by ammonium ions ( $\text{NH}_4^+$ ). *J. Phys. Chem. A* **2009**, *113*, 231–237.
- (132) Pedersen, K. J. The ketonic decomposition of beta-keto carboxylic acids. *J. Am. Chem. Soc.* **1929**, *51*, 2098–2107.
- (133) Hay, R. W.; Bond, M. A. Kinetics of the decarboxylation of acetoacetic acid. *Aust. J. Chem.* **1967**, *20*, 1823–1828.
- (134) Beck, M.; Winterhalter, R.; Herrmann, F.; Moortgat, G. K. The gas-phase ozonolysis of  $\alpha$ -humulene. *Phys. Chem. Chem. Phys.* **2011**, *13*, 10970–11001.
- (135) Shaffer, G. W.; Doerr, A. B.; Purzycki, K. L. Photoisomerization of nopinone. *Org. Chem* **1972**, *37*, 25–29.
- (136) Lignell, H.; Epstein, S. A.; Marvin, M. R.; Shemesh, D.; Gerber, B.; Nizkorodov, S. Experimental and theoretical study of aqueous cis-pinonic acid photolysis. *J. Phys. Chem. A* **2013**, *117*, 12930–12945.
- (137) Ziemann, P. J.; Atkinson, R. Kinetics, products, and mechanisms of secondary organic aerosol formation. *Chem. Soc. Rev.* **2012**, *41*, 6582–6605.
- (138) Tilgner, A.; Bräuer, P.; Wolke, R.; Herrmann, H. Modelling multiphase chemistry in deliquescent aerosols and clouds using CAPRAM3.0i. *J. Atmos. Chem.* **2013**, *70*, 221–256.



- (139) Deguillaume, L.; Leriche, M.; Desboeufs, K.; Mailhot, G.; George, C.; Chaumerliac, N. Transition metals in atmospheric liquid phases: Sources, reactivity, and sensitive parameters. *Chem. Rev.* **2005**, *105*, 3388–3431.
- (140) Nguyen, T. B.; Bateman, A. P.; Bones, D. L.; Nizkorodov, S. A.; Laskin, J.; Laskin, A. High-resolution mass spectrometry analysis of secondary organic aerosol generated by ozonolysis of isoprene. *Atmos. Environ.* **2010**, *44*, 1032–1042.
- (141) Updyke, K. M.; Nguyen, T. B.; Nizkorodov, S. A. Formation of brown carbon via reactions of ammonia with secondary organic aerosols from biogenic and anthropogenic precursors. *Atmos. Environ.* **2012**, *63*, 22–31.
- (142) Madronich, S. ACOM: Quick TUV, 2016.
- (143) Benedict, K. B.; McFall, A. S.; Anastasio, C. Quantum yield of nitrite from the photolysis of aqueous nitrate above 300nm. *Environ. Sci. Technol.* **2017**, *51*, 4387–4395.
- (144) Beers, R.; Sizer, I. A spectrophotometric method for measuring the breakdown of hydrogen peroxide by catalase. *J. Biol. Chem.* **1952**, *195*, 133–140.
- (145) Warneck, P.; Wurzinger, C. Product quantum yields for the 305-nm photodecomposition of nitrate in aqueous solution. *J. Phys. Chem.* **1988**, *92*, 6278–6283.
- (146) Chu, L.; Anastasio, C. Quantum yields of hydroxyl radical and nitrogen dioxide from the photolysis of nitrate on ice. *J. Phys. Chem. A* **2003**, *107*, 9594–9602.
- (147) Goldstein, S.; Aschengrau, D.; Diamant, Y.; Rabani, J. Photolysis of aqueous H<sub>2</sub>O<sub>2</sub>: Quantum yield and applications for polychromatic UV actinometry in photoreactors. *Environ. Sci. Technol.* **2007**, *41*, 7486–7490.
- (148) Christensen, H.; Sehested, K.; Corfitzen, H. Reactions of hydroxyl radicals with hydrogen peroxide at ambient and elevated temperatures. *J. Phys. Chem.* **1982**, *86*, 1588–1590.
- (149) Bateman, A. P.; Nizkorodov, S. A.; Laskin, J.; Laskin, A. Time-resolved molecular characterization of limonene/ozone aerosol using high-resolution electrospray ionization mass spectrometry. *Phys. Chem. Chem. Phys.* **2009**, *11*, 7931–7942.
- (150) Nguyen, T. B.; Laskin, J.; Laskin, A.; Nizkorodov, S. A. Nitrogen-containing organic compounds and oligomers in secondary organic aerosol formed by photooxidation of isoprene. *Environ. Sci. Technol.* **2011**, *45*, 6908–6918.
- (151) Nguyen, T. B.; Roach, P. J.; Laskin, J.; Laskin, A.; Nizkorodov, S. A. Effect of humidity on the composition of isoprene photooxidation secondary organic aerosol. *Atmos. Chem. Phys.* **2011**, *11*, 6931–6944.
- (152) Bateman, A. P.; Laskin, J.; Laskin, A.; Nizkorodov, S. A. Applications of high-resolution electrospray ionization mass spectrometry to measurements of average oxygen to carbon ratios in secondary organic aerosols. *Environ. Sci. Technol.* **2012**, *46*, 8315–8324.
- (153) Nizkorodov, S. A.; Laskin, J.; Laskin, A. Molecular chemistry of organic aerosols through the application of high resolution mass spectrometry. *Phys. Chem. Chem. Phys.* **2011**, *13*, 3612–3629.

- (154) Willoughby, R.; Sheehan, E.; Mitrovich, S. In *A Glob. View LC/MS*; Global View Publishing: Pittsburg, PA, 1998, pp 311–315.
- (155) Leenheer, J. A.; Rostad, C. E.; Gates, P. M.; Furlong, E. T.; Ferrer, I. Molecular resolution and fragmentation of fulvic acid by electrospray ionization/multistage tandem mass spectrometry. *Anal. Chem.* **2001**, *73*, 1461–1471.
- (156) Kind, T.; Fiehn, O. Seven Golden Rules for heuristic filtering of molecular formulas obtained by accurate mass spectrometry. *BMC Bioinformatics* **2007**, *8*, 105.
- (157) Bones, D. L.; Henricksen, D. K.; Mang, S. A.; Gonsior, M.; Bateman, A. P.; Nguyen, T. B.; Cooper, W. J.; Nizkorodov, S. A. Appearance of strong absorbers and fluorophores in limonene-O<sub>3</sub> secondary organic aerosol due to NH<sub>4</sub><sup>+</sup>-mediated chemical aging over long time scales. *J. Geophys. Res. Atmos.* **2010**, *115*, D05203.
- (158) Tolocka, M. P.; Jang, M.; Ginter, J. M.; Cox, F. J.; Kamens, R. M.; Johnston, M. V. Formation of oligomers in secondary organic aerosol. *Environ. Sci. Technol.* **2004**, *38*, 1428–1434.
- (159) Baltensperger, U. et al. Secondary organic aerosols from anthropogenic and biogenic precursors. *Faraday Discuss.* **2005**, *130*, 265–278.
- (160) Reinhardt, A.; Emmenegger, C.; Gerrits, B.; Panse, C.; Dommen, J.; Baltensperger, U.; Zenobi, R.; Kalberer, M. Ultrahigh mass resolution and accurate mass measurements as a tool To characterize oligomers in secondary organic aerosols. *Anal. Chem.* **2007**, *79*, 4074–4082.
- (161) Gao, Y.; Hall, W. A.; Johnston, M. V. Molecular composition of monoterpene secondary organic aerosol at low mass loading. *Environ. Sci. Technol.* **2010**, *44*, 7897–7902.
- (162) Kristensen, K.; Watne, Å. K.; Hammes, J.; Lutz, A.; Petäjä, T.; Hallquist, M.; Bilde, M.; Glasius, M. High-molecular weight dimer esters are major products in aerosols from  $\alpha$ -pinene ozonolysis and the boreal forest. *Environ. Sci. Technol. Lett.* **2016**, *3*, 280–285.
- (163) Glasius, M.; Duane, M.; Larsen, B. R. Determination of polar terpene oxidation products in aerosols by liquid chromatography–ion trap mass spectrometry. *J. Chromatogr. A* **1999**, *833*, 121–135.
- (164) Camredon, M.; Hamilton, J. F.; Alam, M. S.; Wyche, K. P.; Carr, T.; White, I. R.; Monks, P. S.; Rickard, A. R.; Bloss, W. J. Distribution of gaseous and particulate organic composition during dark  $\alpha$ -pinene ozonolysis. *Atmos. Chem. Phys.* **2010**, *10*, 2893–2917.
- (165) Kahnt, A.; Iinuma, Y.; Mutzel, A.; Böge, O.; Claeys, M.; Herrmann, H. Campholenic aldehyde ozonolysis: A mechanism leading to specific biogenic secondary organic aerosol constituents. *Atmos. Chem. Phys.* **2014**, *14*, 719–736.
- (166) Venkatachari, P.; Hopke, P. K. Characterization of products formed in the reaction of ozone with  $\alpha$ -pinene: Case for organic peroxides. *J. Environ. Monit.* **2008**, *10*, 966–974.

- (167) Witkowski, B.; Gierczak, T. Early stage composition of SOA produced by  $\alpha$ -pinene/ozone reaction:  $\alpha$ -Acyloxyhydroperoxy aldehydes and acidic dimers. *Atmos. Environ.* **2014**, *95*, 59–70.
- (168) Bender, M. L. Mechanisms of catalysis of nucleophilic reactions of carboxylic acid derivatives. *Chem. Rev.* **1960**, *60*, 54–107.
- (169) King, R.; Bonfiglio, R.; Fernandez-Metzler, C.; Miller-Stein, C.; Olah, T. Mechanistic investigation of ionization suppression in electrospray ionization. *J. Am. Soc. Mass Spectrom.* **2000**, *11*, 942–950.
- (170) Ng, N. L.; Kroll, J. H.; Keywood, M. D.; Bahreini, R.; Varutbangkul, V.; Flagan, R. C.; Seinfeld, J. H.; Lee, A.; Goldstein, A. H. Contribution of first- versus second-generation products to secondary organic aerosols formed in the oxidation of biogenic hydrocarbons. *Environ. Sci. Technol.* **2006**, *40*, 2283–2297.
- (171) Thomas Brinkmann; Philip Hörsch; Daniel Sartorius; Frimmel, F. H. Photoformation of low-molecular-weight organic acids from brown water dissolved organic matter. *Environ. Sci. Technol.* **2003**, *37*, 4190–4198.
- (172) Kujawinski, E. B.; Del Vecchio, R.; Blough, N. V.; Klein, G. C.; Marshall, A. G. Probing molecular-level transformations of dissolved organic matter: Insights on photochemical degradation and protozoan modification of DOM from electrospray ionization Fourier transform ion cyclotron resonance mass spectrometry. *Mar. Chem.* **2004**, *92*, 23–37.
- (173) Feng, Y.; Ramanathan, V.; Kotamarthi, V. R. Brown carbon: A significant atmospheric absorber of solar radiation. *Atmos. Chem. Phys.* **2013**, *13*, 8607–8621.
- (174) Liu, J.; Lin, P.; Laskin, A.; Laskin, J.; Kathmann, S. M.; Wise, M.; Caylor, R.; Imholt, F.; Selimovic, V.; Shilling, J. E. Optical properties and aging of light-absorbing secondary organic aerosol. *Atmos. Chem. Phys.* **2016**, *16*, 12815–12827.
- (175) Jang, M.; Kamens, R. M. Characterization of secondary aerosol from the photooxidation of toluene in the presence of NO<sub>x</sub> and 1-propene. *Environ. Sci. Technol.* **2001**, *35*, 3626–3639.
- (176) Lin, P.; Liu, J.; Shilling, J. E.; Kathmann, S. M.; Laskin, J.; Laskin, A. Molecular characterization of brown carbon (BrC) chromophores in secondary organic aerosol generated from photo-oxidation of toluene. *Phys. Chem. Chem. Phys.* **2015**, *17*, 23312–23325.
- (177) Kourtechev, I.; Doussin, J. F.; Giorio, C.; Mahon, B.; Wilson, E. M.; Maurin, N.; Pangu, E.; Venables, D. S.; Wenger, J. C.; Kalberer, M. Molecular composition of fresh and aged secondary organic aerosol from a mixture of biogenic volatile compounds: A high-resolution mass spectrometry study. *Atmos. Chem. Phys.* **2015**, *15*, 5683–5695.
- (178) Hinks, M. L.; Montoya-Aguilera, J.; Ellison, L.; Lin, P.; Laskin, A.; Laskin, J.; Shiraiwa, M.; Dabdub, D.; Nizkorodov, S. A. Effect of relative humidity on the composition of secondary organic aerosol from the oxidation of toluene. *Atmos. Chem. Phys.* **2018**, *18*, 1643–1652.

- (179) Klodt, A. L. *Experiment Set: Toluene SOA Generation for matrix effects study*; tech. rep.; University of California Irvine, 2022.
- (180) Collett, J. L.; Bator, A.; Sherman, D.; Moore, K. F.; Hoag, K. J.; Demoz, B. B.; Rao, X.; Reilly, J. E. The chemical composition of fogs and intercepted clouds in the United States. *Atmos. Res.* **2002**, *64*, 29–40.
- (181) Collett, J. L.; Herckes, P.; Youngster, S.; Lee, T. Processing of atmospheric organic matter by California radiation fogs. *Atmos. Res.* **2008**, *87*, 232–241.
- (182) Dittmar, T.; Koch, B.; Hertkorn, N.; Kattner, G. A simple and efficient method for the solid-phase extraction of dissolved organic matter (SPE-DOM) from seawater. *Limnol. Oceanogr. Methods* **2008**, *6*, 230–235.
- (183) Kourtchev, I.; Szeto, P.; O’Connor, I.; Popoola, O. A.; Maenhaut, W.; Wenger, J.; Kalberer, M. Comparison of heated electrospray ionization and nanoelectrospray ionization sources coupled to ultra-high-resolution mass spectrometry for analysis of highly complex atmospheric aerosol samples. *Anal. Chem.* **2020**, *92*, 8396–8403.
- (184) Nguyen, T. B.; Lee, P. B.; Updyke, K. M.; Bones, D. L.; Laskin, J.; Laskin, A.; Nizkorodov, S. A. Formation of nitrogen- and sulfur-containing light-absorbing compounds accelerated by evaporation of water from secondary organic aerosols. *J. Geophys. Res. Atmos.* **2012**, *117*, 1207.
- (185) Walhout, E. Q.; Yu, H.; Thrasher, C.; Shusterman, J. M.; O’Brien, R. E. Effects of photolysis on the chemical and optical properties of secondary organic material over extended time scales. *ACS Earth Sp. Chem.* **2019**, *3*, 1226–1236.
- (186) Chin, H.; Hopstock, K. S.; Fleming, L. T.; Nizkorodov, S. A.; Al-Abadleh, H. A. Effect of aromatic ring substituents on the ability of catechol to produce brown carbon in iron(III)-catalyzed reactions. *Environ. Sci. Atmos.* **2021**, *1*, 64–78.
- (187) O’Brien, R. E.; Ridley, K. J.; Canagaratna, M. R.; Jayne, J. T.; Croteau, P. L.; Worsnop, D. R.; Hapsari Budisulistiorini, S.; Surratt, J. D.; Follett, C. L.; Repeta, D. J.; Kroll, J. H. Ultrasonic nebulization for the elemental analysis of microgram-level samples with offline aerosol mass spectrometry. *Atmos. Meas. Tech.* **2019**, *12*, 1659–1671.
- (188) O’Brien, R. E.; Kroll, J. H. Photolytic aging of secondary organic aerosol: Evidence for a substantial photo-recalcitrant fraction. *J. Phys. Chem. Lett.* **2019**, *10*, 4003–4009.
- (189) Pospisilova, V.; Bell, D. M.; Lamkaddam, H.; Bertrand, A.; Wang, L.; Bhattu, D.; Zhou, X.; Dommen, J.; Prevot, A. S.; Baltensperger, U.; El Haddad, I.; Slowik, J. G. Photodegradation of  $\alpha$ -pinene secondary organic aerosol dominated by moderately oxidized molecules. *Environ. Sci. Technol.* **2021**, *55*, 6936–6943.
- (190) Alif, A.; Pilichowski, J. F.; Boule, P. Photochemistry and environment XIII: Phototransformation of 2-nitrophenol in aqueous solution. *J. Photochem. Photobiol. A Chem.* **1991**, *59*, 209–219.

- (191) Kim, S.; Kramer, R. W.; Hatcher, P. G. Graphical method for analysis of ultrahigh-resolution broadband mass spectra of natural organic matter, the Van Krevelen diagram. *Anal. Chem.* **2003**, *75*, 5336–5344.
- (192) Nozière, B. et al. The molecular identification of organic compounds in the atmosphere: State of the art and challenges. *Chem. Rev.* **2015**, *115*, 3919–3983.
- (193) Merder, J. et al. ICBM-OCEAN: Processing ultrahigh-resolution mass spectrometry data of complex molecular mixtures. *Anal. Chem.* **2020**, *92*, 6832–6838.
- (194) Wozniak, A. S.; Bauer, J. E.; Sleighter, R. L.; Dickhut, R. M.; Hatcher, P. G. Technical Note: Molecular characterization of aerosol-derived water soluble organic carbon using ultrahigh resolution electrospray ionization Fourier transform ion cyclotron resonance mass spectrometry. *Atmos. Chem. Phys.* **2008**, *8*, 5099–5111.
- (195) Farmer, D. K.; Matsunaga, A.; Docherty, K. S.; Surratt, J. D.; Seinfeld, J. H.; Ziemann, P. J.; Jimenez, J. L. Response of an aerosol mass spectrometer to organonitrates and organosulfates and implications for atmospheric chemistry. *Proc. Natl. Acad. Sci.* **2010**, *107*, 6670–6675.
- (196) Fry, J. L.; Kiendler-Scharr, A.; Rollins, A. W.; Wooldridge, P. J.; Brown, S. S.; Fuchs, H.; Dubé, W.; Mensah, A.; Dal Maso, M.; Tillmann, R.; Dorn, H. P.; Brauers, T.; Cohen, R. C. Organic nitrate and secondary organic aerosol yield from NO<sub>3</sub> oxidation of  $\beta$ -pinene evaluated using a gas-phase kinetics/aerosol partitioning model. *Atmos. Chem. Phys.* **2009**, *9*, 1431–1449.
- (197) Bruns, E. A.; Perraud, V.; Zelenyuk, A.; Ezell, M. J.; Johnson, S. N.; Yu, Y.; Imre, D.; Finlayson-Pitts, B. J.; Alexander, M. L. Comparison of FTIR and particle mass spectrometry for the measurement of particulate organic nitrates. *Environ. Sci. Technol.* **2010**, *44*, 1056–1061.
- (198) Roberts, J. M. The atmospheric chemistry of organic nitrates. *Atmos. Environ. Part A. Gen. Top.* **1990**, *24*, 243–287.
- (199) Day, D. A.; Liu, S.; Russell, L. M.; Ziemann, P. J. Organonitrate group concentrations in submicron particles with high nitrate and organic fractions in coastal southern California. *Atmos. Environ.* **2010**, *44*, 1970–1979.
- (200) Liu, S.; Shilling, J. E.; Song, C.; Hiranuma, N.; Zaveri, R. A.; Russell, L. M. Hydrolysis of organonitrate functional groups in aerosol particles. *Aerosol Sci. Technol.* **2012**, *46*, 1359–1369.
- (201) Bejan, I.; Abd El Aal, Y.; Barnes, I.; Benter, T.; Bohn, B.; Wiesen, P.; Kleffmann, J. The photolysis of ortho-nitrophenols: a new gas phase source of HONO. *Phys. Chem. Chem. Phys.* **2006**, *8*, 2028–2035.
- (202) Sangwan, M.; Zhu, L. Absorption cross sections of 2-Nitrophenol in the 295–400 nm region and photolysis of 2-Nitrophenol at 308 and 351 nm. *J. Phys. Chem. A* **2016**, *120*, 9958–9967.

- (203) Barsotti, F.; Bartels-Rausch, T.; De Laurentiis, E.; Ammann, M.; Brigante, M.; Mailhot, G.; Maurino, V.; Minero, C.; Vione, D. Photochemical formation of nitrite and nitrous acid (HONO) upon irradiation of nitrophenols in aqueous solution and in viscous secondary organic aerosol proxy. *Environ. Sci. Technol.* **2017**, *51*, 7486–7495.
- (204) Scheerer, R.; Henglein, A. The triplet state of 3-nitropyrene. *Berichte der Bunsengesellschaft für Phys. Chemie* **1977**, *81*, 1234–1239.
- (205) Feilberg, A.; Nielsen, T. Effect of aerosol chemical composition on the photodegradation of nitro-polycyclic aromatic hydrocarbons. *Environ. Sci. Technol.* **2000**, *34*, 789–797.
- (206) *CRC Handbook of Organic Photochemistry and Photobiology, Volumes 1 & 2*, Second Edi; Horspool, W., Lenci, F., Eds.; CRC Press: 2003, pp 107–7 – 107–10.
- (207) Treinin, A.; Hayon, E. Quenching of triplet states by inorganic ions. Energy transfer and charge transfer mechanisms. *J. Am. Chem. Soc.* **1976**, *98*, 3884–3891.
- (208) Moran, M. A.; Zepp, R. G. Role of photoreactions in the formation of biologically labile compounds from dissolved organic matter. *Limnol. Oceanogr.* **1997**, *42*, 1307–1316.
- (209) Laskin, J.; Laskin, A.; Roach, P. J.; Slysz, G. W.; Anderson, G. A.; Nizkorodov, S. A.; Bones, D. L.; Nguyen, L. Q. High-resolution desorption electrospray ionization mass spectrometry for chemical characterization of organic aerosols. *Anal. Chem.* **2010**, *82*, 2048–2058.
- (210) Zhao, R.; Lee, A. K.; Huang, L.; Li, X.; Yang, F.; Abbatt, J. P. Photochemical processing of aqueous atmospheric brown carbon. *Atmos. Chem. Phys.* **2015**, *15*, 6087–6100.
- (211) Hems, R. F.; Abbatt, J. P. Aqueous phase photo-oxidation of brown carbon nitrophenols: Reaction kinetics, mechanism, and evolution of light absorption. *ACS Earth Sp. Chem.* **2018**, *2*, 225–234.
- (212) Jammoul, A.; Dumas, S.; D’Anna, B.; George, C. Photoinduced oxidation of sea salt halides by aromatic ketones: A source of halogenated radicals. *Atmos. Chem. Phys.* **2009**, *9*, 4229–4237.
- (213) Gemayel, R.; Emmelin, C.; Perrier, S.; Tomaz, S.; Baboomian, V. J.; Fishman, D. A.; Nizkorodov, S. A.; Dumas, S.; George, C. Quenching of ketone triplet excited states by atmospheric halides. *Environ. Sci. Atmos.* **2021**, *1*, 31–44.
- (214) Gelles, E. Complex formation and metal ion catalysis in the decarboxylation of oxaloacetic acid. *Journal of Inorganic and Nuclear Chemistry* **1958**, *8*, Proceedings International Symposium on the Chemistry of the Co-ordination Compounds, 625–630.
- (215) Guasco, T. L.; Cuadra-Rodriguez, L. A.; Pedler, B. E.; Ault, A. P.; Collins, D. B.; Zhao, D.; Kim, M. J.; Ruppel, M. J.; Wilson, S. C.; Pomeroy, R. S.; Grassian, V. H.; Azam, F.; Bertram, T. H.; Prather, K. A. Transition metal associations with primary biological particles in sea spray aerosol generated in a wave channel. *Environ. Sci. Technol.* **2014**, *48*, 1324–1333.

- (216) Kenseth, C. M.; Hafeman, N. J.; Huang, Y.; Dalleska, N. F.; Stoltz, B. M.; Seinfeld, J. H. Synthesis of carboxylic acid and dimer ester surrogates to constrain the abundance and distribution of molecular products in  $\alpha$ -pinene and  $\beta$ -pinene secondary organic aerosol. *Environmental Science and Technology* **2020**, *54*, 12829–12839.